JOURNAL OF PETROLOGY

Journal of Petrology, 2021, 1–35
doi: 10.1093/petrology/egaa100
Advance Access Publication Date: 27 October 2020
Original Article

OXFORD

Apatite Crystals Reveal Melt Volatile Budgets and Magma Storage Depths at Merapi Volcano, Indonesia

Weiran Li [1]*, Fidel Costa[1,2] and Kazuhide Nagashima[3]

[1]Earth Observatory of Singapore, Nanyang Technological University, Singapore, Singapore; [2]Asian School of the Environment, Nanyang Technological University, Singapore, Singapore; [3]HIGP, University of Hawai'i at Mānoa, Hawai'i, Honolulu, USA

*Corresponding author. Present address: Earth Observatory of Singapore, Nanyang Technological University, Singapore, Singapore. Telephone: (+65) 65922401; Fax: (+65) 67901585; E-mail: weiran.li@ntu.edu.sg

Received 16 December 2019; Accepted 8 October 2020

ABSTRACT

Magma volatile budgets and storage depths play a key role in controlling the eruptive styles of volcanoes. Volatile concentrations in the melt can be inferred from analyses of glass inclusions, which however may not be present in the investigated rocks or may have experienced post-entrapment processes that modify their volatile records. Apatite is becoming an alternative robust tool for unraveling the information of magmatic volatiles. Here we report a comprehensive dataset for the concentrations of volatiles and major elements in apatite crystals in the rocks from two eruptions with contrasting eruptive styles: the 2006 (dome-forming) and 2010 (explosive) eruptive events at Merapi volcano (Java, Indonesia). We obtained two-dimensional compositional distributions and in situ concentrations of H_2O, CO_2, F, Cl and S in 50 apatite crystals occurring at various textural positions. The CO_2 concentrations we report are probably the first ones from natural volcanic apatite. Using the volatile concentrations in apatite and existing thermodynamic models and geothermobarometers, we have calculated the volatile abundances of the pre-eruptive melts of the two eruptions.

We find that the apatite from the 2006 and 2010 deposits have a similar compositional range of volatiles, with a bimodal distribution of F–H_2O–CO_2 contents. The apatite included in amphibole has higher H_2O (0·9–1·0 wt %) and CO_2 ($\geq$2400 ppm), but lower F (0·9–1·4 wt %), compared to crystals included in plagioclase, clinopyroxene, or in the groundmass (H_2O: 0·4–0·7 wt %; CO_2: 40–900 ppm; F: 1·7–2·3 wt %). Using these volatile concentrations and apatite-melt exchange coefficients we obtained two distinct ranges of H_2O–CO_2–S–F–Cl concentrations in the melt. Melts in equilibrium with apatite included in amphibole had 3–8 wt % H_2O, $\geq$8000 ppm CO_2, 340–2000 ppm S, whereas melts in equilibrium with apatite included in anhydrous minerals and in the groundmass had lower H_2O (1·5–4 wt %), CO_2 (60–2500 ppm), and S (10–130 ppm). We calculated the melt H_2O–CO_2 saturation pressures and found that they correspond to two main magma storage depths. The shallow reservoir with melts stored at $\leq$10 km below the crater agrees with the depths constrained by melt inclusions, as well as the geodetic, geophysical and seismic tomography studies from the literature. We have also found a significantly deeper melt storage zone at $\geq$25–30 km recorded by the C- and H_2O-rich apatite in amphibole and barometry calculations using amphibole and high-Al clinopyroxene, which matches with the depths reported in seismic tomography studies. The high CO_2/H_2O and CO_2/SO_2 concentrations of the deep melt can help to explain the sharp increase in these ratios in fumarolic gas that were sampled just before the eruption in 2010. Supply of deep volatiles to the shallower magma column before the eruption in 2010 could have increased the magma buoyancy, and thus led to higher magma ascent rates and associated eruption explosivity.

Evidence for the faster pre-eruptive magma ascent in 2010 than 2006 is also found on the diffusion distance of Cl in apatite microlites.

Key words: eruptive styles; partition coefficient; plumbing system; subduction-zone volcano; volatiles

INTRODUCTION

Magmatic volatiles can play a large role in changing the eruptive styles of volcanoes by affecting the viscosity and buoyancy of magmas, which in turn control the eruption dynamics (Blake, 1984; Roggensack *et al.*, 1997; Giordano *et al.*, 2008; Cashman & Sparks, 2013; Cassidy *et al.*, 2018). H_2O and CO_2 are two major magmatic volatiles, whose concentrations in the melt are controlled by multiple factors, including their concentrations in the source magmas, the extent of magma fractionation, and the solubilities of H_2O and CO_2 in the melt of a given composition at a given pressure-temperature (referred to as *P–T–X* condition hereafter) (e.g. Wallace *et al.*, 2015). The abundances of H_2O and CO_2 dissolved in the pre-eruptive melt cannot be directly measured, but can be inferred from petrological investigations via analyses of volatiles in melt inclusions (MI; Wallace, 2005; Kent, 2008), calculations using mineral-based geohygrometry (e.g. the plagioclase-melt hygrometer of Lange *et al.*, 2009; the pyroxene-based hygrometer of O'Leary *et al.*, 2010), and phase equilibrium experiments. Although MIs have been found in some studies to be able to reflect the pre-eruptive volatile budgets (e.g. Lowenstern, 1995; Wallace, 2005), they are not always present in the collected rocks, and do not necessarily record the original melt compositions due to re-equilibration and/or post-entrapment crystallisation (Qin *et al.*, 1992; Danyushevsky *et al.*, 2000; Gaetani & Watson, 2000; Cottrell *et al.*, 2002; Portnyagin *et al.*, 2008; Lloyd *et al.*, 2013). In addition, MIs typically show less H_2O ($<$6 wt %; Plank *et al.*, 2013) than those inferred from equilibrium experiments (up to $>$15 wt %), implying that MIs may not be capable of recording the deepest and most hydrous melts at subduction zones (Steele-MacInnis, 2019).

In addition to the abundances of magmatic volatiles, magma ascent rate is the other key factor that controls the eruptive styles (e.g. Sparks, 2003; Cashman & Sparks, 2013; Cassidy *et al.*, 2018; Edmonds *et al.*, 2019). It is widely accepted that the more explosive eruptions are usually related to faster magma ascent, due to larger magma buoyancy and limited magma–fluid separation. The correlation between magmatic volatile budgets and ascent rates shows the necessity of considering both factors simultaneously when addressing the eruptive style(s) of a given volcano. Moreover, additional complexities can be induced by the exsolved volatiles that are either already present at pre-eruptive conditions, or from magma-volatile fluxes that moved from the deeper parts of the system to the shallow reservoir(s) (Degruyter *et al.*, 2017; Moretti *et al.*, 2018).

To provide more insights into the pre-eruptive magmatic volatile budgets, here we exploit the analyses of volatile elements (i.e. C, H, F, Cl, S) in volcanic apatite, combined with calculations using an apatite-melt thermodynamic model (Li & Costa, 2020), to study the rocks emitted from an effusive (2006) and an explosive (2010) eruption at Merapi volcano, Indonesia. With these apatite-based data and models, we have determined the abundances of volatiles in the melt of the two eruptions, and the depths of the magma storage zones below Merapi. Our findings reveal the composition of the deep volatile-rich magma (near the Moho) below Merapi, which we compare with the changes in the fumarolic gas compositions prior to the two eruptions. Combination of the estimated magmatic volatile budgets and the large difference in the magma ascent rates between the two eruptions (based on the Cl zoning in apatite) allows us to better explain the cause of the difference in eruption dynamics, i.e. there was a larger magma buoyancy in 2010 due to magma-volatile fluxing from deep to shallower melts, which led to faster magma ascent and thus larger explosivity in 2010.

The Merapi 2006 and 2010 eruptions

Merapi Volcano in central Java (Indonesia) is one of the most active volcanoes in the world, and it had about 27 eruptions in the last century (e.g. Voight *et al.*, 2000). Most eruptions at Merapi are dome-forming events with VEIs (Volcanic Explosivity Index; Newhall & Self, 1982) between 1–3, such as that occurred in 2006 (Ratdomopurbo *et al.*, 2013). But in 2010, Merapi produced an unexpectedly explosive eruption (VEI 4), which turned out to be the largest eruption in the last hundred years and caused severe hazards to the local community (Surono *et al.*, 2012). Although the eruptions in 2006 and 2010 have very different eruptive styles, most of the materials emitted from the two eruptions (except some from the very last eruptive stage in 2010; Komorowski *et al.*, 2013) show similar petrological and geochemical features, i.e. similar compositions of the bulk rocks (as basaltic andesite), mineral assemblages (see below) and phenocryst compositions (Costa *et al.*, 2013; Preece, 2014; Preece *et al.*, 2014; Erdmann et al., 2016; Preece *et al.*, 2016). A critical question is

what caused the larger and more hazardous eruption in 2010, compared to the 2006 eruption and earlier events, and in relation to this we provide below a brief review of the observations from the literature.

Eruptive styles of volcanoes are controlled by multiple factors, the most important two are probably the pre-eruptive melt volatile budgets and the magma ascent rate (e.g. Kent, 2008; Cashman & Sparks, 2013; Cassidy *et al.*, 2018). Previous studies have shown that melt inclusions in 2006 and 2010 rocks contain similar abundances of H_2O (~0·2–4 wt %) and CO_2 (mostly <200 ppm), except that those in 2010 pumices show much higher CO_2 (up to ~3000 ppm) (Nadeau *et al.*, 2013; Preece *et al.*, 2014), whereas the magma ascent in 2010 seems to be faster than that in 2006 (Costa *et al.*, 2013; Preece *et al.*, 2014; Preece *et al.*, 2016). Magma extrusion rates in 2010 are about an order of magnitude higher than those in 2006 (Pallister *et al.*, 2013), which could be due to larger abundances of volatiles from depth, and/or a complex dynamic of volatile transfer through exsolved volatile phase within the system. Here we provide a new perspective on constraining the magmatic volatile budgets, by looking into volatile elements in the mineral apatite. Constraints on the volatile abundances in melts at different depths of the plumbing system allow us to evaluate their contributions to different eruptive styles.

Using apatite to investigate melt volatile budgets

Apatite has become a more and more popular tool for calculating melt volatile budgets over the past decade (Boyce & Hervig, 2008, 2009; Van Hoose et al, 2013; Scott *et al.*, 2015; Stock *et al.*, 2016, 2018). Apatite, as a common mineral in volcanic rocks (especially from andesitic–rhyolitic systems), has been recognized as a robust recorder of melt volatile information, since it can incorporate various volatile species (e.g. F, Cl, H_2O, S and CO_2) into its crystal structure (e.g. Piccoli & Candela, 2002; Webster & Piccoli, 2015). To link the volatile composition of apatite with that of the melt, it is necessary to know the equilibrium partition relation of volatiles between the two phases. This has been investigated from previous experimental studies, and incorporated into thermodynamic models as briefly described below.

The partitioning of F, Cl and OH between apatite-melt are non-Nernstian (e.g. McCubbin *et al.*, 2015; Li & Hermann, 2017), and need to be expressed using the exchange coefficients (K_D) that involve two volatile components (e.g. A and B) among F, Cl and OH as: $K_{D_{A-B}}^{Ap-melt} = \frac{X_A^{Ap} X_B^{melt}}{X_A^{melt} X_B^{Ap}}$, where X represents the mole fraction of A or B in apatite, or in the melt. Given our interest in melt H_2O concentrations, here we focus on the K_Ds that involves OH, i.e. $K_{D_{OH-x}}^{Ap-melt}$ (x=F, Cl). The values of $K_{D_{OH-x}}^{Ap-melt}$ determined from experiments vary with not only the temperature, but also the abundances of F–Cl–OH in apatite due to their non-ideal mixing (Li & Hermann, 2017; McCubbin *et al.*, 2015; Li & Costa, 2020). The non-ideal mixing properties of ternary apatite have been constrained by thermodynamic calculations, and been used to establish a geohygrometer of silicate melts (Li & Costa, 2020), which we have used here to estimate H_2O concentrations in Merapi melts.

We have determined the concentrations of H_2O, CO_2, F, Cl and S in 50 apatite crystals that occur at various textural positions (either included in other minerals, or in the groundmass) in the rocks emitted from the Merapi 2006 and 2010 eruptions. The abundances of CO_2 reported in this study are probably the first published data for the CO_2 in volcanic apatite. With the determined volatile concentrations in the apatite, we have calculated the concentrations of H_2O and CO_2 in the pre-eruptive melts of 2006 and 2010, using the calculation procedure in Li & Costa (2020) and the estimated temperatures and halogen contents of the melt with which the apatite equilibrated. Melt H_2O contents were also calculated using the H_2O contents determined for pyroxenes from the same rocks.

ANALYTICAL TECHNIQUES AND CALCULATION METHODS

Juvenile bread-crusted bombs were collected shortly after the 2006 and 2010 eruptions, i.e. in June of 2006 and November of 2010 (see details in Costa *et al.*, 2013). The rocks collected in 2010 were from the block-rich pyroclastic density currents (PDCs) emitted at the beginning of the most explosive phases of this eruption, i.e. Eruption stage 4 on November 5, 2010 (Komorowski *et al.*, 2013). Three rocks from 2006 and three from 2010 were investigated in this study, showing similar bulk-rock compositions (Costa et al, 2013), and here we report the representative composition of each eruption deposit in Table 3. Halogen concentrations were only determined for 2010 rocks (at Actlabs, Canada) using the Instrumental Neutron Activation Analysis (INAA) for Cl, and the Ion Selective Electrode (ISE) method for F (detection limits: 0·01 wt %).

The composition of apatite crystals in three rocks emitted from each eruption were determined using a secondary ion mass spectrometer (SIMS) for volatiles (CO_2, H_2O, F, Cl, S), and using electron probe microanalysis (EPMA) for major elements, F, Cl and S (see analytical conditions below). Major element concentrations in other minerals (amphibole, plagioclase, clinopyroxene, orthopyroxene), the interstitial glass and glass inclusions in the same rocks were determined using EPMA, whereas H_2O concentrations in clinopyroxene and orthopyroxene were determined using SIMS (see analytical conditions in Supplementary Data Electronic Appendix; supplementary data are available for downloading at http://www.petrology.oxfordjournals.org).

SIMS analysis of volatiles in apatite

Volatile concentrations were determined for 50 apatite crystals using SIMS (Cameca ims-1280, at the University of Hawai'i at Mānoa). The standard-size petrographic thin sections were cut into the same size (23×23 mm^2) to fit that of the custom sample holder used for SIMS analysis. The samples were cleaned with ethanol and coated with gold before being loaded into the sample chamber from at least 24 hours before analysis. The vacuum of the sample chamber was kept below 1×10^{-9} torr with LN_2 cold trap. Scanning ion images were acquired from 13 crystals to investigate the compositional distribution of volatile components in the apatite. Quantitative analyses were performed during two sessions (in 2015 and 2016) using similar analytical conditions (except the smaller field aperture used for the analysis of CO_2; see below). CO_2 concentrations were determined in 2016 for 27 crystals. Below we describe the analytical conditions used for acquiring scanning ion images, followed by those used for quantitative analyses of F, Cl, H_2O, S and CO_2.

Scanning ion imaging

A focused Cs^+ primary beam of ~500 pA was used for pre-sputtering over an area of $\sim 35 \times 35$ μm^2 on each sample. The beam current was then reduced to ~50 pA with scanning area reduced to 30×30 μm^2 for data collection. Secondary ions of ^{16}OH, ^{18}O, ^{32}S, $^{19}F^{16}O$ and ^{37}Cl were collected sequentially with counting times of 4, 4, 12, 4 and 2 seconds, respectively, for 50–70 cycles, using an axial electron multiplier (EM). Mass resolving power was ~6000, that is high enough to separate the signals of interfering ions. Normal incident electron gun was used for charge compensation of sputtered area. Secondary ion intensities were normalized to ^{18}O and processed with the L'Image software to produce images. Each image consists of 128×128 pixels and has high resolution estimated to be ~0·5 μm

Quantitative analyses of F, Cl, H_2O, S

The crack-free crystals with nearly homogeneous cores (shown in the scanning ion images) were selected for quantitative analyses of volatile concentrations. The core of each crystal was pre-sputtered for 4–6 minutes over an area of $\sim 25 \times 25$ μm^2 using a primary Cs^+ beam of ~3 nA, after which the raster size was reduced to $\sim 15 \times 15$ μm^2 for data collection (field aperture of $\sim 2500 \times 2500$ μm^2). An electronic gating of 50% was used to minimize signals from the edges of the pits, such that only the signals from the most central area ($\sim 7{\cdot}5 \times 7{\cdot}5$ μm^2) of individual pits were used for determining volatile concentrations. Secondary ions of $^{16}O^1H$, ^{18}O, ^{34}S, $^{19}F^{16}O$ and ^{37}Cl were sequentially collected for 20 cycles using the axial EM. Normal incident electron gun was used for charge compensation of sputtered area. Secondary ion intensities were normalized to ^{18}O to determine H_2O, F, Cl and S concentrations, using calibration curves determined from natural apatite standards: three standards from McCubbin *et al.* (2012) in the 2015 session, and four standards, i.e. two from McCubbin *et al.* (2012) and two from Clark *et al.* (2016) in the 2016 session (Supplementary Data Table S1). Calibration curves were fit using the *IsoPlot* program (model-1 fit; Ludwig, 2003), showing good linear correlation between secondary ion intensities and volatile concentrations in the standards (Supplementary Data Fig. S2). The San Carlos Olivine (SC olivine) was analysed at the beginning and end of each analytical session (within the same days), reflecting low backgrounds of H_2O (~7 ppm), and S, Cl and F (all <1 ppm) during analysis. Relative errors in the determined concentrations are ~2–5% for F and H_2O, and ~5–20% for Cl and S.

Quantitative analyses of CO_2

CO_2 concentrations in apatite were determined only in the 2016 session, together with those of H_2O, S, Cl and F. These crystals are located in the two thin sections analysed in 2015 (see above), and four other thin sections that were never analysed nor coated with carbon. All the samples were carefully polished using silk cloth, cleaned using ethanol and coated with gold before analysis. To minimize air contamination, the samples were loaded in the sample chamber of SIMS at least 24 hours before analysis. Each crystal was pre-sputtered for ~5 minutes, after which secondary ion intensities of ^{12}C, $^{16}O^1H$, ^{18}O, ^{34}S, $^{19}F^{16}O$ and ^{37}Cl were collected using the same analytical condition as described above (e.g. voltage, current, analysed area, e-gate), except that this time we used a smaller field aperture ($\sim 1200 \times 1200$ μm^2) to reduce the analytical background of C. We obtained a low CO_2 concentration of ~37 ppm for the San Carlos Olivine, and ~20 ppm for the clinopyroxene and Fe–Ti oxide in the same thin sections that contain apatite, indicating background CO_2 contents of ~20 ppm during all the analysis. The collected signals of $^{12}C^-$ were normalized to $^{18}O^-$ to determine CO_2 concentrations, using calibration curves determined by a natural apatite standard ('HAM') from Clark *et al.* (2016) (Supplementary Data Table S1, Supplementary Data Fig. S1). Errors in the determined CO_2 concentrations (±1 s.d.) are ~10–30% relative.

The locations of pits produced by SIMS analyses were investigated using a scanning electron microscope (SEM). Most SIMS pits are within the analysed crystals, and those that exceed the crystal boundary or lie above cracks were ruled out (Supplementary Data Fig. S3). We noticed that three crystals that have cracks across the pit locations (Supplementary Data Fig. S3) gave abnormally high CO_2 concentrations (~4–11 wt %) that are unlikely to be real, considering that the sum of elemental concentrations in each crystal should not exceed 100% (Supplementary Data Table S2). Such high CO_2 contents likely reflect contaminant C within the cracks that could be inherited from the epoxy used for making thin sections, thus these values were excluded from consideration hereafter.

EPMA analyses of apatite

Forty two apatite crystals were analysed using a JEOL JXA 8530F field emission gun electron microprobe at the Facility for Analysis Characterization Testing and Simulation, Nanyang Technological University (Singapore). X-ray maps of Cl, F and S, and cathodoluminescence (CL) images were acquired using accelerating voltage of 15 kV, and beam current of 25 nA. Dwell times used for the X-ray mapping and CL imaging were 70 ms and 40 ms respectively. Point analyses and concentration profiles of Si, Mg, Fe, Ce, Ca, Na, P, S, F and Cl were acquired using an electron beam of lower energy (accelerating voltage: 15 kV; beam current: 10 nA). Most crystals were analysed with their c-axes not parallel to the direction of the electron beam, such that there should be a minimal extent of F migration during analysis (Stormer *et al.*, 1993; Goldoff *et al.*, 2012; Stock *et al.*, 2015). Concentration profiles with 1-μm spacing were acquired using a focused beam, but this did not produce apparent fluctuation in the counts of F, monitored through analyses. The on-peak counting times were 80 s for F, Cl, S and Mg, 60 s for Ce and Fe, 40 s for Si, and 20 s for Na, Ca and P. Natural mineral standards from Astimex Ltd were used for calibration of different elements: apatite standard for F, P, Ca; tugtupite for Cl, Na; anhydrite for S; almandine for Si, Mg; monazite for Ce. A time-dependent intensity (TDI) correction was applied to F, Cl, S and Na to mathematically correct signal variation. Concentrations were quantified using a modified ZAF matrix correction procedure (Armstrong, 1988). Background intensity was calibrated based on mean atomic number of analytical volume and continuum absorption was corrected after Donovan and Tingle (1996). Stoichiometric oxygen was calculated by cation abundance and included in the matrix correction. An absorption correction was applied for carbon coating to both the standard and sample for electrical conductivity. Detection limits for F, Cl and S are ~300 ppm, ~85 ppm and ~30 ppm, respectively. Relative errors are <1% for major elements in apatite (Ca and P), <2–3% for F and Cl, and <10% for minor elements (S, Si, Ce, Na, Mg).

The structural formula of apatite was calculated following Ketcham (2015), i.e. on the basis of 25 oxygen for the OH-rich apatite (mole fraction of OH ≥0·5; hosted by amphibole), and 26 oxygen for the OH-poor crystals (mole fraction of OH <0·5; at other textural positions). The mole fractions of OH calculated on the basis of 25-oxygen and 26-oxygen show rather small difference of <4% (Ketcham, 2015), i.e. within errors from analyses.

Abbreviations, symbols and formulations of the exchange coefficients

Abbreviations and symbols

Abbreviations used in this paper are: Ap, Apatite; Amph, amphibole; Cpx, clinopyroxene; Opx, orthopyroxene; Pl, plagioclase; Ol, Olivine; Biot, Biotite; Gm, groundmass; MI, melt inclusion. Symbols are defined as: anorthite value An $= \frac{Ca}{Ca+K+Na} \times 100$; magnesium number Mg# $= \frac{Mg}{Mg+Fe^*} \times 100$, and wollastonite value Wo $= \frac{Ca}{Ca+Mg+Fe^*} \times 100$. Fe^* indicates total Fe as Fe^{2+}.

Calculation of the exchange coefficients between apatite and the melt

The exchange coefficients $K_{D\,OH-F}^{Ap-melt}$ and $K_{D\,OH-Cl}^{Ap-melt}$ were calculated using the equations of Li & Costa (2020):

$$ln\left(K_{D\,OH-F}^{Ap-melt}\right) = -\frac{1}{R\cdot T} \times \{94600\ (\pm 5600) - 40\ (\pm 0.1) \times T - 1000 \times \left[7\ (\pm 4) \times \left(X_F^{Ap} - X_{OH}^{Ap}\right) - 11\ (\pm 7) \times X_{Cl}^{Ap}\right]\} \quad (1)$$

and

$$ln\left(K_{D\,OH-Cl}^{Ap-melt}\right) = -\frac{1}{R\cdot T} \times \{72900\ (\pm 2900) - 34\ (\pm 0.3) \times T - 1000 \times [5\ (\pm 2) \times \left(X_{Cl}^{Ap} - X_{OH}^{Ap}\right) - 10\ (\pm 8) \times X_F^{Ap}]\} \quad (2)$$

where T is temperature (in kelvins), and apatite composition is expressed in the mole fractions of *i* (=F, Cl, OH), calculated using $X_i^{Ap} = \frac{\frac{c_i^{Ap}}{M_i}}{\frac{c_F^{Ap}}{19}+\frac{c_{Cl}^{Ap}}{35.45}+\left(\frac{c_{H_2O}^{Ap}}{18}\times 2\right)}$ (where M_i is the atomic mass of *i*, and C_i^{Ap} is the weight concentration of *i* determined by SIMS; cf. Li & Costa, 2020). Calculations of $K_{D\,OH-F}^{Ap-melt}$, $K_{D\,OH-Cl}^{Ap-melt}$ and melt H_2O contents following Li & Costa (2020) can be performed using the '*ApThermo*' calculation tool in excel format, which is available in Supplementary Data Electronic Appendix A1.

The exchange coefficient for H_2O-CO_2 between apatite and the melt is defined as (Riker *et al.*, 2018):

$$K_{D\,H_2O-CO_2}^{Ap-melt} = \frac{c_{H_2O}^{Ap} \cdot c_{CO_2}^{melt}}{c_{CO_2}^{Ap} \cdot c_{H_2O}^{melt}} \quad (3)$$

where *c* represents the mass concentrations of H_2O, or CO_2 (expressed in subscript) in apatite, or in the melt (expressed in superscript). For calculations in this study, we take $K_{D\,H_2O-CO_2}^{Ap-melt} = 0.629 \pm 0.08$, determined for basaltic-andesitic melts at 1250°C and 1 GPa (Riker *et al.*, 2018).

Calculation of the exchange coefficients $K_{D\,Cl-OH}^{Amph-melt}$ and $K_{D\,Al-Si}^{Amph-melt}$ between amphibole and the melt

The exchange coefficient for Cl-OH between amphibole-melt is defined (on the basis of mole

fractions) as: $K_{D\,Cl-OH}^{Amph-melt} = \frac{X_{Cl}^{Amph} X_{OH}^{melt}}{X_{Cl}^{melt} X_{OH}^{Amph}}$. Here we have used the equation of Humphreys *et al.* (2009):

$$K_{D\,Cl-OH}^{Amph-melt} = \exp\left(8.62 - 3.46 \times Mg - 0.0062 \times T\right) \quad (4)$$

where Mg# is the Mg number of amphibole, and T is temperature in kelvins.

The exchange coefficient for Al–Si is defined (on the basis of mole fractions) as: $K_{D\,Al-Si}^{Amph-melt} = \frac{X_{Al}^{Amph} X_{Si}^{melt}}{X_{Al}^{melt} X_{Si}^{Amph}}$. We have performed a linear regression of experimental data from the literature, and found $K_{D\,Al-Si}^{Amph-melt} = 0.96 \pm 0.04$ at a range of *P–T–X* conditions (Supplementary Data Fig. S4). This value was then used to test the equilibrium between the amphibole and liquid before applying them to geothermobarometric calculations (see below).

Calculation of the partition coefficients of H_2O between pyroxenes and the melt

For calculation of melt H_2O concentrations using pyroxenes, we have taken the formulations for the partition coefficients of H_2O between Cpx-melt ($D_{H_2O}^{Cpx-melt}$) and Opx-melt ($D_{H_2O}^{Opx-melt}$) from O'Leary *et al.* (2010):

$$\ln\left(D_{H_2O}^{Cpx-melt}\right) = -4.2(\pm 0.2) + 6.5\,(\pm 0.5)\cdot X_{IV_{Al}}^{Cpx} - 1.0(\pm 0.2)\cdot X_{Ca}^{Cpx} \quad (5)$$

and

$$\ln\left(D_{H_2O}^{Opx-melt}\right) = -5.66(\pm 0.11) + 8.4\,(\pm 1.1)\cdot X_{VI_{Al}}^{Opx} + 10(\pm 2)\cdot X_{Ca}^{Opx} \quad (6)$$

where X_i^j is the mole fraction of cation i (^{IV}Al, Ca, ^{VI}Al) in phase j (Cpx, Opx), calculated on a 6-oxygen basis (cf. O'Leary *et al.*, 2010).

PETROGRAPHICAL OBSERVATIONS

The rocks emitted in 2006, and 2010 (eruption stage 4) investigated in this study show similar bulk-rock composition of basaltic-andesitic (Table 3; more details in Costa *et al.*, 2013). They also have a similar mineral assemblage of plagioclase (Pl) + clinopyroxene (Cpx) + orthopyroxene (Opx) + amphibole (Amph) + Fe–Ti oxide + apatite (Ap) ± olivine (Ol) ± biotite (Biot). Phenocrysts (> 500 μm in length) occupy ~30–40 volume percent (vol.%) of the whole rocks (vesicle-free normalization; Costa *et al.*, 2013), consisting of plagioclase (~20–30 vol.%), Cpx (~5–7 vol.%), Amph (≤0·5 vol.%), Opx (≤0·5 vol.%), and fewer Ol and Biot (≤0·1 vol.%). Fe–Ti oxide and apatite crystals exist as either microphenocrysts (~100–500 μm in length), or microlites (<100 μm in length), whereas some apatite crystals are included in other minerals.

Plagioclase phenocrysts in 2006 and 2010 rocks show a variety of textures and zoning patterns, and a broad range of An between 43 and 90 (Supplementary Data Table S4; Costa *et al.*, 2013; Cheng & Costa, 2019). Cpx phenocrysts in 2010 rocks commonly show oscillatory/sectoral zoning of Al and Mg, and some contain higher Al_2O_3 (up to 7–9 wt %) at the rim than the core (~1–2 wt %) while Mg# varying from 66 to 77. Cpx phenocrysts of 2006 are less prominently zoned and show narrower ranges of Mg# (70–77) and Al_2O_3 (1–6 wt %) (Supplementary Data Table S5). The complex zoning observed in Pl and Cpx phenocrysts of both eruptions reflect an open-system magma evolution at Merapi, where magmas migrated from depths to the shallower reservoir(s), and interacted with the more evolved and crystal-richer magmas (Costa *et al.*, 2013; Preece *et al.*, 2014; Erdmann *et al.*, 2016).

The most significant petrological differences between the rocks emitted from the two eruptions are the textures and compositions of amphibole phenocrysts and plagioclase microlites. Most of the 2006 amphibole shows reaction rims consisting of fine-grained Pl + Opx + Fe–Ti oxides that are up to tens of micrometres in width, which was rarely observed for 2010 amphibole (Fig. 1; Costa *et al.*, 2013; Preece *et al.*, 2014) and has been interpreted as evidence of a slower magma ascent in 2006 (Costa *et al.*, 2013). Some of the 2010 amphibole shows complex zoning patterns of Al_2O_3 and Mg#, whereas the 2006 amphibole is more homogeneous (Al_2O_3: 11–12 wt. %; Mg# = 68–69). In agreement with the texture of amphiboles, the higher number intensities of microlites (Pl + Cpx + Fe–Ti oxide + apatite) in stage 4 dome samples from 2010 rocks (than 2006) reflect nucleation-dominated crystallization of microlites induced by a more rapid magma ascent and degassing in 2010 than in 2006 (Costa *et al.*, 2013; Preece *et al.*, 2016).

TEXTURAL RELATIONS AND COMPOSITIONS OF APATITE

Apatite crystals occupy ~0·2–0·6 vol.% of 2006 and 2010 rocks, and they occur at various textural positions (Fig. 1): some are surrounded by the glass and appear as either microlites (30–100 μm in length) or microphenocrysts (100–180 μm in length), and the rest are included in phenocrysts of other minerals, such as Amph, Cpx, Pl and Opx. The host Amph from 2010 are oscillatory zoned of Al (Al_2O_3: ~11–13 wt %) without any reaction rim, whereas the host Amph from 2006 is compositionally more homogeneous (Al_2O_3: ~12 wt %) but has a thin reaction rim (consisting of Pl + Opx + Fe–Ti oxides). The Cpx that hosts apatite has Mg# between 74 and 76; and the host Pl has An values between 53 and 74.

Apatite inclusions can be divided into two types according to their textures and sizes: Type-1 is small (<10 μm in length) and anhedral or needle-shape, whereas Type-2 is larger (~20–80 μm in length) and subhedral–euhedral in hexagonal or tabular shapes. The two types of inclusions were likely formed under different conditions: Type-1 inclusions were likely crystallised due to local supersaturation of apatite-forming elements (e.g. phosphorus) at the boundary layer between

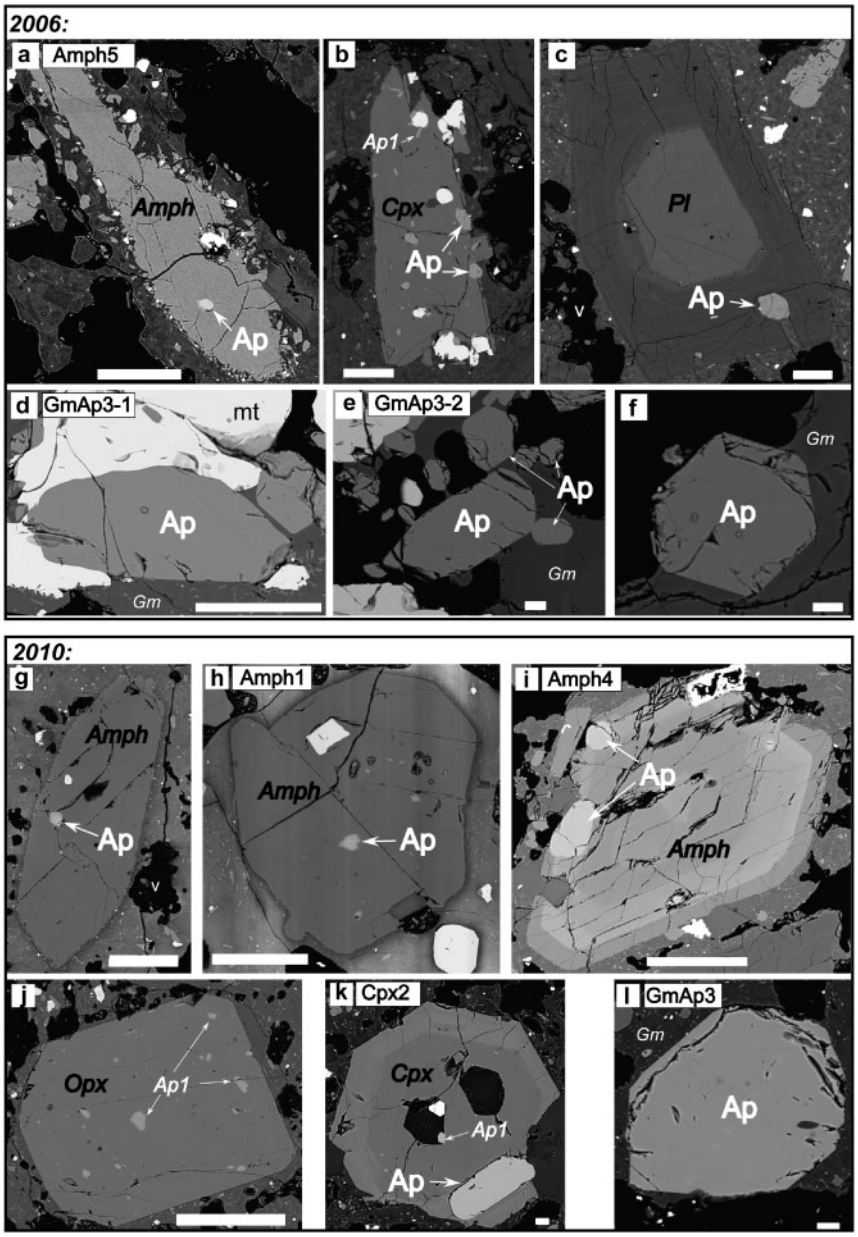

Fig. 1. Backscattered electron images of apatite crystals that occur at various textural positions in rocks emitted from (a–f) the 2006 and (g–l) 2010 eruptions (Ap, apatite; Amph, amphibole; Cpx, clinopyroxene; Opx, orthopyroxene; Pl, plagioclase; Gm, groundmass; Mt, Magnetite; see sample labels in Table 1). Apatite inclusions show two types of morphology: Type-1 inclusions (‘*Ap1*’) are $<10\,\mu m$ in length and anhedral, whereas Type-2 (‘Ap’) inclusions are larger (mostly 20–80 μm in length) and euhedral–subhedral, and were analysed in this study (see text). Scale bars are 10 μm for panels e, f, k, l, and 100 μm for the rest.

the silicate host mineral and the melt (Harrison & Watson, 1984; Bacon, 1989), whereas Type-2 inclusions that are larger and subhedral-euhedral more likely reflect the representative melt composition. Considering this, only the larger Type-2 inclusions and the crystals in the groundmass that are also subhedral-euhedral with similar sizes were analysed and used to estimate volatile concentrations in the melt.

H_2O and CO_2 concentrations were measured using SIMS, whereas F, Cl and S were measured using both SIMS and EPMA (Table 1; Supplementary Data Table S3). Given the larger analysis area by SIMS ($\sim 7{\cdot}5 \times 7{\cdot}5$ μm^2) than by EPMA ($<1 \times 1$ μm^2), the SIMS data likely represent the ‘bulk’ volatile concentrations at crystal cores, whereas the EPMA data represent the ‘local’ volatile concentrations at given locations within the crystals (at rim/mantle/core). Data obtained from the two techniques are reported below for comparison.

F, Cl and H_2O

Apatite crystals in 2006 and 2010 rocks show a similar range of F–Cl–H_2O concentrations, i.e. 1·1–2·2 wt % F, 0·4–1·2 wt % Cl and 0·5–1·0 wt % H_2O (Table 1). Apatite inclusions in amphibole show about twice as much H_2O

Table 1: Volatile compositions of the apatite (determined by SIMS), from the Merapi 2006 and 2010 (stage 4) eruptions

Eruption	Textural position	No.	Label	Concentrations (wt %)					Mole fraction		
				CO_2	H_2O	F	Cl	S	X_F	X_{Cl}	X_{OH}
2006	in Amphibole (~12 wt % Al_2O_3)	1	061506L_1, Amph5	n.d.	0·90 (4)*	0·94 (3)	0·37 (2)	0·15 (1)	0·309	0·065	0·626
2006	in Clinopyroxene (Mg#: 74–76)	2	061406, Cpx3	0·09 (2)	0·52 (5)	1·95 (5)	1·08 (4)	0·06 (2)	0·538	0·160	0·302
		3	061406, Cpx1	0·031 (6)	0·52 (5)	1·96 (5)	1·08 (4)	0·05 (2)	0·536	0·159	0·305
		4	061406, Cpx_v	0·022 (5)	0·56 (6)	1·83 (5)	1·07 (4)	0·04 (1)	0·511	0·160	0·328
		5	061506L_2, Cpx2	0·014 (4)	0·51 (2)	2·06 (5)	1·01 (4)	0·033 (3)	0·561	0·148	0·291
		6	061506L_2, Cpx6	0·005 (2)	0·52 (2)	1·83 (5)	0·97 (4)	0·032 (2)	0·532	0·151	0·317
		7	061406, Cpx6	0·004 (2)	0·55 (4)	2·00 (4)	1·0 (2)	0·031 (4)	0·541	0·145	0·314
		8	061506L_2, Cpx1	0·002 (2)	0·58 (2)	1·92 (3)	0·90 (4)	0·040 (3)	0·531	0·133	0·336
		9	061506L_1, Cpx4	n.d.	0·61 (3)	1·94 (6)	0·97 (3)	0·026 (2)	0·517	0·139	0·344
		10	061506L_1, Cpx7	n.d.	0·61 (3)	1·94 (6)	0·93 (3)	0·024 (2)	0·522	0·133	0·345
		11	061506L_1, Cpx3, Ap3	n.d.	0·59 (3)	1·85 (6)	0·79 (3)	0·026 (2)	0·527	0·120	0·354
		12	061506L_1, Cpx3, Ap4	n.d.	0·55 (3)	1·72 (5)	0·92 (4)	0·022 (2)	0·508	0·146	0·346
		13	061506L_1, Cpx3, Ap5	n.d.	0·56 (3)	1·79 (6)	0·92 (4)	0·037 (4)	0·516	0·141	0·342
2006	in Groundmass	14	061506L_2, Ox3Ap	0·08 (2)	0·48 (2)	2·13 (5)	0·94 (4)	0·13 (1)	0·585	0·138	0·277
		15	061406, GmAp8	0·047 (8)	0·67 (3)	1·55 (3)	1·0 (2)	0·039 (6)	0·443	0·153	0·404
		16	061406, GmAp4	0·035 (5)	0·51 (2)	2·30 (4)	1·0 (2)	0·029 (4)	0·587	0·138	0·275
		17	061406, GmAp7	0·014 (2)	0·50 (2)	2·25 (4)	1·1 (2)	0·11 (1)	0·578	0·151	0·271
		18	061506L_2, GmAp3	0·009 (3)	0·52 (2)	2·08 (6)	0·83 (3)	0·038 (3)	0·576	0·122	0·301
		19	061506L_2, Gm_v	0·004 (2)	0·42 (2)	2·29 (4)	0·93 (4)	0·057 (5)	0·623	0·136	0·241
		20	061506L_1, GmAp3-2-1	n.d.	0·58 (3)	1·74 (7)	0·96 (4)	0·027 (2)	0·500	0·148	0·352
		21	061506L_1, GmAp3-1	n.d.	0·60 (3)	1·84 (6)	1·00 (4)	0·024 (2)	0·505	0·147	0·348
		22	061506L_1, Ap1	n.d.	0·53 (3)	2·12 (8)	0·88 (4)	0·019 (2)	0·571	0·127	0·302
		23	061506L_1, GmAp5	n.d.	0·46 (3)	2·30 (8)	0·90 (4)	0·027 (4)	0·613	0·128	0·259
2010	in Amphibole (11–13 wt % Al_2O_3)	24	1011211A, Amph1	1·6 (2)	0·90 (4)	1·37 (2)	0·55 (3)	0·31 (5)	0·384	0·082	0·533
		25	10111123, Amph4-1 #1†	0·24 (5)	0·91 (4)	1·17 (2)	0·55 (2)	0·090 (1)	0·345	0·087	0·569
		26	10111123, Amph4-1 #2†	n.d.	0·98 (3)	1·24 (4)	0·54 (2)	0·19 (2)	0·346	0·081	0·573
		27	10111123, Amph4-2	n.d.	0·93 (4)	1·12 (5)	0·41 (2)	0·18 (2)	0·339	0·066	0·595
2010	in Clinopyroxene (Mg# = 74–76)	28	1011211A, Cpx5-1	0·03 (2)	0·59 (2)	1·99 (4)	1·18 (4)	0·041 (6)	0·515	0·163	0·322
		29	11051903, Cpx8, Ap1	0·017 (3)	0·55 (2)	2·06 (4)	1·05 (4)	0·11 (2)	0·546	0·149	0·305
		30	11051903, Cpx8, Ap2	0·012 (2)	0·55 (2)	2·07 (4)	1·03 (4)	0·030 (5)	0·549	0·146	0·305
		31	11051903, Cpx8, Ap3	0·017 (3)	0·55 (2)	2·10 (4)	1·04 (4)	0·037 (5)	0·551	0·146	0·303
		32	11051903, Cpx6	0·014 (2)	0·55 (3)	1·99 (3)	1·08 (4)	0·029 (4)	0·533	0·154	0·313
		33	1011211A, Cpx6	0·007 (2)	0·54 (2)	2·22 (4)	1·03 (4)	0·046 (7)	0·566	0·141	0·293
		34	1011211A, Cpx4	0·006 (2)	0·51 (2)	2·13 (2)	1·11 (4)	0·058 (9)	0·560	0·156	0·284
		35	1011211A, Cpx5-2	0·005 (2)	0·59 (2)	1·87 (5)	1·08 (4)	0·039 (6)	0·507	0·157	0·337
		36	10111123, Cpx5	n.d.	0·57 (2)	1·79 (6)	0·96 (3)	0·023 (2)	0·509	0·147	0·344
		37	10111123, Cpx6, Ap2	n.d.	0·57 (2)	2·00 (5)	1·01 (3)	0·028 (2)	0·535	0·144	0·321
		38	10111123, Cpx6, Ap3	n.d.	0·54 (2)	1·93 (5)	1·01 (3)	0·026 (2)	0·534	0·149	0·317
2010	in Plagioclase (An = 53–74)	39	10111123, Pl3	n.d.	0·55 (2)	1·84 (6)	0·93 (3)	0·037 (4)	0·527	0·142	0·330
		40	10111123, Pl1, Ap1	n.d.	0·44 (2)	1·24 (4)	0·75 (2)	0·15 (2)	0·482	0·157	0·361
		41	10111123, Pl1, Ap2	n.d.	0·53 (2)	1·80 (7)	0·97 (4)	0·18 (2)	0·525	0·151	0·325
2010	in Groundmass	42	1011211A, GmAp8	0·07 (1)	0·55 (2)	2·09 (4)	1·07 (4)	0·047 (7)	0·548	0·150	0·302
		43	1011211A, GmAp7	0·039 (5)	0·54 (2)	2·12 (4)	1·04 (4)	0·07 (1)	0·556	0·145	0·298
		44	11051903, GmAp6 #1	0·018 (3)	0·55 (2)	2·07 (4)	1·08 (4)	0·037 (5)	0·544	0·152	0·304
		45	11051903, GmAp6 #2	0·012 (2)	0·55 (3)	2·05 (4)	1·09 (4)	0·12 (2)	0·542	0·154	0·304
		46	10111123, GmAp3 #1	n.d.	0·57 (2)	1·97 (6)	1·03 (3)	0·022 (2)	0·528	0·148	0·324
		47	10111123, GmAp3 #2	n.d.	0·57 (2)	1·95 (6)	1·01 (3)	0·017 (2)	0·527	0·147	0·326
		48	10111123, GmAp8	n.d.	0·62 (2)	1·98 (6)	0·99 (3)	0·025 (2)	0·520	0·139	0·341
		49	10111123, GmAp9	n.d.	0·60 (2)	1·96 (5)	1·00 (3)	0·13 (1)	0·523	0·142	0·335
		50	10111123, GmAp6	n.d.	0·60 (2)	1·90 (6)	0·97 (3)	0·14 (2)	0·516	0·141	0·343

n.d., not determined.
*Values in parenthesis represent the 1σ standard deviation of volatile measurements (of the last digit).
†#1 and #2 represent analyses of different positions within the same crystal.

(0·9–1·0 wt %) and only half F (1·1–1·3 wt %), compared to the apatite in Cpx, Pl and groundmass (mean: ~0·5 wt % H_2O, ~2·0 wt % F). Comparison between the concentrations determined from SIMS and EPMA show similar ranges of F–Cl contents, and larger differences in H_2O (up to 25%, relative). Compared to the H_2O measurements from SIMS (H_2O_M), those calculated from stoichiometry (H_2O_{Calc}) based on the EPMA data show a wider range (Fig. 6), possibly related to the larger error in H_2O_{Calc} that were propagated from the error in major element concentrations determined by EPMA, and the uncertainty in the assumption of a stoichiometric anion site of apatite (Schettler *et al.*, 2011; Jones *et al.*, 2014; McCubbin & Ustunisk, 2018). Considering this, we only used H_2O, F and Cl concentrations determined by SIMS to calculate the mole fractions of OH, F and Cl in apatite (X_{OH}^{Ap}, X_F^{Ap}, X_{Cl}^{Ap}) and the melt volatile budgets hereafter.

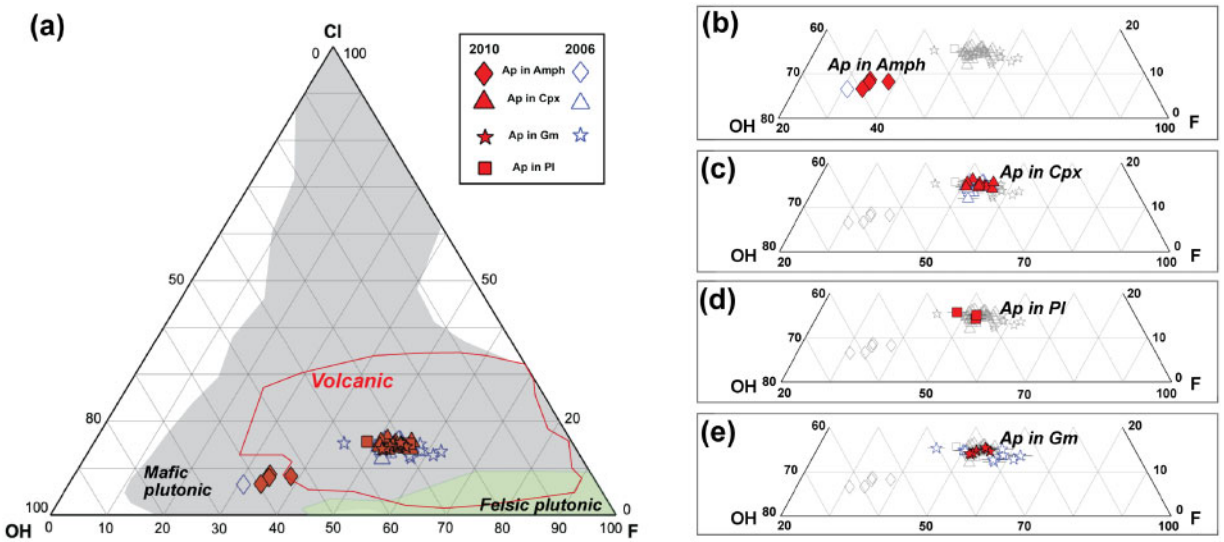

Fig. 2. Cl–OH–F ternary diagrams for apatite crystals from the 2006 (empty symbols) and 2010 (solid symbols in red) eruption deposits (mole fractions calculated using the SIMS data in Table 1). (a) shows all the data determined from this study, compared to volatile compositions of apatite in different types of rocks from the literature (adapted from Li & Costa, 2020). (b–e) show crystals at different textural positions in different symbols (see legend). The crystals from 2006 and 2010 show similar range of Cl–OH–F, and similar bimodal distribution of F–OH: those included in Amph are higher in OH and lower in F, within the range of mafic plutonic apatite (grey field in a), whereas those in Cpx, Pl, and groundmass are lower in OH, similar to apatite from other volcanic rocks (red line in panel a). Errors bars show ±1 s.d. of volatile measurements by SIMS (most errors within the symbol size).

The 2006 and 2010 apatite show a similar bimodal distribution of F–Cl–OH (Fig. 2; Table 1): crystals in Amph are OH-rich and F-poor (X_{OH}^{Ap} = 55–63%, X_{F}^{Ap} = 30–38%, X_{Cl}^{Ap} = 7–9%), with similar composition to apatite from mafic plutonic rocks (e.g. gabbro; Boudreau, 1995), whereas crystals in Cpx, Pl and Gm are lower in OH and higher in F (X_{OH}^{Ap} = 26–40%, X_{F}^{Ap} = 50–60%, X_{Cl}^{Ap} = 12–16%, with similar composition to apatite from other volcanic systems (e.g. Peng *et al.*, 1997; Webster *et al.*, 2009; Van Hoose *et al.*, 2013; Scott *et al.*, 2015; Stock *et al.*, 2016, 2018). The distinct F–Cl–OH compositions of crystals that occur at different textural positions implies that they may have crystallised or equilibrated at different *P–T–X* conditions. This is in agreement with the observations of multiple magma storage-crystallization zones at Merapi (e.g. Chadwick *et al.*, 2013; Costa *et al.*, 2013, Preece *et al.*, 2014; Peters *et al.*, 2017; Widiyantoro *et al.*, 2018), where different minerals are stable at different conditions: the OH-rich apatite in Amph likely grew from a H_2O-rich melt at greater depth, compared to the OH-poor crystals in Cpx, Pl and Gm (see calculations below).

The most significant compositional difference between the 2006 and 2010 apatite is the Cl-rich zones that were only observed from the rims of the microlites in 2006 rocks (Fig. 3), but not from any crystal in 2010 rocks (Fig. 4). The Cl-rich zones in 2006 apatite have length of ~3–7 μm, and appear only parallel to the long directions of the crystals, i.e. nearly parallel to the crystal c-axis (//c) (see interpretations in Discussion section). F zoning was found in the rim of one apatite microlite from 2006 (Fig. 3), whereas there seems to be no zoning or heterogeneity of OH. Scanning ion images acquired from some crystals show abnormally high OH/F/Cl intensities at the cracks and/or analysis positions of EPMA, which more likely reflect interferential signals due to microtomography/damage on the sample surface, rather than zoning (Figs 3 and 4).

CO_2

Apatite crystals in Cpx, Pl and groundmass of 2006 and 2010 show a similar range of CO_2 concentrations between 40–900 ppm (detection limits: ~20 ppm; Table 1). Two crystals in 2010 Amph show the highest CO_2 contents of ~2400 ppm and ~16 000 ppm, respectively (Fig. 5a; Table 1). We were not able to determine the CO_2 for the amphibole-hosted apatite from 2006, because the only crystal at such textural position in our samples were analysed with SIMS before (for H_2O, F, Cl and S), leaving insufficient space for the later analysis of CO_2.

Sulfur

Sulfur concentrations in apatite (measured by SIMS) from the two eruptions show an overlapping range, where the apatite in Amph shows higher S (2006: ~1510 ppm; 2010: ~900–3120 ppm) than the apatite in Cpx, Pl and groundmass (2006: ~190–1300 ppm; 2010: ~170–1750 ppm) (Table 1). Most crystals show oscillatory S zoning with narrow (<1–5 μm in width) S-rich bands (~500–1000 ppm S) at their mantles/rims (Figs 3 and 4). S in apatite can have multiple valances (S^{2-}, S^{1+}, S^{4+}, S^{6+}) depending on the oxidization condition of the magmatic system (Konecke *et al.*, 2017, 2019), i.e. mainly S^{2-} at/below FQM buffer (fayalite–magnetite–quartz buffer), and > 95% S^{6+} out of the total S at ≥FMQ + 1·2.

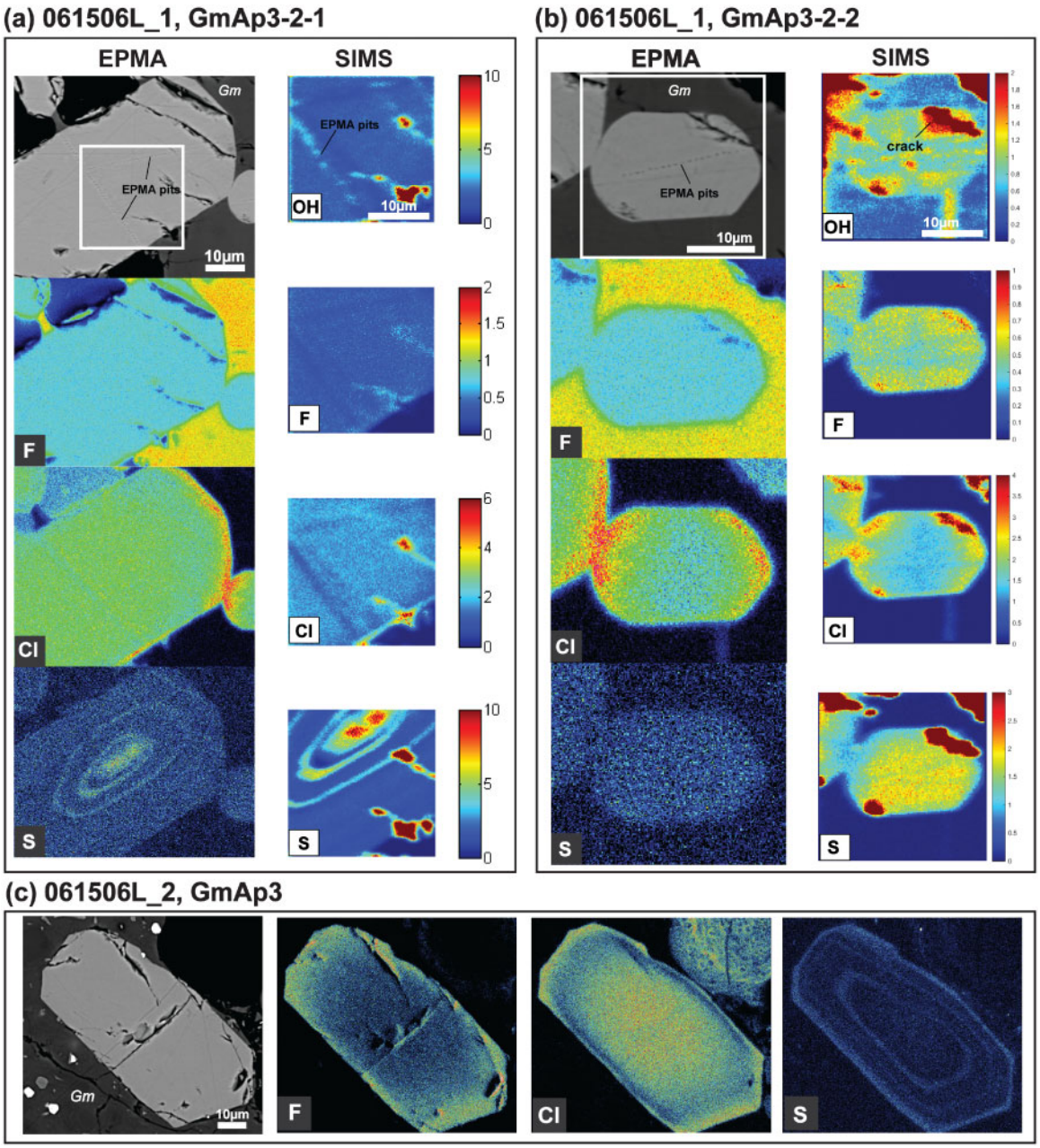

Fig. 3. Compositional distribution of F, Cl, S and OH in the groundmass apatite of 2006, shown in X-ray maps from EPMA analyses (panels a–c), and secondary ion maps from SIMS analyses (panels a and b) (see crystal labels in Table 1). Most crystals show Cl-rich rims (red colour, higher concentration; blue colour, lower concentration) nearly parallel to the c-axes, but not parallel to the a-axes (panels a–c). One crystal shows high F at the rim (panel c). There is no obvious zoning of OH. Some of the secondary ion maps for $OH^-/Cl^-/F^-$ show abnormally high or low signals at the cracks or pit locations of previous EPMA analyses (panels a and b), likely reflecting artefacts from analyses (see text). Most crystals show oscillatory S zoning (panels a, c).

Given the oxidization condition of Merapi magmas at ~FMQ + 0·6 to +2·2 above 400 MPa (Gertisser, 2001) and ~NNO + 1 (NNO = nickle–nickle oxide buffer) in the shallow reservoir (Erdmann *et al.*, 2016), and a much more favorable substitution of S^{6+} than S^{2-} into apatite (Kim *et al.*, 2017), there should be a larger proportion of S^{6+} than the S of other valences in apatite from this study (see discussion). There are multiple ways to incorporate S^{6+} at the tetrahedral site of the apatite structure (see review by Pan & Fleet, 2002). Electron microprobe analysis of crystals from this study show strong positive correlations between S-Na and S-Si concentrations, reflecting a dominant substitution reaction as: $S^{6+} + Na^{+} + Si^{4+} + 2Ce^{3+} \Longleftrightarrow 3P^{5+} + Ca^{2+}$ (Parat *et al.*, 2011).

Non-volatile elements

The apatite in Amph of 2006 and 2010 are much lower in Ce_2O_3 (0·01–0·03 wt %) than those included in anhydrous minerals and in the groundmass (0·1–0·3 wt %) (Fig. 6; see data in Supplementary Data Table S3).

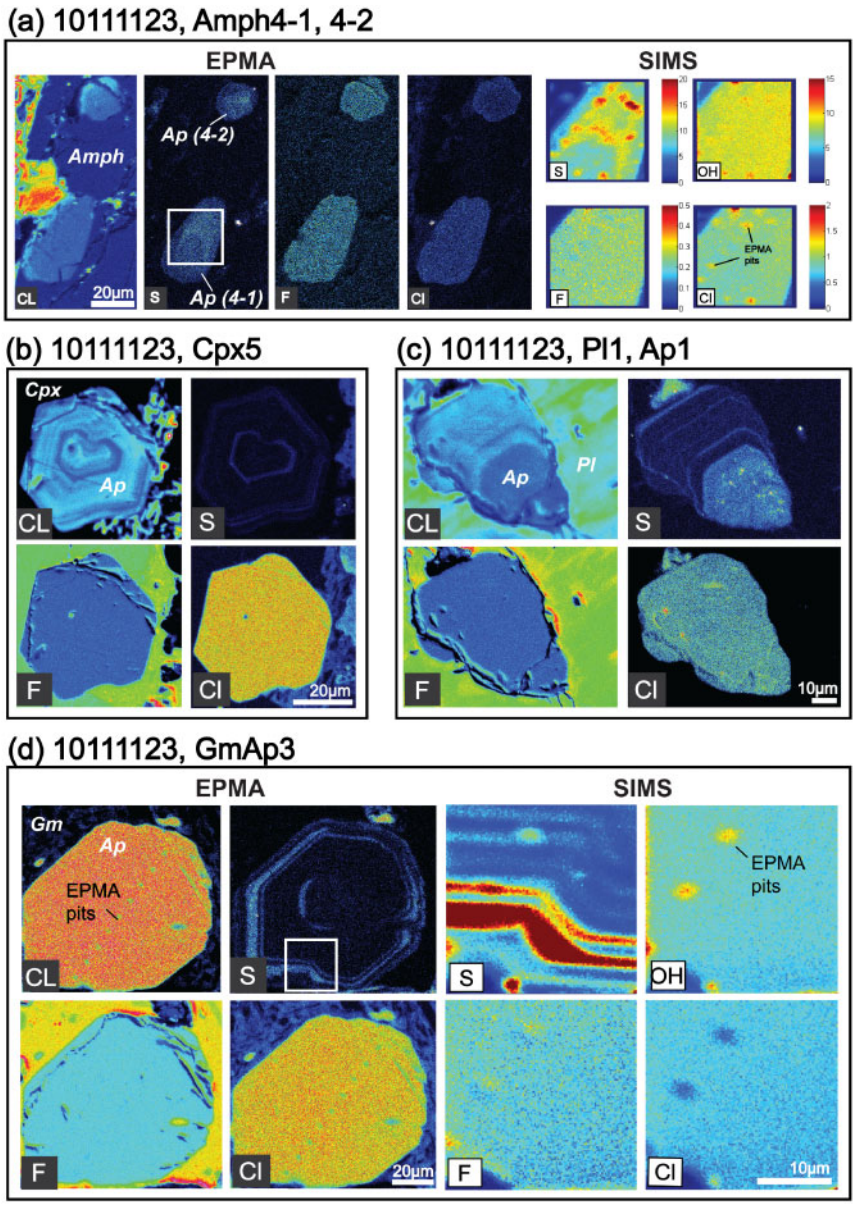

Fig. 4. Compositional distribution of F, Cl, OH, and S in the 2010 apatite: (a) included in Amph, (b) included in Cpx, (c) included in Pl, and (d) in the groundmass (see crystal labels in Table 1). Most crystals show oscillatory S zoning (panels b–d), but the crystal in Amph (panel a) shows higher S at the core than the rim. There is no obvious zoning of Cl/F/OH. Some maps for OH^- show abnormal signals at the cracks or pit locations of previous EPMA analyses, as was observed from the 2006 apatite (Fig. 3).

Considering that Ce is an incompatible element and its partitions into apatite is more favorable at lower *T*s with more silicic melts (Watson & Green, 1981), the Ce-rich apatite in Cpx/Pl/Gm should have grown from either cooler or more silicic melts (or both), compared to the Ce-poor apatite in Amph. This is also in agreement with the multiple *P–T–X* conditions reflected by the bimodal distribution of H_2O-CO_2-F in these crystals (see above). The Ce-poor crystals show high S contents (Fig. 6c), consistent with those observed in CL images (reflecting intensities of REEs) and x-ray maps of S where low REE intensities correspond to high S (Fig. 4). This implies that the incorporation of Ce and REEs into these crystals were not dominated by the substitution reaction shown above for S.

COMPOSITIONS OF MELTS

With volatile compositions determined for apatite, we calculate the melt H_2O–CO_2 budgets following the method of Li & Costa (2020). To carry out these calculations we need to know halogen concentrations in the melt that equilibrated with apatite, and the temperature. In this section we report the abundances of F, Cl and also major/minor elements in the melt, determined from analysis of the bulk rocks, interstitial glass, and

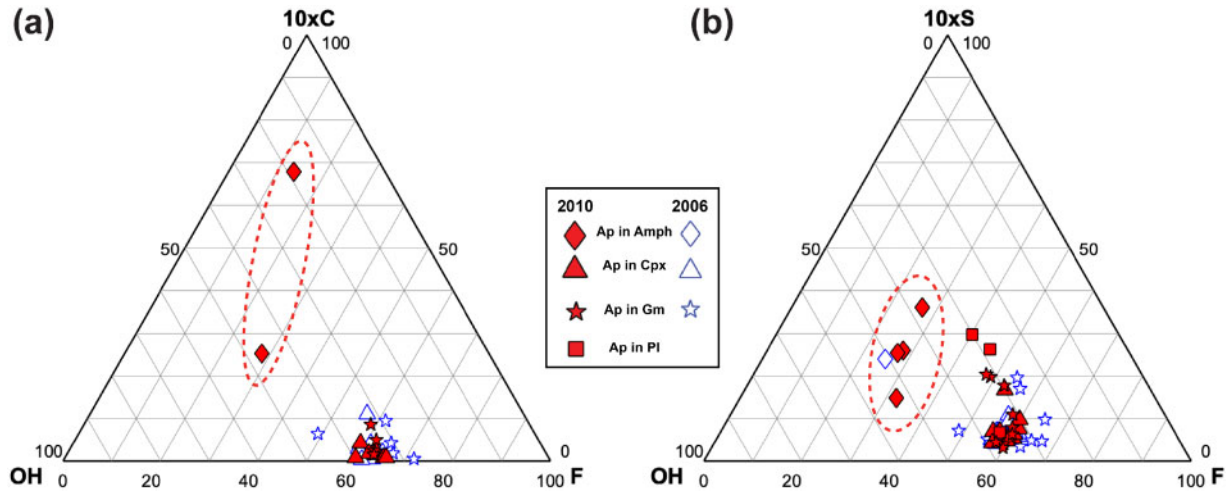

Fig. 5. (a) C–OH–F and (b) S–OH–F ternary diagrams for apatite crystals of the 2006 and 2010 eruptions (see legend). C and S concentrations were multiplied by 10 for ease of comparison. Apatite crystals in 2010 amphibole (red diamonds within areas marked in red dashed curves) show higher OH, C and S than the rest of crystals (in Cpx, Pl and groundmass) from the two eruptions. CO_2 data was not obtained from any crystal in 2006 amphibole nor in the 2006 and 2010 plagioclase, due to their limited numbers in the investigated rocks.

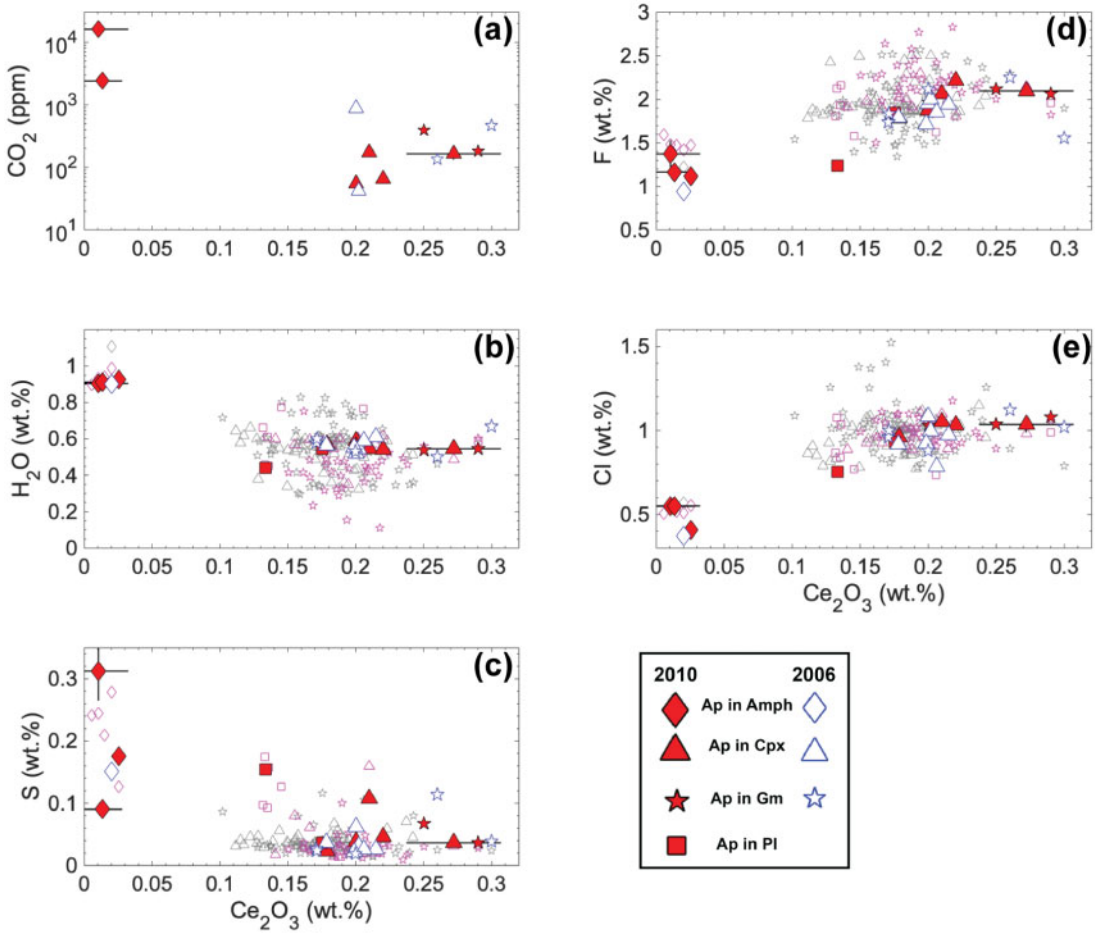

Fig. 6. Ce_2O_3 concentrations in apatite (by EPMA) vs (a) CO_2, (b) H_2O, (c) S, (d) F and (e) Cl (by SIMS; see symbol legend at the bottom; see data in Supplementary Data Table S3). The CO_2-, H_2O- and S-rich crystals in Amph (marked in diamonds) are much lower in Ce than the crystals at other textural positions. The concentrations of H_2O, F, Cl and S determined by SIMS are within the ranges of those acquired for a larger number of crystals using EPMA (crystal textural positions marked in same symbol shapes as used for crystals analysed by SIMS, but in different colors: 2010, empty with pink edges; 2006, empty with grey edges). Error bars show ±1 s.d. of the concentrations determined by SIMS (for volatiles) and by EPMA (for Ce).

Table 2: Composition of the Cpx-hosted glass inclusions measured using EPMA

		Concentration (wt %), normalized to 100% anhydrous											Concentration (ppm)	
Eruption	Label	SiO_2	TiO_2	Al_2O_3	FeO*	MnO	MgO	CaO	Na_2O	K_2O	P_2O_5	Total	Cl	S
2006	**cpx7_incl1**†	**69·13**	**0·48**	**16·39**	**2·13**	**0·13**	**0·61**	**1·60**	**4·93**	**4·48**	**0·11**	**94·78**	**2536**	**205**
2006	**cpx4_incl3**	**65·59**	**0·51**	**16·22**	**3·03**	**0·16**	**0·32**	**1·09**	**6·94**	**6·01**	**0·13**	**96·94**	**2377**	**104**
2006	**cpx4_incl3**	**65·87**	**0·43**	**15·99**	**2·99**	**0·13**	**0·29**	**1·04**	**6·98**	**6·12**	**0·15**	**96·62**	**2611**	**81**
2006	**cpx4_incl3**	**65·50**	**0·40**	**16·12**	**3·10**	**0·15**	**0·32**	**1·13**	**7·11**	**6·07**	**0·10**	**96·60**	**2487**	**124**
2006	**cpx3-incl1**	**66·25**	**0·39**	**17·10**	**2·85**	**0·16**	**0·34**	**1·13**	**5·38**	**6·26**	**0·14**	**99·59**	**2059**	**124**
2006	pair-clB-incl1	68·12	0·46	16·55	1·97	0·08	0·81	2·28	4·69	4·88	0·16	94·91	2472	121
2006	pair-clB-incl1	68·25	0·42	16·94	2·12	0·10	0·48	1·68	4·86	4·98	0·17	95·76	2504	184
2006	pair-clB-incl2	68·07	0·41	16·12	2·75	0·13	0·37	0·96	4·96	6·11	0·13	99·99	2842	18
2010	**cpx5_incl2**	**65·98**	**0·59**	**16·62**	**4·03**	**0·19**	**0·41**	**2·19**	**4·52**	**5·30**	**0·17**	**96·38**	**2649**	**68**
2010	**cpx6_incl2**	**68·03**	**0·53**	**15·66**	**3·74**	**0·15**	**0·54**	**1·36**	**4·84**	**5·11**	**0·05**	**97·51**	**2549**	**80**
2010	**cpx6_incl2**	**68·04**	**0·50**	**15·89**	**3·69**	**0·12**	**0·46**	**1·20**	**4·76**	**5·25**	**0·09**	**97·57**	**2491**	**172**
2010	**cpx6_incl4**	**68·34**	**0·45**	**16·77**	**2·61**	**0·07**	**0·38**	**1·24**	**4·93**	**5·12**	**0·11**	**97·33**	**2870**	**532**
2010	**cpx6_incl5**	**67·19**	**0·58**	**16·29**	**2·96**	**0·13**	**0·18**	**0·71**	**6·31**	**5·44**	**0·21**	**96·35**	**2697**	**258**
2010	**cpx6_incl5**	**67·52**	**0·62**	**16·45**	**2·78**	**0·16**	**0·26**	**0·78**	**5·78**	**5·53**	**0·12**	**95·05**	**2792**	**222**
2010	**cpx6_incl5**	**68·47**	**0·47**	**16·88**	**3·02**	**0·13**	**0·23**	**0·77**	**4·31**	**5·58**	**0·14**	**94·31**	**2756**	**242**
2010	**cpx6_incl5**	**67·76**	**0·41**	**16·50**	**2·36**	**0·08**	**0·17**	**0·72**	**6·31**	**5·57**	**0·13**	**95·25**	**2474**	**117**
2010	cpx-opx-pair1-incl1	67·29	0·47	15·97	3·61	0·16	0·26	1·67	4·41	6·09	0·07	98·46	1823	214
2010	cpx-opx-pair1-incl2	65·44	0·42	17·26	3·88	0·18	0·53	1·90	4·57	5·73	0·09	98·49	2229	33

*Total Fe as Fe^{2+}.
†Data marked in bold were acquired for melt inclusions hosted by Cpx crystals that also contain apatite. Mean Cl concentrations in these melt inclusions were considered as representative of Cl contents in the melt that equilibrated with Cpx-host apatite.

glass inclusions (in Cpx) in this study and from the literature, combined with a series of calculations. The temperature derived from multiple calculation methods are reported in following sections.

Major and minor elements

The SiO_2 content increases from 54–55 wt % in the bulk rocks, through 65–69 wt % in the Cpx-hosted MIs (Table 2), to 68–72 wt % in the interstitial glass (Table 3). The MIs analysed in this study and the majority of those from the literature have $\geq$64 wt % SiO_2 (Fig. 7; Costa *et al.*, 2013; Nadeau *et al.*, 2013; Preece *et al.*, 2014). The exceptions are some MIs hosted by amphibole from unknown eruption(s) (Nadeau *et al.*, 2013) which show 52–58 wt % SiO_2, and apparently lower Mg and higher Ca and P compared to the bulk rocks, implying the MIs may be formed by melts that are compositionally different from those emitted from 2006 and 2010 eruptions. To better evaluate the range of liquid compositions from the Merapi system, we subtracted the phenocrysts from the bulk rock of the 2010 eruption, and obtained a calculated groundmass that has ~58 wt % SiO_2, and its major-element composition follows the linear trend between bulk rocks and the interstitial glass in Harker diagrams (Fig. 7). The liquid compositions lying on the linear trends between the bulk rocks and interstitial glass (Supplementary Data Table S6) were used in the amphibole-liquid geothermobarometry calculations as described in the next section.

F and Cl

F concentrations in 2010 bulk rocks are below the detection limit of the applied technique (see methods), i.e. $\leq$ 0·01 wt %, and thus they were not considered hereafter. F concentrations in 2006 and 2010 interstitial glass are ~700–900 ppm, within the range of data from the literature (2010 glass: 180–2640 ppm; 2006 glass: <2350 ppm; Preece *et al.*, 2014). F concentrations in MIs from the literature also show a broad range, i.e. 140–2390 ppm for 2010, and 40–2050 ppm for 2006 (Preece *et al.*, 2014), but these values do not seem to show any obvious variation trend with melt evolution (Fig. 8b).

Cl concentrations measured from 2010 bulk rocks are 500–700 ppm, overlapping with those in 2010 ash samples (i.e. 550–1120 ppm; Borisova *et al.*, 2013). The amphibole-hosted primitive MIs from unknown eruptions (Nadeau *et al.*, 2013) show higher Cl contents than 2010 bulk rocks, likely reflecting different source magmas as were also seen from their major element compositions (see above). The interstitial glass of 2006 and 2010 contain similar Cl concentrations of 1500–1700 ppm, within the range of literature values (i.e. 900–3550 ppm for 2010, and 1000–2920 ppm for 2006; Preece *et al.*, 2014), but lower than the Cl contents in MIs that we analysed (i.e. 1820–2870 ppm), and from the literature (i.e. 2060–5130 ppm; Nadeau *et al.*, 2013; Preece *et al.*, 2014). The lower abundances of Cl in the interstitial glass than in MIs indicates Cl loss from our samples, likely due to Cl partitioning into vapor/fluid phase(s) at low pressures before/during eruption (e.g. Webster *et al.*, 2009; Allard, 2010; Preece *et al.*, 2014). Using the Cl solubility model of Webster *et al.* (2015), we find that the interstitial glass from the two eruptions (at 1 bar) could contain >4500 ppm Cl, meaning that the 'missing' portion of Cl likely went into a hydro-saline liquid (rather than a vapor), which is supported by Li enrichment in melt inclusions that reflect possible re-equilibration with a Li-rich brine phase (Preece *et al.*, 2014). The Cl exsolution into hydro-saline liquids may occur at ~5 km

Table 3: Representative major elements concentrations (wt %) of the bulk rocks, matrix glass and minerals, and calculated groundmass

	Data source	SiO_2	TiO_2	Al_2O_3	FeO*	MnO	MgO	CaO	Na_2O	K_2O	P_2O_5	Total (anhydrous)	
2006 Glass (N = 5)	This study	72·48	0·53	13·96	2·47	0·10	0·19	0·60	3·62	5·94	0·11	100·00	
2010 Glass (N = 3)	This study	68·73	0·57	15·97	3·10	0·13	0·37	1·70	3·77	5·43	0·23	100·00	
2010 Bulk rock	[1]	54·43	0·77	19·10	8·30	0·20	2·56	8·60	3·71	2·02	0·32	100·00	
Minerals from 2010 rocks		SiO_2	TiO_2	Al_2O_3	FeO*	MnO	MgO	CaO	Na_2O	K_2O	P_2O_5	Total	Modal abundance (in volume)
Pl†	[2]	53·93	0·00	28·83	0·51	0·00	0·00	11·35	4·61	0·34	0·00	99·56	25%
Cpx	[3]	51·90	0·36	2·09	8·83	0·64	14·73	20·83	0·35	0·01	0·00	99·74	5.9%
Mgt	[1]	0·10	9·28	2·93	78·01	0·90	2·66	0·00	0·00	0·00	0·00	93·88	2.0%
Opx	[3]	53·87	0·15	0·75	18·40	1·34	24·23	1·45	0·02	0·01	0·00	100·22	0.5%
Amph	[1]	39·46	2·68	12·44	12·89	0·27	12·81	11·60	3·08	0·95	0·00	96·18	0.4%
Ap	This study	0·20	0·00	0·00	0·00	0·00	0·35	54·50	0·08	0·00	41·40	96·53	0.3%
Ol	[1]	37·81	0·00	0·00	25·97	1·16	34·06	0·12	0·00	0·00	0·00	99·12	$\leq$0.1%
Biot	[1]	36·99	5·22	14·36	15·24	0·25	14·45	0·00	0·84	8·79	0·00	96·14	$\leq$0.1%
Calc, groundmass (2010)‡		58.18	0·57	18·37	6·89	0·19	2·18	6·47	3·95	2·93	0·27	100·00	66%

*Total Fe as Fe^{2+}.
†Compositions of minerals and bulk rocks were normalized to 100% (anhydrous) to calculate the groundmass composition (see text).
‡Calculation for the groundmass composition is described in the main text. Modal abundances of minerals were reported by [1].
Data sources: [1] Costa *et al.* (2013); [2] Cheng & Costa (2019); [3] Erdmann *et al.* (2016).

depth (Nadeau *et al.*, 2013), or at the conduit level where a hydrothermal system has been detected by electrical resistivity tomography (Byrdina *et al.*, 2017).

Given the halogen loss from the interstitial glass and bulk rocks, we did not use their concentrations for any calculation. Instead, we use the MI data from our analyses and from the literature, together with a fractionation model (see below) to estimate halogen contents of the less fractionated liquids. First, we use the MIs of 2010 reported by Preece *et al.* (2014) that have similar SiO_2 concentrations to the interstitial glass (i.e. ~68 wt %) as the representative of the most differentiated melts, which have on average ~2810 (± 250) ppm Cl, and ~860 (± 200) ppm F. With these values, we calculated the halogen contents of the less differentiated melts, using a Rayleigh fractionation model (cf. Philpotts & Ague, 2009):

$$C_i^l = C_i^o \cdot \varphi^{\overline{D}_i - 1} \quad (7)$$

where C_i^l and C_i^o are the concentrations of i (= F, Cl) in the residual and the initial melts respectively, φ is the mass fraction of the residual melts, and $\overline{D}_i$ is the bulk distribution coefficient of i between crystals and the melt. $\overline{D}_i$ in Eq. 7 was calculated using

$$\overline{D}_i = \sum D_i^{c/m} \cdot w_i^c \quad (8)$$

where $D_i^{c/m}$ is distribution coefficient of i between mineral c (= Cpx, Opx, Pl, Amph, Ol, Ap; Table 4) and the melt, and w_i^c is the fraction of the modal abundance of mineral c out of that of all crystals.

Using $D_i^{c/m}$ measured from previous experiments (Table 4), and the modal abundances of minerals in Merapi 2010 rocks (Costa *et al.*, 2013; Table 4), we find $\overline{D}_F \cong 0{\cdot}382$ and $\overline{D}_{Cl} \cong 0{\cdot}050$. The φ value of the residual liquid was calculated using K_2O concentrations in residual and initial liquids, where potassium is assumed to be perfectly incompatible ($\overline{D}_K \approx 0$). The calculated φ values are 0·38 (±0·02) for the interstitial glass, and 0·70 (±0·03) for the groundmass (Table 5). The difference (of ~0·32) between the two φ values should reflect the extent of microlite crystallization before the 2010 eruption, which matches with the microlite crystallinity observed in rocks that were emitted from same eruption stage (in 2010) as our samples (Preece *et al.*, 2016).

Using the parameter values above and Eq. 7, we found that the 'hypothetical' crystal-free liquid (with composition equivalent to the basaltic-andesitic bulk rock) could have ~1120 ppm Cl, and ~470 ppm F, whereas the andesitic groundmass could have ~1600 ppm Cl, and ~600 ppm F (Table 5). Moreover, we found that the value of melt Cl/F increases with melt differentiation (e.g. from ~1·3 for the bulk rock, to ~1·7 for the interstitial glass), because Cl is more incompatible than F (Table 4). The Cl/F in melts calculated from the fractional model above can be compared with that yielded by apatite to evaluate whether a liquid was in equilibrium with a given apatite crystal (e.g. in Amph, Cpx, Pl and groundmass).

WATER IN PYROXENE AND PARTITION RELATION BETWEEN PYROXENES AND THE MELT

The Cpx and Opx crystals contain ~10–280 ppm, and ~30–70 ppm H_2O respectively (by SIMS; Supplementary Data Fig. S4; Supplementary Data Table S5). The Cpx of 2010 shows on average higher H_2O concentration (mean: ~87 ppm) than the 2006 Cpx crystals (mean: ~34 ppm). The highest H_2O in Cpx was ~280 ppm from a glomerocryst of 2010. Using the major-element compositions of Cpx and Opx, we calculated the partition

Table 4: Distribution coefficients $D_i^{c/m}$ for F and Cl between different minerals and the melt

Mineral	w†	$D_F^{c/m}$	$D_{Cl}^{c/m}$	Data sources
Pl	0·77	0·098	0·0014	[1]
Cpx	0·18	0·114	0·011	[2]
Opx	0·015	0·056	0·02	[2]
Amph	0·012	0·635	0·378	[2]
Ol	0·003	0·0026	0·0003	[3]
Ap*	0·012	25	4	This study
Calculated bulk distribution coefficients: $\overline{D}_F$= 0.382, $\overline{D}_{Cl}$= 0·050				

*Distribution coefficients calculated using the mean halogens contents of the melt inclusions (Table 2) and of the apatite in Cpx/Pl/Gm.
†Weight fraction of each mineral out of all crystals.
Data sources: [1] Dalou *et al.* (2012); [2] Dalou *et al.* (2014); [3] Hauri *et al.* (2006).

coefficients of H_2O between Cpx-melt ($D_{H_2O}^{Cpx-melt}$) and between Opx-melt ($D_{H_2O}^{Opx-melt}$) using Eqns. 5–6 (see above). We find $D_{H_2O}^{Cpx-melt} \approx$ 0·011–0·014 for the 2006 Cpx, and a wider range of $D_{H_2O}^{Cpx-melt}$ of 0·011–0·024 for 2010 Cpx. The calculated $D_{H_2O}^{Opx-melt}$ values are between 0·005 and 0·014. The calculated $D_{H_2O}^{Cpx-melt}$ and $D_{H_2O}^{Opx-melt}$ values and the concentrations of H_2O in pyroxenes determined by SIMS (see above) were used to estimate H_2O concentrations in the melt (see below).

CALCULATIONS ON TEMPERATURES

To calculate melt H_2O concentrations based on apatite-melt volatile partitioning, i.e. $K_{D\,OH-x}^{Ap-melt}$ (Eqns. 1 and 2), we need to know the temperature of apatite-melt equilibration. The equilibrium temperature can be constrained by mainly two methods: (1) calculation of apatite saturation temperature (AST) using existing empirical equation (e.g. Piccoli & Candela, 1994); and (2) calculation of the crystallization/equilibrium *T*s for minerals that host apatite inclusions. In this section, we report the ASTs calculated for the groundmass apatite, and the *T*s for the apatite in amphibole estimated using amphibole-liquid geothermobarometry of Putirka (2016). The *T*s for the apatite in Cpx and Pl were constrained by other methods, and are reported in the next section where we summarize all the parameter values used in calculations of melt H_2O contents.

Apatite saturation temperature

The empirical equation for calculating the apatite saturation temperature (AST; Piccoli & Candela, 1994) is expressed as: $\mathrm{AST} = \frac{26400C_{SiO_2}^{l} - 4800}{12.4C_{SiO_2}^{l} - ln\left(C_{P_2O_5}^{l}\right) - 3.97}$, where $C_{SiO_2}^{l}$ and $C_{P_2O_5}^{l}$ are the weight fractions of SiO_2 and P_2O_5 in the melt at the temperature at which apatite started to crystallize. We have noticed that the calculated AST is very sensitive to the melt P_2O_5 contents. As a result, calculations using the wide range of P_2O_5 concentrations determined for the dacitic–rhyolitic MIs from Merapi rocks (0·02–0·3 wt %; Fig. 7) would yield ASTs that span a wide range that may be biased from the real temperatures of apatite-melt equilibration. Considering this, we only use the measured interstitial glass compositions (Table 3) to calculate the AST, and consider them as rough estimates of temperatures at which the groundmass apatite equilibrated with the melt. The AST calculated for the groundmass apatite in 2010 and 2006 rocks are ~980°C and ~940°C, respectively. Errors in the calculated AST are ~10°C, considering errors in the concentrations of P_2O_5 (7–8% relative) and SiO_2 (<0·4% relative) from EPMA of the glass.

Amphibole-liquid geothermobarometric calculations

Amphibole has been widely used for constraining the magmatic temperatures and pressures (Hammarstrom & Zen 1986; Hollister *et al.*, 1987; Johnson & Rutherford 1989; Blundy & Holland 1990; Schmidt 1992; Holland & Blundy 1994; Anderson & Smith 1995; Anderson 1996; Ridolfi *et al.*, 2010; Ridolfi & Renzulli, 2012; Putirka, 2016). Here we use the amphibole-liquid geothermobarometer of Putirka (2016) and the amphibole-only geothermobarometer of Ridolfi & Renzulli (2012) to calculate temperatures and pressures (Table 6). Calculation with the amphibole-only method is straightforward, whereas that with the amphibole-liquid geothermobarometry requires compositions of the melt that equilibrated with amphibole to be known. The amphibole-melt equilibrium can be tested using a parameter that varies little at different *P–T–X* conditions, however we noticed that the parameter proposed by Putirka (2016), i.e. $K_{D\,Fe-Mg}^{Amph-melt}$, varies in a wide range from 0·16 to 0·38. Considering this, we have used another test parameter, i.e. $K_{D\,Al-Si}^{Amph-melt}$, which was proposed to be less varied with *T* (Sisson & Grove, 1993). To determine the values of $K_{D\,Al-Si}^{Amph-melt}$ at a wide range of *P–T–X* conditions, we have performed a least-squares regression on the experimental data reported in Sisson & Grove (1993) and from other studies (Scaillet & Evans, 1999; Pichavant *et al.*, 2002; Grove *et al.*, 2003; Rutherford & Devine, 2003; Costa *et al.*, 2004; Sato *et al.*, 2004). The calculated $K_{D\,Al-Si}^{Amph-melt}$ is equal to 0·96 (±0·04) (Supplementary Data Fig. S5), and was used to test the amphibole-melt equilibrium as shown below.

Using $K_{D\,Al-Si}^{Amph-melt}$= 0·96, we find that the 2006 and 2010 amphiboles with molar Al/Si = 0·34–0·39 should be in equilibrium with melts that have molar Al/Si = 0·35–0·41 (Table 6). Based on the linear correlation between Al/Si and SiO_2 of bulk rocks, melt inclusions and glass, the melt in equilibrium with amphibole should have ~54–59 (±2) wt % SiO_2, within the compositional range between bulk rocks and the groundmass, and less silicic than MIs (Fig. 9b; Table 2). Liquid compositions were determined from the SiO_2 values above and

Table 5: F and Cl concentrations of the melt calculated using a Rayleigh fractionation model

Melt	K_2O (wt %)	φ * (calc)	F (ppm)	Cl (ppm)	mole Cl/F
Differentiated melt†	5·38 ± 0·21§	0·36–0·40	860 (±200)	2810 (±250)	1·8 (±0·3)
Bulk rock	2·04 ± 0·02	1	480 (±170)	1120 (±100)	1·3 (±0·3)
Groundmass (calc)‡	2·7–3·1	0·68–0·72	600 (±210)	1580 (±140)	1·4 (±0·3)
MIs in Cpx (mean)	4·8–5·0 ¶	0·41–0·43	810 (±280)	2570 (±230)	1·7 (±0·3)

*Fraction of differentiated liquid (φ) calculated using Eq. 7 and the K_2O concentration in the melt, assuming φ =1 for bulk rock.
†K_2O concentration of the interstitial glass and halogens are the median F and Cl contents in glass inclusions.
(Preece *et al.*, 2014) with equivalent SiO_2 to the interstitial glass of the 2010 rocks.
‡Calculated from mass balance (Table 3).
§Values in bold from measurements, whereas the rest calculated from the Rayleigh fractionation model.
¶Calculated using Eq. 7 and the mean of Cl concentration in glass inclusions (Table 2).

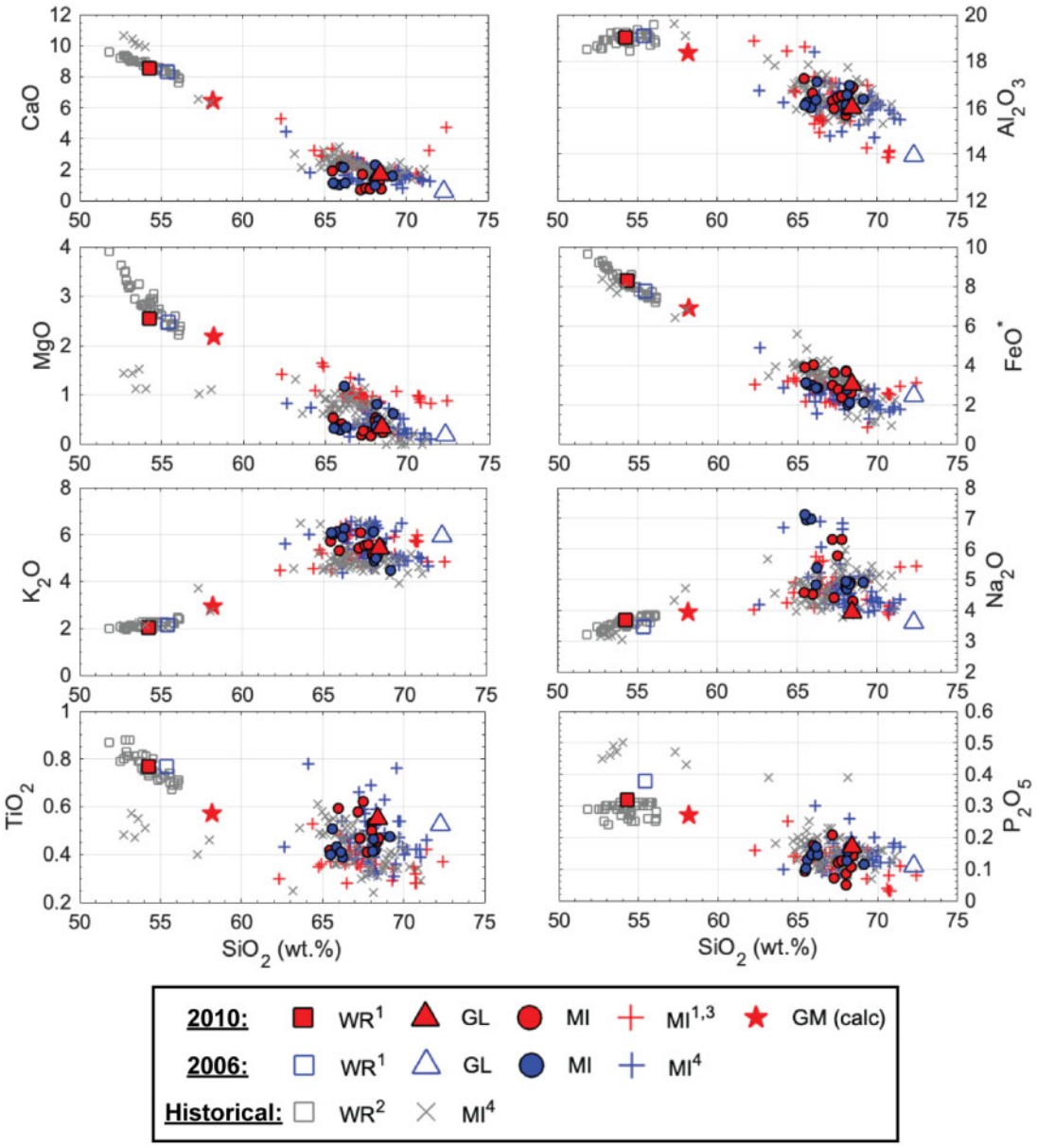

Fig. 7. Harker diagrams showing major element concentrations (wt %) of the interstitial glass (GL), melt inclusions (MI) and bulk rocks (WR) (see symbols in legend; see data in Tables 2 and 3). The calculated groundmass composition of 2010 (red stars) falls on the linear trends between the bulk rocks and the interstitial glass. Literature data are for the Cpx-hosted MIs of 2006[3,4] and 2010[1,3], and for the bulk rocks[2] and MIs (hosted by Cpx and Amph)[4] of historical eruptions. Data sources: [1]Costa et al, 2013; [2]Gertisser & Keller, 2003; [3]Preece *et al.*, 2014; [4]Nadeau *et al.*, 2013.

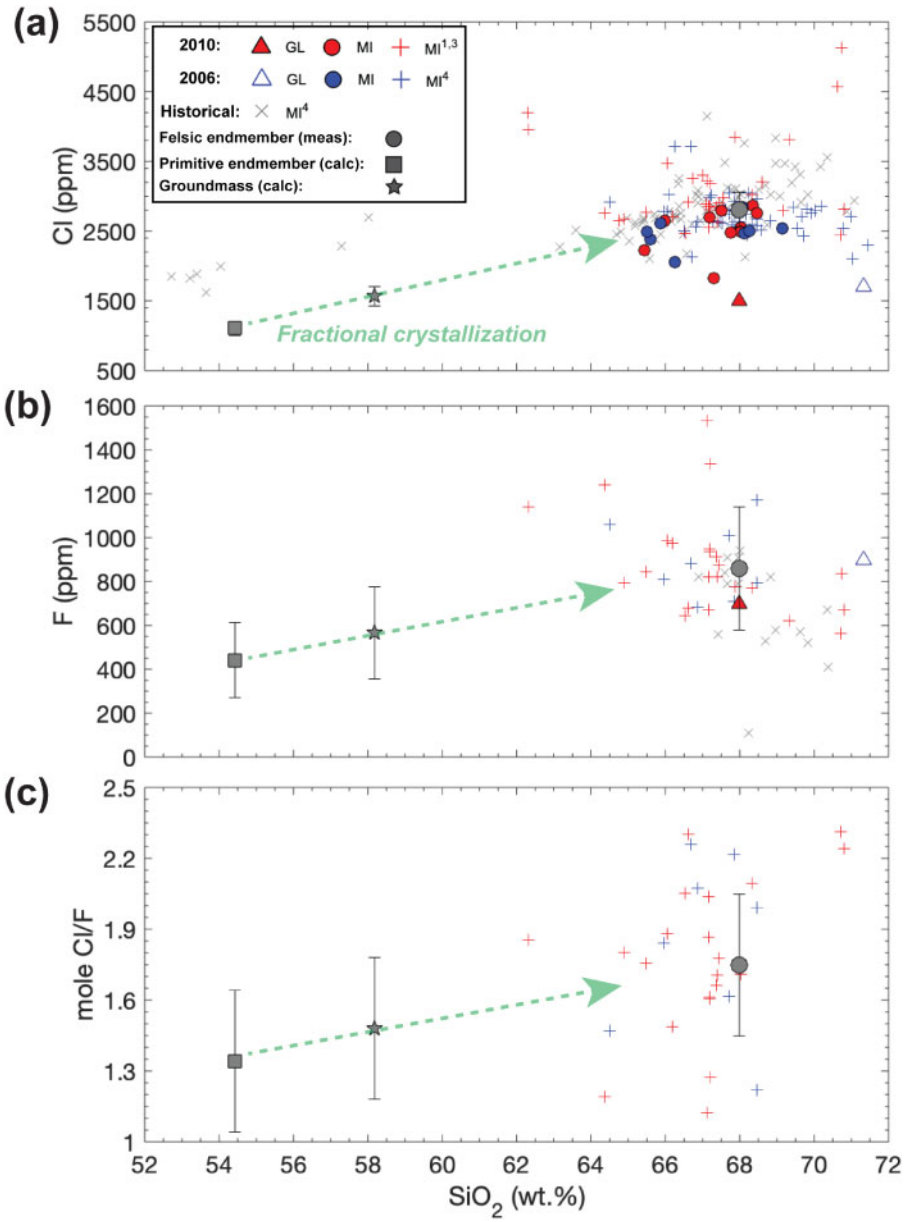

Fig. 8. Melt SiO_2 contents vs (a) Cl, (b) F, and (c) Cl/F of the melt (symbols same as in Fig. 7). The interstitial glass of 2006 and 2010 (triangles) have lower F and Cl concentrations than most melt inclusions, indicating some extent of Cl loss from the glass. We take the mean halogen contents measured for dacitic-rhyolitic MIs (grey circles) as the felsic endmember, and use these values and a Rayleigh fractionation model (see text) to calculate halogen contents of the phenocryst-free primitive melt (grey squares) and the groundmass (grey stars). The melt Cl/F values increase with fractional crystallization (panel c), because Cl is more incompatible than F (Table 5).

mass-balance calculations (Supplementary Data Table S6). Using the most precise equations among those suggested by Putirka (2016) (Eqns. 4a and 4b for T, and Eq. 7a for P), we find 950–1000°C, 580–850 MPa from 2010 amphibole, and 960–980°C, 560–590 MPa from 2006 amphibole (Table 6). These *P*–*T* estimates were calculated using 5 wt % H_2O in melt, and we notice that the value of melt H_2O has negligible effect on *T*, but larger effect on *P* (e.g. the *T* and *P* calculated using 6 wt% H_2O are higher of ~3°C, and 40–100 MPa than those reported above). Compared to *P*–*T* estimates above, calculations using the amphibole-only thermobarometry of Ridolfi & Renzulli (2012) show similar *T*s (≈ 950–1020 °C) but lower *P*s (≈340–510 MPa) (Table 6). Here we have taken the mean values of *T*s yielded by the two methods in the calculation of K_Ds for the apatite in amphibole.

PARAMETER VALUES USED FOR ESTIMATION OF MELT WATER CONTENTS

Parameter values needed for calculating the exchange coefficients $K_{D_{OH-x}}^{Ap-melt}$ (Eqs. 1 and 2) and melt water contents are: (1) apatite volatile composition (determined by SIMS), (2) melt Cl and/or F concentrations (calculated above with a Rayleigh fractionation model), and (3)

Table 6: Representative amphibole compositions determined by EPMA, and calculated temperatures and pressures

Eruption deposits	2010				2006	
Sample Label	10111123, Amph4		1011211A, Amph1		061506L_1, Amph5	
Concentration (wt %)	Max[§]	Min[§]	Max	Min	Max	Min
SiO_2	40·79	40·23	38·86	38·60	40·40	40·55
TiO_2	2·42	2·22	2·68	2·66	2·58	2·53
Al_2O_3	11·90	13·13	12·73	12·95	12·00	12·08
FeO*	12·95	13·45	12·69	12·87	10·98	10·95
MnO	0·23	0·22	0·25	0·26	0·22	0·25
MgO	12·65	12·8	12·82	12·63	13·41	13·02
CaO	11·75	11·62	11·63	11·80	11·43	11·32
Na_2O	2·35	2·37	3·41	3·39	2·28	2·35
K_2O	1·03	1·02	0·84	0·92	0·95	0·96
F	0·19	0·06	0·13	0·15	0·02	0·10
Cl	0·04	0·01	0·03	0·03	0·02	0·03
Calc H_2O*	1·77	1·85	1·79	1·78	1·84	1·79
Sum (hydrous)	98·07	98·98	97·85	98·05	96·14	95·93
Mg#	64	63	64	64	69	68
Mole Al/Si	0·34	0·38	0·39	0·39	0·35	0·35
Mole OH/Cl	179	562	241	233	362	272
Amphibole-liquid thermobarometry using equations from Putirka (2016) and the Al–Si equilibria						
Mole Al/Si	0·36	0·40	0·41	0·40	0·36	0·37
Melt SiO_2 (wt %)[†]	59	56	55	55	59	59
K_D(Fe–Mg)[‡]	0·31	0·33	0·31	0·31	0·26	0·26
T (°C) (Eq. 4a)	953	963	1001	1004	962	965
T (°C) (Eq. 4b)	954	965	977	976	981	980
P (MPa) (Eq. 7a)	580	720	840	850	560	590
P (MPa) (Eq. 7b)	366	462	470	466	380	390
Amphibole-only thermobarometry using equations from Ridolfi & Renzulli (2012)						
T (°C) (Eq. 2)	945	957	1013	1012	963	961
P (MPa) (Eq. 1b)	340	439	418	432	391	403
P (MPa) (Eq. 1c)	408	484	493	505	444	449
Mean values of *P* and *T* (calculated using equations of Putirka, 2016) and their variations [¶]						
T (°C) (Eqns. 4a, 4b)	959 (± 6)		990 (± 15)		972 (± 10)	
P (MPa) (Eq. 7a)	650 (± 70)		845 (± 5)		575 (± 15)	
OH–Cl partition between Amph-melt (following Humphreys *et al.*, 2009)						
K_D(Cl–OH)	0·281	0·290	0·220	0·224	0·240	0·244
Melt OH/Cl	50	163	53	52	87	67

*Total Fe as Fe^{2+}.
[†]Calculated melt SiO_2 concentration (relative error: ~ 4%) based on mole Al/Si in Amph, and K_D(Al–Si) =0.96 (Supplementary Data Fig. S5).
[‡]Equilibrium test parameter proposed by Putirka (2016): K_D(Fe–Mg) = 0·28 ± 0·11.
[§]Min & Max refer to the SiO_2 concentrations of the melts in equilibria with amphibole.
[¶]Errors in *T*s and *P*s calculated using the equations of Putirka (2016) are ~20–30 °C, and ~100–150 MPa, respectively.
*Calculated based on amphibole stoichiometry, following Ridolfi *et al.* (2010).

temperature. Given that apatite crystals appearing at different textural positions have distinct compositions of F–Cl–OH–C and Ce, they may have grown from melts that have different halogen contents and temperatures. Thus, we have used different values of parameters (2) and (3) in our calculations on apatite at different textural positions (summarized in Table 7).

Errors in parameter values were propagated to the calculated melt volatile contents (cf. Li & Costa, 2020; Li, 2019), including analytical errors in apatite volatile measurements (by SIMS), variations in melt halogen contents, and uncertainties in the formulation for $K_{D\,OH-Cl}^{Ap-melt}$ and $K_{D\,OH-F}^{Ap-melt}$. The uncertainty in the two formulations for K_Ds (30–50% relative; Li & Costa, 2020) contribute the largest error to the results, much larger than those induced by variations in melt Cl contents (~9%, relative; Table 5), and by a change in *T* of <50 °C. Given that melt water contents can be calculated using either $K_{D\,OH-Cl}^{Ap-melt}$ (with melt Cl) or $K_{D\,OH-F}^{Ap-melt}$ (with melt F), and the smaller error in $K_{D\,OH-Cl}^{Ap-melt}$ (30–40 %, relative) than $K_{D\,OH-F}^{Ap-melt}$ (40–50%, relative) (Li & Costa, 2020), we have mainly used $K_{D\,OH-Cl}^{Ap-melt}$ to calculate melt H_2O contents, and later to calculate melt CO_2 contents. Eventually the relative error in the calculated melt volatile contents are ~36–45% for H_2O, and ~38–45% for CO_2, considering uncertainties in $K_{D\,H_2O-CO_2}^{Ap-melt}$ (~13% relative; Riker *et al.*, 2018) and analyses of CO_2 in apatite. All the errors are reported in Table 7. It should be noted here that the $K_{D\,H_2O-CO_2}^{Ap-melt}$ value used in our calculations was determined from experiments at a temperature (1250 °C; Riker *et al.*, 2018) higher than those of Merapi melts, and

Table 7: Exchange coefficients (K_Ds) and melt H_2O–CO_2–S concentrations calculated for 2006 and 2010 (stage 4) eruptions (error: ± 1 s.d.)

Eruption	Ap textural position[†]	No.[*]	$K_{D\,OH-Cl}^{Ap-melt}$	$K_{D\,OH-F}^{Ap-melt}$	$K_{D\,Cl-F}^{Ap-melt}$	mole OH/Cl	mole OH/F	mole Cl/F	Melt H_2O (calc using Cl) wt %	±	Melt H_2O (calc using F) wt %	±	Melt CO_2 ppm	±	Melt S[§] ppm	H_2O–CO_2 Saturation pressure[‡] MPa
2006	in Amph [1]	1	0·090	0·018	0·196	108	116	1·1	8·0	2·6	5·1	2·8	n.d.	n.d.	665	n.d.
	in Cpx [2]	2	0·088	0·013	0·149	21	43	2·0	1·7	0·7	2·1	0·9	1814	852	37	330
		3	0·088	0·013	0·149	22	43	2·0	1·7	0·7	2·1	0·9	634	297	31	120
		4	0·087	0·014	0·156	23	47	2·0	1·9	0·8	2·3	1·0	468	216	22	90
		5	0·090	0·013	0·141	22	41	1·9	1·7	0·7	2·0	0·8	314	150	19	68
		6	0·089	0·013	0·148	24	45	1·9	1·9	0·8	2·2	1·0	113	53	18	47
		7	0·090	0·013	0·145	24	45	1·8	2·0	0·8	2·2	0·9	95	45	18	46
		8	0·090	0·013	0·145	28	48	1·7	2·4	1·0	2·4	1·0	62	29	23	50
		9	0·089	0·013	0·150	28	50	1·8	2·3	0·9	2·5	1·0	n.d.	n.d.	14	n.d.
		10	0·090	0·013	0·148	29	50	1·7	2·4	1·0	2·5	1·0	n.d.	n.d.	13	n.d.
		11	0·091	0·013	0·144	32	51	1·6	2·9	1·2	2·6	1·1	n.d.	n.d.	15	n.d.
		12	0·088	0·014	0·154	27	50	1·9	2·2	0·9	2·5	1·0	n.d.	n.d.	12	n.d.
		13	0·089	0·013	0·151	27	49	1·8	2·3	0·9	2·5	1·0	n.d.	n.d.	21	n.d.
	in Gm [3]	14	0·083	0·011	0·127	24	45	1·9	2·4	0·9	2·7	1·2	2420	998	87	406
		15	0·077	0·013	0·167	34	71	2·1	3·8	1·3	4·9	2·1	1670	740	22	280
		16	0·083	0·011	0·127	24	45	1·9	2·4	0·9	2·6	1·2	1020	400	16	177
		17	0·081	0·011	0·131	22	44	2·0	2·1	0·8	2·6	1·2	365	160	74	83
		18	0·084	0·011	0·127	30	49	1·7	3·1	1·2	3·0	1·3	115	50	21	110
		19	0·084	0·010	0·119	21	39	1·8	2·0	0·8	2·2	1·0	114	53	34	53
		20	0·079	0·012	0·150	30	59	2·0	3·2	1·1	3·8	1·7	n.d.	n.d.	15	n.d.
		21	0·079	0·012	0·149	30	58	2·0	3·1	1·1	3·8	1·6	n.d.	n.d.	13	n.d.
		22	0·083	0·011	0·128	29	49	1·7	3·0	1·1	3·0	1·3	n.d.	n.d.	11	n.d.
		23	0·084	0·010	0·120	24	42	1·8	2·4	0·9	2·4	1·1	n.d.	n.d.	15	n.d.
2010	in Amph [4]	24	0·100	0·018	0·182	65	77	1·2	2·4	0·8	4·7	2·6	24306	9500	2001	>1000
	in Amph [5]	25	0·083	0·015	0·185	79	108	1·4	5·0	1·6	4·7	2·6	8400	3190	343	≥800
	in Amph [5]	26	0·084	0·015	0·183	85	108	1·3	5·6	1·8	5·1	2·8	n.d.	n.d.	724	n.d.
	in Amph [5]	27	0·085	0·015	0·181	107	114	1·1	8·0	2·6	1·7	0·9	n.d.	n.d.	686	n.d.
	in Cpx [2]	28	0·087	0·014	0·156	23	46	2·0	1·8	0·8	2·3	1·0	809	375	24	147
		29	0·090	0·013	0·145	23	43	1·9	1·9	0·8	2·1	0·9	415	196	70	84
		30	0·090	0·013	0·143	23	43	1·9	1·9	0·8	2·1	0·9	283	134	17	66
		31	0·090	0·013	0·143	23	43	1·9	1·9	0·8	2·1	0·9	397	188	21	82
		32	0·089	0·013	0·149	23	44	1·9	1·9	0·8	2·2	0·9	344	161	17	73
		33	0·091	0·013	0·138	23	41	1·8	1·8	0·8	2·0	0·9	152	73	27	49
		34	0·089	0·013	0·142	20	40	2·0	1·5	0·6	1·9	0·8	138	66	34	41
		35	0·088	0·014	0·157	25	48	2·0	2·0	0·8	2·4	1·0	142	65	22	53
		36	0·088	0·014	0·154	27	50	1·9	2·2	0·9	2·5	1·1	n.d.	n.d.	13	n.d.
		37	0·090	0·013	0·147	25	46	1·8	2·0	0·9	2·3	1·0	n.d.	n.d.	16	n.d.
		38	0·089	0·013	0·148	24	45	1·9	1·9	0·8	2·2	0·9	n.d.	n.d.	14	n.d.
	in Pl [6]	39	0·081	0·011	0·142	29	55	1·9	2·8	1·0	2·6	1·4	n.d.	n.d.	21	n.d.
	in Pl [7]	40	0·089	0·015	0·165	26	51	2·0	2·2	0·7	2·2	1·2	n.d.	n.d.	110	n.d.
	in Pl [7]	41	0·091	0·014	0·152	24	45	1·9	1·9	0·7	2·7	1·5	n.d.	n.d.	131	n.d.

(continued)

Table 7: Continued

Eruption	Ap textural position[†]	No.[*]	$K_{D\,OH-Cl}^{Ap-melt}$	$K_{D\,OH-F}^{Ap-melt}$	$K_{D\,Cl-F}^{Ap-melt}$	mole OH/Cl	mole OH/F	mole Cl/F	Melt H_2O (calc using Cl) wt %	±	Melt H_2O (calc using F) wt %	±	Melt CO_2 ppm	±	Melt S[§] ppm	H_2O–CO_2 Saturation pressure[‡] MPa
	in Gm [3]	42	0·081	0·011	0·138	25	50	2·0	2·3	0·9	2·7	1·5	2040	850	27	330
		43	0·081	0·011	0·135	25	49	1·9	2·4	0·9	2·7	1·5	1160	500	40	200
		44	0·080	0·011	0·140	25	50	2·0	2·3	0·9	2·7	1·5	517	226	21	110
		45	0·080	0·011	0·141	25	50	2·0	2·3	0·8	3·0	1·7	335	145	76	88
		46	0·080	0·011	0·143	27	54	2·0	2·6	1·0	3·0	1·7	n.d.	n.d.	12	n.d.
		47	0·080	0·011	0·143	28	54	2·0	2·6	1·0	3·3	1·8	n.d.	n.d.	10	n.d.
		48	0·081	0·011	0·143	31	57	1·9	3·0	1·1	3·2	1·8	n.d.	n.d.	14	n.d.
		49	0·080	0·012	0·143	29	56	1·9	2·8	1·1	3·3	1·8	n.d.	n.d.	91	n.d.
		50	0·080	0·012	0·144	30	57	1·9	3·0	1·1	1·6	0·9	n.d.	n.d.	93	n.d.

*Crystal labels and compositions are shown in Table 1 (referring to No.).
[†]Different values of temperatures and melt halogen contents (Table 5) were used for calculations of apatite at different textural positions: [1] Ap in Amph (Al_2O_3: ~12 wt %) from 2006: 972°C, 1580 ppm Cl, 600 ppm F; [2] Ap in low-Al Cpx (Mg# = 74–76; Wo = 41–48) from 2006 and 2010: 970°C, 2570 ppm Cl, 810 ppm F; [3] Ap in Gm from 2006 and 2010: 940°C, 2810 ppm Cl, 860 ppm F; [4] Ap in *Amph1* (Al_2O_3: 12–13 wt %) from 2010: 990°C, 1120 ppm Cl, 480 ppm F; [5] Ap in *Amph4* (Al_2O_3: 11–13 wt %) from 2010: 959°C, 1580 ppm Cl, 600 ppm F; [6] Ap in *Pl3* ($An_{53–67}$) from 2010: 950°C, 2810 ppm Cl, 860 ppm Cl; [7] Ap in *Pl1* (An_{74}) from 2010: 975°C, 2570 ppm Cl, 810 ppm Cl.
[‡]Magma volatile saturation pressures calculated using the H_2O–CO_2 solubility model of Papale *et al.* (2006).
[§]Errors in the calculated melt S concentrations are ~7–16% relative, considering the analytical errors in S measurements for apatite (Table 1).

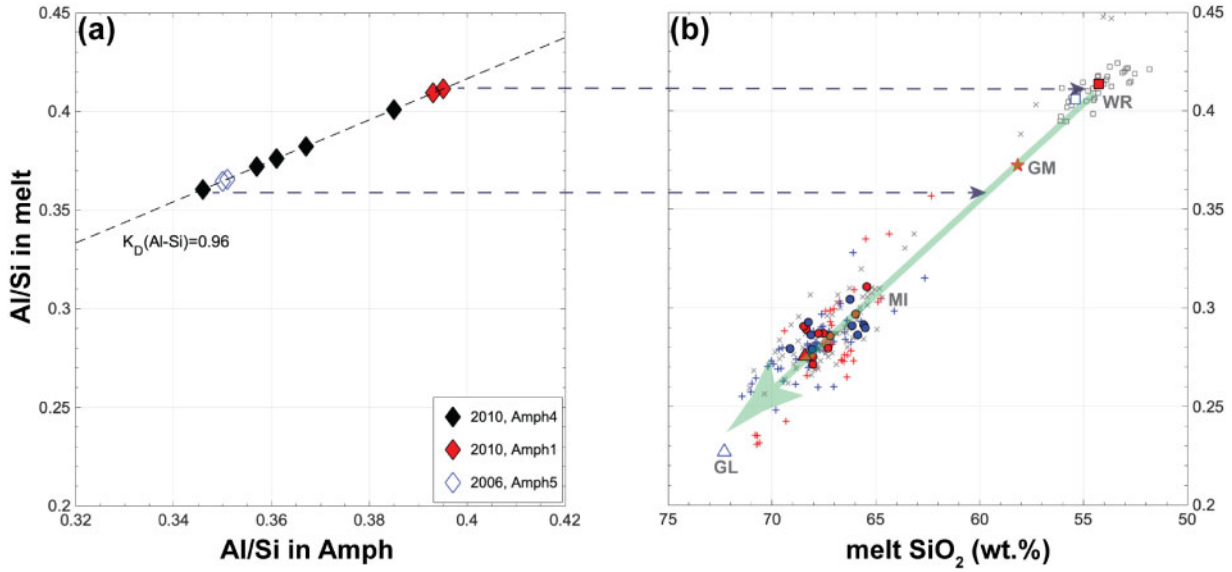

Fig. 9. (a) Molar Al/Si in amphibole (measured), plotted versus molar Al/Si calculated for the equilibrium melt using $K_{D_{Al-Si}}^{Amp-melt} = 0{\cdot}96$ (shown as the line slope); and (b) SiO_2 concentration vs molar Al/Si determined by EPMA analysis of the bulk rocks (WR), interstitial glass (GL), melt inclusions (MI), and calculated for the groundmass (GM) (see symbols and data sources in Fig. 7). The amphibole equilibrated with melts that have ~54–59 (±2) wt % SiO_2, i.e. less evolved than the Cpx-hosted MIs.

the relationship between $K_{D_{H_2O-CO_2}}^{Ap-melt}$ and *T* has yet to be determined. If there is a positive correlation between $K_{D_{H_2O-CO_2}}^{Ap-melt}$ and *T*, then the melt CO_2 contents calculated from this study would represent the highest values. Below we describe the parameter values used for calculations on the apatite in amphibole, clinopyroxene, plagioclase and groundmass (summarized in Table 7).

Apatite inclusions in amphibole

We have shown that the amphibole cores were in equilibrium with a liquid of ~59 (±2) wt % SiO_2 (equivalent to that in groundmass) at ~972°C for 2006, and ~54–59 wt % SiO_2 at 959–990°C for 2010 (Table 6). Errors in these *T* estimates are ~25 °C. These liquids should contain ~1120–1580 ppm Cl and 470–590 ppm F, as calculated from the Rayleigh fractionation model above (Table 5). These values were used in calculations on the amphibole-hosted apatite (Table 7).

Apatite inclusions in clinopyroxene

For calculations on the apatite in Cpx, we use the *T* inferred from the host Cpx, and halogen concentrations measured for glass inclusions. Here we only consider the low-Al Cpx that contains apatite inclusions, whereas the high-Al Cpx that grew from the deep reservoir is discussed below. Using Cpx-liquid thermometry of Putirka (2008, Eq. 33), and the composition of Cpx (near apatite inclusions) and Cpx-hosted MIs, we find *T*s between 960–970 (±50)°C assuming 2 wt % H_2O in the melt, and 970–980 (±50) °C assuming 1 wt % H_2O in the melt. These values are lower than the low-Al Cpx crystallization *T* (~1000°C) inferred from MELTS modelling (Costa *et al.*, 2013), and the Cpx-bulk rock equilibration *T* (1025–1058, ±50 °C) calculated by Preece *et al.* (2014)

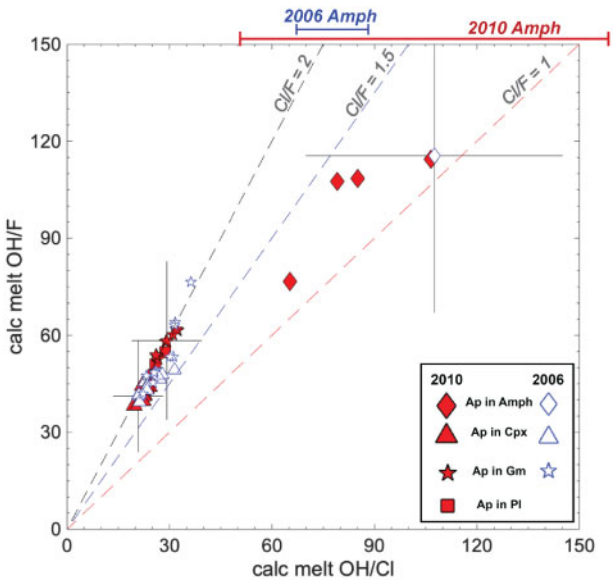

Fig. 10. Mole OH/Cl and OH/F of the melts that equilibrated with apatite (Table 7). Line slopes equal to the melt Cl/F values. Melt OH/Cl and OH/F calculated using the apatite in Amph are higher than those calculated using the apatite in Cpx, Pl and Gm. Melt OH/Cl values calculated from the Amph (marked on top; Table 6) and from their apatite inclusions show an overlapping range. Error bars show ±1 s.d. of OH/F and OH/Cl calculated for the melts.

using the Cpx-liquid thermometry of Putirka *et al.* (2003). The low-Al Cpx that contains apatite inclusions from this study (Wo = 41–48; Supplementary Data Table S5) has compositions within the range of those formed from phase equilibria experiments at 950–1000°C, down to ~925 °C (Erdmann *et al.*, 2016). Considering the various thermometry results described above and the experimental constraints of Erdmann *et al.* (2016), we

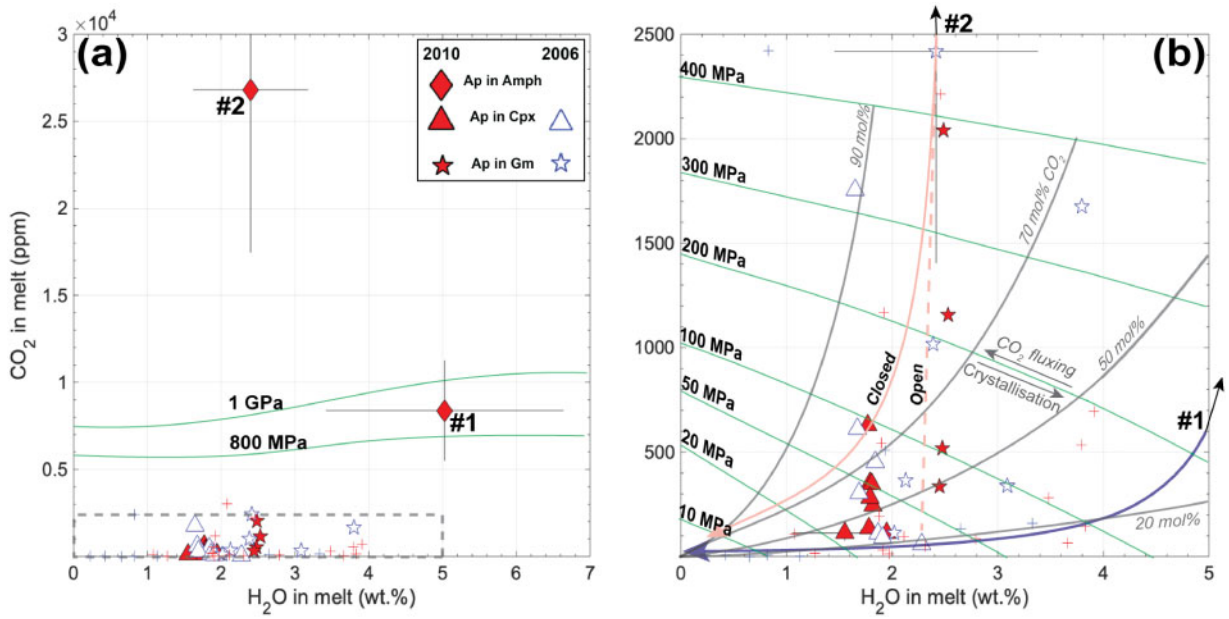

Fig. 11. H_2O vs CO_2 concentrations of the melt calculated using apatite (panel b as zoomed-in view of the grey dashed area in panel a). The melt in equilibrium with apatite in Cpx, Pl and Gm show similar abundances of H_2O and CO_2 with the Cpx-hosted glass inclusions from the literature (2010, red cross; 2006, blue cross; Preece *et al.*, 2014), but much less CO_2 than the melt in equilibrium with the apatite inclusions in Amph. Isobars and isopleths (showing a given mole fraction of CO_2 in fluids) were calculated using the H_2O–CO_2 solubility model of Papale *et al.* (2006). Degassing paths were modelled using initial volatile concentrations calculated from the apatite inclusions in Amph (#1, #2) for closed-system ('closed', solid lines) and open-system ('open', dashed line). Error bars show ±1 s.d. of the melt H_2O and CO_2 estimates (Table 7).

used $T \approx 970$°C to calculate the $K_D^{Ap-melt}_{OH-x}$ for the apatite in Cpx. Variations in T should be <50 °C which would only cause small changes in the calculated $K_D^{Ap-melt}_{OH-x}$ and melt H_2O contents of <30–40% relative (see above). For the melt halogen contents, we use ~2570 (±210) ppm Cl (i.e. the average concentration in Cpx-hosted MIs), and ~810 (±280) ppm F (calculated from the Rayleigh fractionation model above).

Apatite inclusions in plagioclase

We have only analysed three apatite inclusions in two plagioclase phenocrysts. The crystal that hosts two apatite inclusions (i.e. 'Pl1, Ap1' and 'Pl1, Ap2' in Table 1) is An_{74}, whereas the other one (i.e. 'Pl3' in Table 1) is $An_{53–67}$. Given the An values of plagioclase formed by phase equilibria experiments (Erdmann et al, 2016), i.e. An_{70} at 950–1000°C and An_{50} at 925–950°C, we use the mean T of 975°C for the apatite in 'Pl1' (of An_{70}), and 950°C for the other crystal in 'Pl3' (of $An_{53–67}$). Considering the similarity in T between the high-An 'Pl1' and the low-Al Cpx shown above, it is likely that the melts from which they grew have similar abundances of halogens, thus we use ~2570 ppm Cl and ~810 ppm F in our calculation. For the apatite in 'Pl3' that grew at lower T (≈950°C) from possibly more evolved melts, we use higher melt halogen contents (~2810 ppm Cl, ~860 ppm F) that are equivalent to those used in the calculation for the groundmass apatite reported below. The apatite in plagioclase were only used to calculate the melt H_2O contents but not melt CO_2, given a lack of data for CO_2 concentrations in these crystals (Table 1).

Groundmass apatite

The core of the groundmass apatite that we analysed likely equilibrated with liquids that are compositionally equivalent to, or less evolved than the interstitial glass. Here we take the lower value of AST calculated from the 2006 glass, i.e. 940 (±10) °C, and the mean concentrations determined for the dacitic-rhyolitic MIs from Merapi rocks (~2810 ppm Cl, ~860 ppm F) to calculate the melt H_2O–CO_2 contents. Considering the crystallization and halogen evolution in the melt with fractionation, the melt in equilibrium with the cores of these crystals in the groundmass could be actually hotter and contain less halogen compared to the interstitial glass. Therefore, calculations using the parameter values above likely give us the highest values of H_2O–CO_2 concentrations in the melt that equilibrated with the groundmass apatite.

CALCULATED MELT VOLATILE COMPOSITION

Calculated exchange coefficients (K_D), and melt OH/Cl and OH/F values

Using the determined apatite compositions and temperatures, we calculated the exchange coefficients (K_D) for OH–F and OH–Cl (Table 7). We found that the melt in equilibrium with apatite in Amph have mole fraction ratios of $\frac{X_{OH}^{melt}}{X_{Cl}^{melt}} \approx$ 65–108, $\frac{X_{OH}^{melt}}{X_{F}^{melt}} \approx$ 77–116, and $\frac{X_{Cl}^{melt}}{X_{F}^{melt}} \approx$ 1·1–

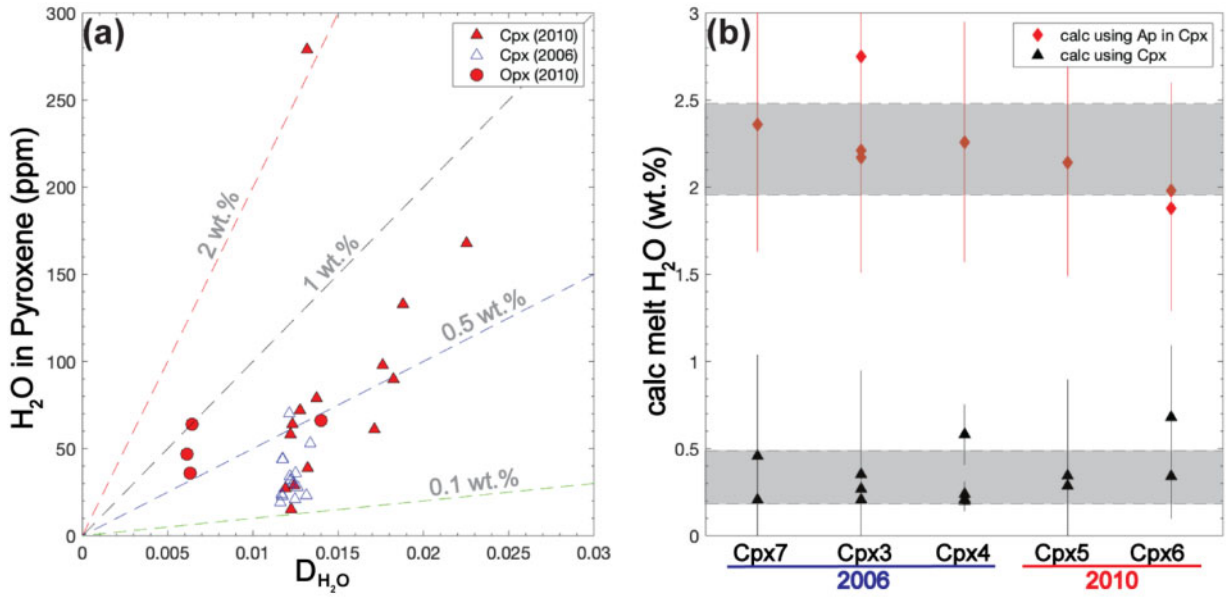

Fig. 12. (a) H_2O concentrations of clinopyroxene (triangles) and orthopyroxene (circles) (measured by SIMS), plotted versus the partition coefficients of H_2O (calculated using Eqns. 5 and 6). Line slopes (dashed lines) represent the calculated H_2O contents of the melt. (b) Melt H_2O estimates using five Cpx crystals and their apatite inclusions (multiple data points at the same location of the *x*-axis reflect multiple analyses at different positions on the same crystals). Melt H_2O contents calculated from apatite are generally >3 x higher than those calculated from Cpx (95% confidence intervals marked in grey fields in panel b; see data in Table 7 and Supplementary Data Table S5). Error bars show ±1 s.d. of H_2O concentrations calculated for the melt.

1·4. In contrast, the melt in equilibrium with the rest of apatite crystals (in Cpx, Pl, groundmass) have lower $\frac{X_{OH}^{melt}}{X_{Cl}^{melt}}$ (≈20–36) and $\frac{X_{OH}^{melt}}{X_{F}^{melt}}$ (≈38–76), but higher $\frac{X_{Cl}^{melt}}{X_{F}^{melt}}$ (≈1·6–2·1) (Table 7; Fig. 10). Comparison of melt Cl/F values calculated from apatite with those calculated from the Rayleigh fractionation model (Table 5) shows that the apatite in Amph equilibrated with basaltic–andesitic to andesitic melts, whereas apatite in Cpx/Pl/Gm equilibrated with more evolved melts varying from dacitic to rhyolitic. In addition, melt OH/Cl values ($\frac{X_{OH}^{melt}}{X_{Cl}^{melt}}$) calculated using the exchange coefficient for OH–Cl between amphibole and melts (Eq. 4; Humphreys *et al.*, 2009) show a wide range between 50 and 163 (Table 6), which includes the values calculated from the apatite included in Amph (Fig. 10). The good match of melt Cl/F and OH/Cl values calculated using the multiple methods above indicates that the parameter values used in calculations on apatite are reasonable.

Calculated melt H_2O and CO_2 concentrations

The 2006 and 2010 melts that equilibrated with the apatite in anhydrous minerals/groundmass show a similar range of H_2O-CO_2 concentrations, i.e. 1·5 (±0·5) to 4 (±1) wt % H_2O, and ~60 to 2500 ppm CO_2 (Fig. 11; Table 7). These estimates are within the range of concentrations measured from MIs (0·2–4 wt % H_2O, 10–3000 ppm CO_2) by Preece *et al.* (2014).

In addition, we have estimated the melt H_2O concentrations using H_2O concentrations measured from Cpx and Opx, and the corresponding partitioning coefficients for H_2O ($D_{H_2O}^{Cpx-melt}$ and $D_{H_2O}^{Opx-melt}$ in Eqns. 5 and 6). We find that, except for the Cpx in a glomerocryst that reflects ~2·5 wt % H_2O in the melt, the rest of Cpx phenocrysts reflect low H_2O concentrations of ~0·1–0·7 wt % in the melt, and the Opx phenocrysts reflect ~0·5–1·0 wt % H_2O in the melt (Fig. 12a; Supplementary Data Table S5). The much lower melt H_2O contents calculated from Cpx phenocrysts than from their apatite inclusions (1·9–2·8 wt %; Fig. 12b) can be explained by diffusive H loss from the Cpx, which could occur during magma ascent (Wade *et al.* 2008). H diffuses more than 3 orders of magnitude faster in Cpx (Hercule and Ingrin, 1999) than OH diffusion in apatite at the relevant *T* of Merapi magmas (Li *et al.*, 2020). This highlights that apatite can better record H_2O concentrations in the melt compared to Cpx, especially when the samples have experienced slow cooling near the Earth's surface. Using melt H_2O–CO_2 concentrations calculated from apatite in Cpx and in groundmass, and the solubility model of Papale *et al.* (2006), we find H_2O–CO_2 saturation pressures between 20–410 MPa, mostly <100 MPa (Fig. 11b).

We found that the melt in equilibrium with apatite included in 2006 Amph had ~8 wt % H_2O, whereas melt those included in 2010 Amph contains about 3–8 wt % H_2O, and about 8000 to 27 000 ppm CO_2 (Table 7). Using the solubility model of Papale *et al.* (2006), we find H_2O–CO_2 saturation pressures of >800 MPa for these high volatile melts (Fig. 11a). We have used these results and models (#1 and #2 in Fig. 11a) to compute the open- and closed- system degassing paths, but none of the paths fits perfectly with our data. Here we cannot determine CO_2 concentration in the 2006 melt with ~8 wt % H_2O,

due to a lack of data for CO_2 concentration in the apatite inclusion in the 2006 Amph. Nevertheless, if the melt in equilibrium with the 2006 Amph contains the same or higher CO_2 than the melt in equilibrium with groundmass apatite, i.e. ≥2500 ppm, the H_2O–CO_2 saturation pressure of the deep melt of 2006 would be ≥530 MPa. Comparison of pressures calculated from the apatite in amphibole and the amphibole barometry are described in the following section.

Calculated melt S concentrations

Sulfur (S) concentrations in the melt were calculated using the distribution coefficient for S between apatite and melt, i.e. $D_S^{Ap-melt} = \frac{c_S^{Ap}}{c_S^{melt}}$, where c_S^{Ap} and c_S^{melt} represent the concentration of S in apatite and in the melt respectively. The $D_S^{Ap-melt}$ determined from previous experiments varies with varying apatite S concentration, melt composition, and oxygen fugacity (fO_2) (Peng *et al.*, 1997; Parat & Holtz, 2004, 2005; Konecke *et al.*, 2019). For magmas in the shallow reservoir or in the conduit of Merapi with log(fO_2) of ∼NNO + 1 (Erdmann *et al.*, 2016), the S^{6+}/total S in apatite (in Cpx/Pl/groundmass) should be ∼95% (Konecke *et al.*, 2019). For the deeper magmas (above 400 MPa) with log(fO_2) of FMQ + 2·2 to +0·6 (Gertisser, 2001), the S^{6+}/total S in apatite (in Amph) may vary from 95% down to ∼70% (Konecke *et al.*, 2019). Considering this and different compositions of the melt that equilibrated with the S-rich apatite in Amph and the S-poor apatite in Cpx/Pl/Groundmass, we have used different equations to calculate $D_S^{Ap-melt}$ as shown below.

For the apatite with >1500 ppm S included in Amph, we have used the equation for $D_S^{Ap-melt}$ (S as S^{6+}) determined for trachyandesite (Peng *et al.*, 1997): $lnD_S^{Ap-melt} = \frac{21130}{T} - 16.2$ (T in kelvins). Using T = 950–1000°C calculated from amphibole-liquid thermometry (Table 6), we find $D_S^{Ap-melt} \approx$ 2–3, comparable to that determined for basalt at 1000 °C and oxidized conditions (Konecke *et al.*, 2019). The calculated melt S contents are about 670 ppm for 2006, and 340–2000 ppm for 2010 (Table 7; relative error: 7–16%). The highest melt S estimate (∼2000 ppm) was yielded by the crystal in 2010 Amph that has the highest concentrations of S and CO_2, which reflects saturation pressure of >800 MPa. We have noticed that the melt H_2O/S concentrations calculated from the apatite in Amph show a wide range (Fig. 13). This could be related to the kinetic processes involved in the incorporation of S into these crystals, and/or the co-existence of multiple valences of S (e.g. S^{4+}, S^{2-}) in apatite below ∼FMQ + 1.2 (Konecke *et al.*, 2019). More accurate estimation of S concentrations in the deep and reduced magmas requires direct measurements of the abundances of S^{6+} and the S of other valences in the natural apatite.

For the S-poor apatite in Cpx, Pl, and the groundmass that contains S as mostly S^{6+} (see above), we used the equation for $D_S^{Ap-melt}$ (S as S^{6+}) of Parat and Holtz (2005): $ln\left(D_S^{Ap-melt}\right) = -0.0025 \times c_S^{melt}$ ($in\ ppm$) + 2.9178. To solve this equation, we combined it with $D_S^{Ap-melt} = \frac{c_S^{Ap}}{c_S^{melt}}$, and obtained:

$$c_S^{Ap}(in\ ppm) = \exp\left(-0.0025 \times c_S^{melt} + 2.9178\right) \times c_S^{melt} \quad (9)$$

To solve Eq. 9 using the values of c_S^{Ap} determined from SIMS, we have inputted a series of guessed c_S^{melt} values until the left- and right-hand sides of Eq. 9 become equivalent. We find that the melt of 2006 and 2010 in equilibrium with these crystals (i.e. apatite in Cpx, Pl, and Gm) have a similar concentration range of S between 10 and 130 ppm (using $D_S^{Ap-melt} \approx$ 12–18; Table 7). These values partly overlap with those determined from Cpx-hosted MIs from this study (∼18–530 ppm; Table 2) and in the literature (∼5–760 ppm; Costa *et al.*, 2013; Nadeau *et al.*, 2013; Preece *et al.*, 2014).

DISCUSSION

A critical appraisal of magma storage depths and the multi-reservoir plumbing system at Merapi

Constraining the architecture of volcanic plumbing systems helps to understand the eruption dynamics and interpret the monitoring data for eruption forecasting (Blundy & Cashman, 2008; Cashman & Sparks, 2013; Bachmann & Huber, 2016; Sparks & Cashman, 2017). Despite its importance, most petrological, geophysical and geodesic methods face the problem of imprecise determination of the magma storage locations. For example, seismic tomography is rarely capable of identifying small magma bodies (e.g. <5 km^3; Lowenstern *et al.*, 2017), nor distinguishing a bulk mush containing a small fraction of melt in its pore space from several isolated melt lenses in a rock matrix (Magee *et al.*, 2018; Maclennan, 2019). A simple spherical cavity 'Mogi source' is commonly used in deformation modelling (Segall, 2010), but this is over-simplified for a plumbing system made up of multiple reservoirs at various depths (Amoruso & Crescentini, 2009; Segall, 2019).

Mineral-based geobarometers (Putirka, 2008) usually give pressure–depth estimates with large errors (e.g. ± 5–10 km; Preece *et al.*, 2014): the mineral-only geobarometry is not very *P*-sensitive especially at pressures <5 GPa, due to the small changes in the partial molar volumes of solid solutions (Putirka, 2008). Moreover, mineral-melt geobarometry requires crystal-melt equilibrium, but this is difficult to test and is not achieved in many cases (e.g. for the Unzen 1991–1995 eruptions; Nakada & Motomura, 1999). More complexities arise when the investigated rocks consist of mixed crystal populations (such as from Merapi; e.g. Chadwick *et al.*, 2013; Costa *et al.*, 2013; Erdmann *et al.*, 2016), and/or the crystals are chemically-zoned as was commonly

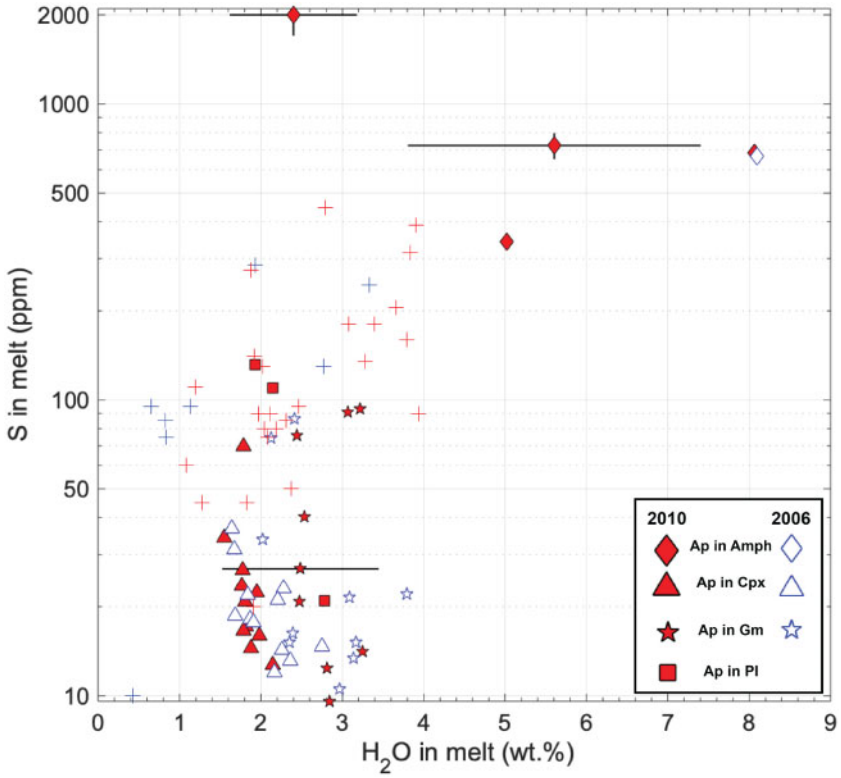

Fig. 13. Melt H_2O and S concentrations calculated using apatite (Table 7), compared with measurements for glass inclusions from the literature (2010, red cross; 2006, blue cross; Preece *et al.*, 2014). The *y*-axis is shown on a log scale for better visualisation. The melt in equilibrium with apatite in Cpx/Pl/Gm show similar ranges of H_2O and S contents with most of melt inclusions, but lower S concentrations than the deeper melt in equilibrium with apatite included in Amph (diamonds). Representative error bars show ± 1 s.d. of the calculated melt H_2O and S concentrations.

observed in the rocks from the intermediate-felsic magmatic systems (Pichavant *et al.*, 2007). Magmatic volatile-saturation pressures constrained from analyses of MIs need to be free of the re-equilibration and/or post-entrapment crystallization (Qin *et al.*, 1992; Danyushevsky *et al.* 2000; Gaetani & Watson 2000; Cottrell *et al.* 2002; Portnyagin *et al.*, 2008; Lloyd *et al.*, 2013). Given the limitations of the existing techniques, our knowledge of the plumbing systems of most volcanoes focuses on the shallow parts in the mid-upper crust, leaving the deeper structure in a rather blurred image (Cashman *et al.*, 2017; Edmonds *et al.*, 2019). Steele-MacInnis (2019) has proposed that the generally lower H_2O contents in MIs (mostly <6 wt %) than those determined for primitive melts from phase equilibrium experiments (up to >15 wt %) indicate that MIs are incapable of preserving water contents of the relatively wet and primitive melt, due to the difficulty of quenching.

The plumbing system of Merapi volcano has been studied using a variety of methods, and was proposed to contain multiple magma reservoirs at depths between 1 km and 45 km (Beauducel & Cornet, 1999; Ratdomopurbo & Poupinet, 2000; Gertisser, 2001; Chadwick *et al.*, 2007; Chadwick *et al.*, 2013; Costa *et al.*, 2013; Preece *et al.*, 2014; Erdmann *et al.*, 2016; Widiyantoro *et al.*, 2018), with low-velocity anomaly almost through the whole crust observed at Merapi and other volcanoes in central Java (Wagner *et al.*, 2007; Koulakov *et al.*, 2009). In the following paragraphs we review the literature data and compare them with our results calculated from apatite (Fig. 14). For easy comparison of depths proposed by different studies, we have converted pressure estimates from the literature into depths (assuming 0 at the summit crater), using the average crustal densities from Widiyantoro *et al.* (2018), i.e. 2242 kg/m^3 at ≤ 10 km depth (Tiede *et al.*, 2005) and 2900 kg/m^3 at >10 km depth (Rudnick & Fountain, 1995).

Volcano monitoring studies (e.g. seismic and deformation data) have suggested the presence of shallow magma reservoirs at 1–9 km depth: (from shallow to deep) ~0·8–1·8 km from gravity anomalies (Saepuloh *et al.*, 2010), 1·5–2·5 km from seismic and deformation studies (Ratdomopurbo & Poupinet, 2000; Budi-Santoso *et al.*, 2013; Saepuloh *et al.*, 2013; Aisyah *et al.*, 2018), and ~8·5 km from the GPS and tiltmeter data during the quiescence (Beauducel & Cornet, 1999) (Fig. 14). These depths are covered by the range of magmatic volatile-saturation depths (1–12 km) from petrological studies on melt inclusions (Nadeau *et al.*, 2013; Preece *et al.*, 2014), and overlap with the clinopyroxene/plagioclase crystallization depths (4·5–12 km) found from phase equilibrium experiments (Erdmann *et al.*, 2016). The shallowest magma storage zone within the volcano

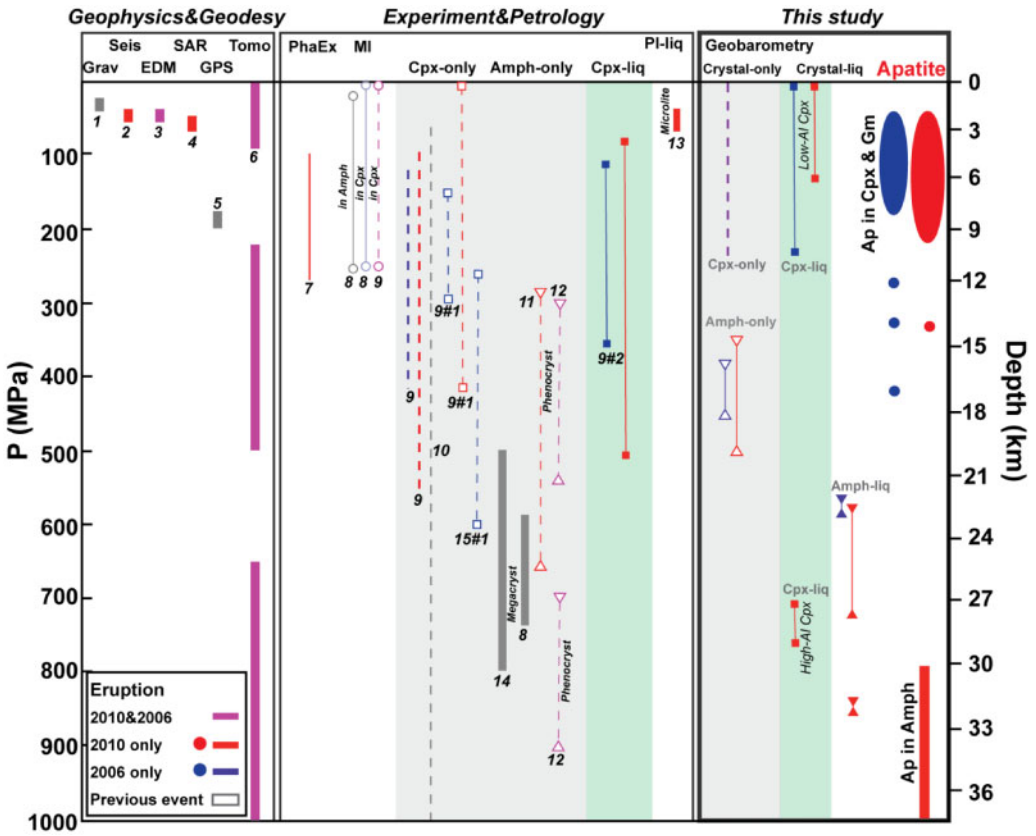

Fig. 14. Magma storage pressure-depths below Merapi volcano, calculated from apatite, amphibole and clinopyroxene from this study, and suggested by previous studies based on a variety of methods/techniques (symbols in different colors indicate different eruptions as shown in legend; symbols in different shapes indicate different methods used for deriving depths; see below). Depths calculated from apatite in Cpx and Gm are marked in solid circles/ellipses, and larger symbol sizes indicate more crystals at given depths (large ellipses: $N = 7$–8; small circle: $N = 1$). Abbreviations for different methods are: Grav, Gravity anomalies; Seism, seismicity; EDM, Electronic Distance Measurements; SAR, Synthetic Aperture Radar; Tomo, Seiscmic tomography; PhaExp, Phase equilibrium experiments; MI, melt inclusions (hosted by clinopyroxene, or amphibole megacrysts); Cpx-liq, clinopyroxene-liquid barometer of Putirka (2008) calculated using Eq. 32c (see symbol used for 9#2 in figure); Cpx-only, clinopyroxene-only barometer of Nimis (1999) (see symbol used for 10 in figure), and that of Putirka (2008) using Eq. 32b where melt H_2O is considered (see symbol used for 9#1 in figure); Amph-only, amphibole-only barometer of Ridolfi *et al.* (2010) on megacrysts, and of Ridolfi & Renzulli (2012) on phenocrysts; Amph-liq, amphibole-liquid barometer of Putirka (2016); Pl-liq, plagioclase-liquid hygrometer of Waters and Lange (2015) on plagioclase microlites. Data sources: [1]Saepuloh *et al.* (2010); [2]Budi-santoso *et al.* (2013); [3]Aisyah *et al.* (2018); [4]Saepuloh *et al.* (2013); [5]Beauducel and Cornet (1999); [6]Widiyantoro *et al.* (2018); [7]Erdmann *et al.* (2016); [8]Nadeau *et al.* (2013); [9]Preece *et al.* (2014); [10]Chadwick *et al.* (2013); [11]Erdmann *et al.* (2014); [12]Costa *et al.* (2013); [13]Preece *et al.* (2016); [14]Peters *et al.* (2017); [15]Deegan *et al.* (2016).

edifice detected by geoelectric sounding and seismic investigations was also interpreted as layers of saline fluids, rather than melts (e.g. Wegler and Lühr, 2001; Müller & Haak, 2004; Luehr *et al.*, 2013; Widiyantoro *et al.*, 2018).

Geobarometric calculations using clinopyroxene and amphibole suggest a wider range of depths, from the upper to the lower crust, including 1–15 km (Nadeau *et al.*, 2013; Preece *et al.*, 2014), ~11–23 km (Deegan *et al.*, 2016), ~20–30 km (Costa *et al.*, 2013; Nadeau *et al.*, 2013; Peters *et al.*, 2017), and up to ~45 km (Chadwick *et al.*, 2013) (Fig. 14). The clinopyroxene-only geobarometry of Nimis (1999) applied to samples from the 1994 and 1998 eruptions gave the widest range of depths (2–45 km; Chadwick *et al.*, 2013). The clinopyroxene-only geobarometry of Putirka (2008; Eq. 32b) applied to the 2006 samples indicated depths of 11–23 km (concentrating at ~18 km; Deegan *et al.*, 2016), and also shallower depths of ~7–13 km (Preece *et al.*, 2014). The clinopyroxene-liquid geobarometry of Putirka (2008; Eq. 32c) applied to samples from the 2006 and 2010 eruptions indicated depths of ~4–16 km (with one value up to ~20 km from Cpx in 2010 white pumice; Preece *et al.*, 2014). Calculations using the amphibole-only barometers (Ridolfi & Renzulli, 2010; Ridolfi *et al.*, 2012) and amphibole phenocrysts of 2006 and 2010 indicated depths of ~13 (±2) km and ~30 (±2) km (Erdmann *et al.*, 2014; Costa *et al.*, 2013), whereas amphibole megacrysts from historical eruptions give depths of about 20–30 km (Nadeau *et al.*, 2013; Peters *et al.*, 2017). The geobarometry calculations mentioned above (especially those based on mineral composition only) have large uncertainties which could translate to errors in depths of 5–10 km (cf. Preece *et al.*, 2014).

To be able to reliably use the crystal-liquid geobarometry it is important, and yet difficult, to know the

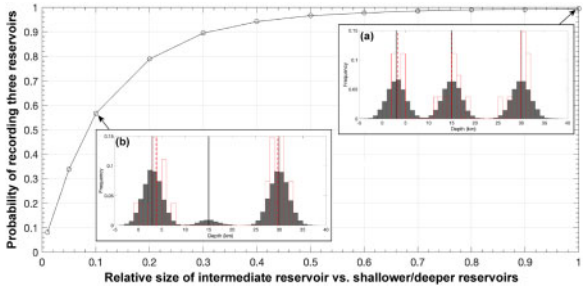

Fig. 15. Results of simulations on the probability of recording the depths of three expected major magma reservoirs at 3 (±2), 15 (±2) and 30 (±2) km (mean values: black solid lines), by the number of apatite crystals (***N***= 27) used for estimating depths in this study. If the three reservoirs are approximately the same size, the probability of sampling all the three reservoirs by 27 crystals is close to 1 (inset a); if the size of the intermediate reservoir is 10 x smaller than the other two, the probability of sampling it would drop to ∼0·5 (see example of missing the intermediate reservoir in inset b). Dark grey bars in insets show 'original' distributions of depths (assumed as normal distributions). Empty bars with red edges show depths recorded by sampled crystals (mean values: red dashed lines). See interpretations in the main text and methods in Supplementary Data Electronic Appendix.

composition of the melt that equilibrated with the erupted crystals. This is especially difficult when studying open-system volcanoes like Merapi, where the erupted rocks consist of multiple crystal populations originating from different magma sources (e.g. Gertisser & Keller, 2003; Chadwick *et al.*, 2013; Costa *et al.*, 2013; Preece *et al.*, 2014; Erdmann *et al.*, 2016). Thus, significant uncertainty remains on whether the geobarometric results above record the real pressure-depths for magma crystallization and storage. More specifically, it is unclear whether such wide range of depths reflect widespread distribution of melts below Merapi, or are an artefact of limited and partial melt-crystal equilibrium of the compositions used. Seismic tomography images (Widiyantoro *et al.*, 2018) suggest two magma storage zones at ∼10–20 km and >25 km respectively (Fig. 14). However, given the significant uncertainties in depths (±5 km, according to the size of grid nodes used in the inversion model of Widiyantoro *et al.*, 2018), it is unclear whether the magma storage depths of 10–20 km are real, and whether this magma storage zone is isolated or interconnected with other magma reservoir(s) at shallower/deeper locations.

Our calculations using apatite volatile compositions indicate depths of 2–7 (±1–2) km (with an outlier at ∼14 km) where apatite in Cpx grew (***N***= 15), mostly 2–9 km (up to 17 km; ± 2–3 km) where apatite microphenocrysts/microlites grew (***N***= *10*), and ≥30 km where apatite inclusions in 2010 Amph grew (***N***= 2; Fig. 14). Using Cpx-liquid geobarometry of Putirka (2008; Eq. 32 c), we find depths of ≤10 km from the low-Al Cpx (with apatite included) that cover the range of depths calculated from apatite in Cpx, and larger depths (∼24–30 km, ±5 km) from the 2010 high-Al Cpx (with no apatite inclusion), overlapping with those calculated using amphibole-liquid barometry of Putirka (2016; Eq. 7a), i.e. ∼22–32 km (±3–5 km). As comparison, pressure-depths calculated using the amphibole-only barometry of Ridolfi & Renzulli (2012) show generally lower values (Table 6; Fig. 14), and were not taken into consideration due to larger uncertainties. The shallow magma storage depths at 1–10 km are recorded by the majority of apatite crystals in Cpx and in groundmass, and agree with depths (<5 km) obtained by multiple geophysical, geodetic, and seismic tomography studies (Saepuloh *et al.*, 2010; Ratdomopurbo & Poupinet, 2000; Budi-Santoso *et al.*, 2013; Saepuloh *et al.*, 2013; Aisyah *et al.*, 2018), overlap with those revealed by MIs (1–12 km; Preece *et al.*, 2014), phase equilibrium experiments (4·5–12 km; Erdmann et al., 2016), as well as GPS and tilt observations (∼8·5 km; Beauducel & Cornet, 1999). The majority of depths calculated for the deep reservoir from this study, i.e. from ∼25 (±5) to ≥30 km, were also proposed by previous seismic tomography studies (Widiyantoro *et al.*, 2018), and overlap with geobarometric calculations on amphibole megacrysts from older eruption deposits (Nadeau *et al.*, 2013; Peters *et al.*, 2017).

Only three apatite crystals in the groundmass (out of 27 crystals that we analysed) indicate discrete magma depths between 13–17 km, reflecting that the reservoir in the mid-crust (as suggested by some studies mentioned above) was not significantly involved in the 2006 and 2010 eruptions. A question that may arise here is whether the apatite sample size we have used (***N***= 27) provides a biased view of magma reservoir depths, i.e. whether the limited number of crystals may have missed the record of any major reservoir. To investigate this, we performed simple numerical simulations on the probability of sampling the various apatite populations from three potential magma storage zones at about 3 (±2), 15 (±2) and 30 (±2) km depths (see examples in Fig. 15 and Supplementary Data Fig. S6). By randomly sampling 27 crystals out of a much larger crystal population for many times, we have obtained the probability that the sampled crystals reflect the mean depths of the three reservoirs (see Supplementary Data Fig. S7). We find that if the intermediate reservoir is of similar size to the other two reservoirs, there is a probability of ∼0·995 that the sampled 27 crystals would show all the three major distributions at the expected depths (Fig. 15a). But if the intermediate reservoir is much smaller than the other two (e.g. ∼10 times), the probability significantly decreases (e.g. to ∼0·5; Fig. 15b). Results from these simulations indicate that the number of crystals that we have studied are, in principle, statistically representative of the major magma storage zones (at two distinct depths) related to the 2006 and 2010 eruptions at Merapi. Given that apatite can crystallise from silicate melts over a wide range of *P–T* conditions through the crust (e.g. Webster & Piccoli, 2015; Li & Costa, 2020), the fact that no intermediate reservoir was recorded by our samples is unlikely due to a lack of apatite crystallization in the mid crust. Instead, this can be explained if the intermediate reservoir is much smaller and/or it contributed much smaller volumes of magmas to the 2006 and 2010 eruptions, compared to the shallower and deeper reservoirs.

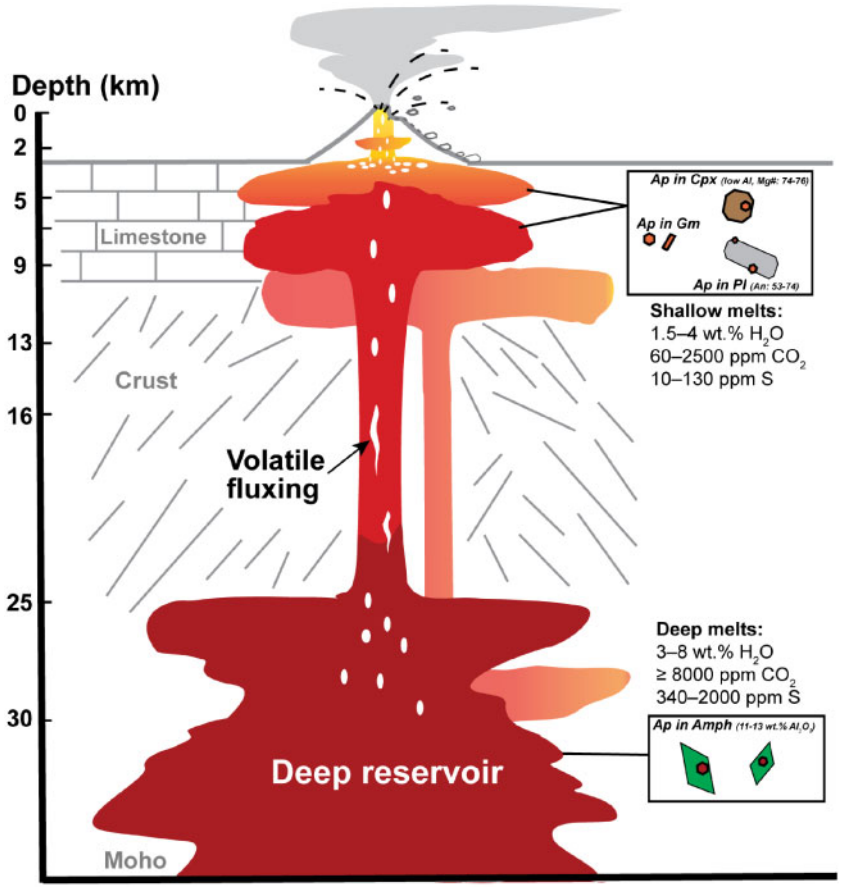

Fig. 16. Sketch for the plumbing system of Merapi, showing two major magma reservoirs at depths ≤10 km and ≥25–30 km respectively. Compared to the dome-forming eruption in 2006, the more explosive eruption in 2010 was likely caused by larger volumes of magma-volatile fluxes originating from depth, which increased the buoyancy of the shallower magmas, and thus led to faster magma ascent and larger explosivity in 2010.

In summary, we suggest that there are two major magma reservoirs that fed the 2006 and 2010 eruptions: one at ≤10 km below the summit crater where the majority of magma degassing/crystallization occurred, and the other at depth ≥25–30 km (Fig. 16). The majority of shallow magmas (<5 km deep) found in this study for Merapi are at similar depths to those proposed for other volcanoes in central Java (e.g. Slamet and Lawu, detected by InSAR; Chaussard & Amelung, 2012) and at the Sunda arc (e.g. Geiger *et al.*, 2018). It is unclear whether there are significant amounts of magmas between the two major reservoirs at Merapi, given the uncertainties in calculations on apatite from this study, and on the mineral-only geobarometry from the literature (see above). Additional constraints on the depths of magma storage may be obtained based on the depth of brittle–ductile transition and the magma buoyancy in relation to the volumes of exsolved volatiles (e.g. Huber *et al.*, 2019), but this requires a good understanding of how the high thermal flux affects the crustal densities at an active volcano such as Merapi. The dual reservoir model proposed here is different from the architecture of plumbing systems consisting of multiple continuous magma reservoirs through the whole crust (e.g. Cashman *et al.*, 2017). The case study of Merapi volcano using apatite indicates that the architecture of volcano plumbing systems may be unravelled by chemical analyses of volatiles in a large number of apatite crystals that occur at different textural positions in the erupted products.

Links between magmatic volatiles and pre-eruptive gas emission

The composition of pre-eruptive volcanic gas can be combined with modeling of magmatic volatile saturation (e.g. Moretti *et al.*, 2003; Scaillet & Pichavant, 2005) and used as eruption precursor (e.g. for Etna and Stromboli volcanoes; Aiuppa *et al.*, 2007, 2009). To properly interpret the gas data using volatile saturation models, it is necessary to know the abundance and composition of volatiles in melts at different depths of the system. With the 'initial' melt volatile budgets as estimated from apatite inclusions in amphibole, it is possible to construct magma ascent and degassing models that translate to the depth (e.g. Aiuppa *et al.*, 2007). These models are quite complex and need to

involve the kinetics of the processes and how volatile composition may evolved during ascent (Burgisser & Scaillet, 2007), which are beyond the scope of this paper. Below we rationalize the changes in composition of the fumaroles with time with the different composition of the volatiles in the melt at different depths.

The composition of gas emitted from Merapi has been traditionally monitored by sampling high-temperature fumaroles from the summit Woro-field (Humaida *et al.*, 2007; Surono *et al.*, 2012). A common observation is that CO_2/SO_2 in the fumarolic gas increases towards the eruption, e.g. from $CO_2/SO_2 \approx 9$ during quiescence and passive degassing, to up to ~ 37 before the 2006 eruption, and to the maximum of $\sim$118 on October 20th, 2010 (one week before the first eruption stage) (Humaida *et al.*, 2007; Surono *et al.*, 2012). In addition, CO_2/H_2O in the fumarolic gas also increases towards the eruption, e.g. from $\sim$0·05 during quiescence and passive degassing, to $\sim$0·5 about one month before the 2006 eruption (in March), and to the maximum of $\sim$2·7 in October 2010. This means that from the quiescence to just before the 2010 eruption, CO_2/SO_2 and CO_2/H_2O values of the fumarolic gas increase by factors of about 13 and 54, respectively. Such significant changes in gas composition can be rationalized as due to changes in the depths of magma degassing (e.g. Aiuppa *et al.*, 2007, 2009; Scaillet & Pichavant, 2005), and qualitatively agree with the differences in C/S and CO_2/H_2O between shallow MIs and the deepest melt reflected by apatite in Amph from this study.

Another explanation for the CO_2-rich gas released just before eruption is the decarbonation of limestones, which commonly exist at the upper crust in Java (e.g. Allard, 1983; Chadwick *et al.*, 2007; Deegan *et al.*, 2010; Troll *et al.*, 2012, 2013; Blythe *et al.*, 2015; Carr *et al.*, 2018; Whitley *et al.*, 2019). The CO_2 released from limestones at such shallow level is hardly likely to be soluble in the melt and thus tends to exist as a vapor phase rather than dissolving in the melt (e.g. Troll *et al.*, 2013). As a result, the CO_2 contribution from limestone assimilation is difficult to be recorded by melt inclusions or apatite, and thus not recorded in our data. Nonetheless, the depleted $\delta^{13}C$ signals of fumarolic CO_2 emitted from Merapi (Allard *et al.*, 2011) suggest a major magmatic input from large depths, which is supported by the deep magma reservoir ($\geq$25–30 km) found in this study.

Given the similar volatile concentrations in the shallow melt inferred by the products of the two eruptions, there have to be more complex processes (e.g. related to the magma ascent and degassing) to cause the difference in the explosivities in 2006 and 2010 (e.g. Costa *et al.*, 2013; Preece *et al.*, 2014, 2016; Handley *et al.*, 2018; Carr *et al.*, 2020). The high CO_2/SO_2 and CO_2/H_2O values of the fumarolic gas emitted about one week before the first explosion in 2010 suggests larger amounts of deep volatiles, which could be in accord with larger amounts of magma replenishment from depths that released volatiles that fluxed the shallow magma column. Surono *et al.* (2012) has suggested the presence of significant amounts of exsolved volatiles before the eruption in 2010. These exsolved volatiles were able to produce larger magma buoyancy and faster magma ascent in 2010, which eventually caused the explosive eruption (Fig. 16). Evidence for the faster magma ascent in 2010 than 2006 has been found from volcano monitoring, petrography observations and diffusion modelling of apatite as summarized below.

Faster magma ascent in 2010 than 2006 revealed by Cl zoning in apatite

Magma ascent rate has been recognized as a key parameter for controlling eruptive styles (e.g. Cashman & Sparks, 2013; Cassidy *et al.*, 2018), however few magma ascent rates were directly determined (e.g. Humphreys *et al.*, 2008; Myers et al 2016). In the case of Merapi, magma ascent in 2010 was higher than in 2006, based on the following observations: (1) magma extrusion rates of the eruption in 2010 were much larger ($\approx$25–35 m^3/s; Pallister *et al.*, 2013) than those in 2006 ($\leq$ 1–4 m^3/s; Surono *et al.*, 2012; Ratdomopurbo *et al.*, 2013); (2) the amphibole of 2010 rarely has breakdown reaction rims, whereas many amphibole crystals of 2006 have (Costa *et al.*, 2013); (3) the higher number density of microlites in 2010 (stage-4) rocks than that in 2006 deposits reflects nucleation-dominant crystallization of microlites in 2010 due to more rapid magma ascent and degassing (Preece *et al.*, 2013, 2016); and (4) different distances of diffusion-induced Cl zoning in the 2006 and 2010 apatites, due to different durations of magma ascent before the two eruptions (Li *et al.*, 2020; see below).

Apatite microlites from rocks emitted in 2006 are commonly zoned, increasing Cl towards their rims for distances of 3–7 μm (Fig 3), whereas the 2010 apatite shows no obvious zoning of F/Cl/OH (Fig. 4). Moreover, the Cl zoning is anisotropic, and only occurs along the c-axis, as is expected given the large anisotropy of the Cl diffusion coefficient in apatite (e.g. Li *et al.*, 2020). The observed Cl zoning was unlikely related to crystal growth, as there is no zoning of trace elements (e.g. REE) according to cathodoluminescence images (Li, 2019). Cl diffusion in groundmass apatite can be driven by increasing Cl/H_2O concentrations in the melt due to decompression-induced H_2O loss, and associated microlite crystallization during magma ascent, and increasing Cl melt concentration. Thus, we believe that the zoning developed during magma ascent from the last stage of pre-eruptive storage and its ascent towards the surface. Li *et al.* (2020) experimentally determined the diffusivities of F–Cl–OH in apatite and used a three-component diffusion model to calculate timescales for the same samples from this study. They found that the 2006 and 2010 apatite reflect magma ascent times of about two weeks, and less than 3 days respectively, which are comparable to the durations between the start of volcanic unrest and the eruption proposed in previous studies (Ratdomopurbo *et al.*, 2013; Aisyah *et al.*, 2018). Given that the pre-eruptive magmas of the two eruptions were likely stored at similar depths, magma ascent rates of the 2010 and 2006

eruptions are on average >0·01–0·04 m/s and ~0·002–0·005 m/s respectively, consistent with an order of magnitude greater magma extrusion rates in 2010 than 2006 (Surono *et al.*, 2012; Pallister *et al.*, 2013; Ratdomopurbo *et al.*, 2013). The minimum ascent rate of 0·01–0·04 m/s estimated for the VEI-4 explosive eruption in 2010 using apatite agrees with the ascent rates of ≥0·01–0·1 m/s proposed for explosive eruptions at a variety of arc volcanoes (Cassidy *et al.*, 2018).

CONCLUSIONS

We have found that the apatite crystals from the Merapi 2006 and 2010 eruptions with contrasting eruptive dynamics reflect two main magma storage zones with similar melt volatile contents. The shallow magma storage zone was at ≤10 km below the crater, containing melts with about 1·5–4 wt % H_2O, 60–2500 ppm CO_2 and 10–130 ppm S. The deeper magma storage zone was at ≥25–30 km depth, containing melts with ~3–8 wt % H_2O, ≥8000 ppm CO_2 and ~340–2000 ppm S. The melt CO_2 concentrations calculated from apatite likely represent the maximum, given the extrapolation of apatite-melt CO_2 partitioning data (determined from experiments) to the melt and temperature conditions applicable to Merapi. Combination of our results with the literature data suggests that the 2006 and 2010 eruptions at Merapi were fed by magmas from two major reservoirs that are connected by magma-volatile fluxes. The deep volatile-rich melts revealed by the apatite in amphibole can explain the changes in the compositions of fumarolic gases before the two eruptions. Our results imply that the more explosive 2010 eruption was likely driven by a larger amount of deep magmas that released volatiles to the upper parts of the system and led to a higher magma buoyancy, faster magma ascent and thus larger explosivity. This is consistent with the slower magma ascent of the 2006 eruption (than 2010) recorded by the crystallization-degassing-related Cl zoning in groundmass apatite. Applications of apatite volatile chemistry to constraints on volatile contents, storage depths, and ascent rates of pre-eruptive magmas may contribute to a better understanding of the effusive-explosive transition at volcanoes, and can be integrated with volatile solubility models and monitoring data to give more accurate eruption forecasts.

ACKNOWLEDGMENTS

This work is part of the Ph.D. thesis of W. Li, who would like to thank professor Y. Zhang for generously providing the natural apatite standards, J. Herrin for assistance with electron microanalysis, and C. Widiwijayanti and L. Cheng for discussions on the eruption dynamics at Merapi volcano. W. Li. and F. Costa thank J. Pallister for collecting and sharing the rock samples, and H. Humaida and other staff from BPPTKG (Indonesia) for discussions on the eruption history of Merapi. We are grateful to R. Gertisser, K. Preece, S. Erdmann and an anonymous reviewer for their constructive comments on this manuscript, and thank V. Troll for editorial support.

FUNDING

This work was supported by the 'Magma plumbing system' research project at the Earth Observatory of Singapore via its funding from the National Research Foundation Singapore Investigatorship Award (NRF-NRFI2017-06). This work is Earth Observatory of Singapore contribution number 328.

SUPPLEMENTARY DATA

Supplementary data are available at *Journal of Petrology* online.

REFERENCES

Aisyah, N., Iguchi, M., Subandriyo, B., A., Hotta, K. & Sumarti, S. (2018). Combination of a pressure source and block movement for ground deformation analysis at Merapi volcano prior to the eruptions in 2006 and 2010. *Journal of Volcanology and Geothermal Research* **357**, 239–253.

Aiuppa, A., Federico, C., Giudice, G., Giuffrida, G., Guida, R., Gurrieri, S., Liuzzo, M., Moretti, R. & Papale, P. (2009). The 2007 eruption of Stromboli volcano: Insights from real-time measurement of the volcanic gas plume CO_2/SO_2 ratio. *Journal of Volcanology and Geothermal Research* **182**, 221–230.

Aiuppa, A., Moretti, R., Federico, C., Giudice, G., Gurrieri, S., Liuzzo, M., Papale, P., Shinohara, H. & Valenza, M. (2007). Forecasting Etna eruptions by real-time observation of volcanic gas composition. *Geology* **35**, 1115–1118.

Allard, P. (1983). The origin of hydrogen, carbon, sulphur, nitrogen and rare gases in volcanic exhalations; evidence from isotope geochemistry. In: Tazieff, H. & Sabroux, J. (eds) *Forecasting Volcanic Events*. New York: Elsevier, pp. 337–386.

Allard, P. (2010). A CO_2-rich gas trigger of explosive paroxysms at Stromboli basaltic volcano. *Journal of Volcanology and Geothermal Research* **189**, 363–374.

Allard, P., Métrich, N. & Sabroux, J. (2011). Volatile and magma supply to standard eruptive activity at Merapi volcano, Indonesia. *EGU General Assembly Abstracts* **13**, 13522.

Amoruso, A. & Crescentini, L. (2009). Shape and volume change of pressurized ellipsoidal cavities from deformation and seismic data. *Journal of Geophysical Research* **114**, B02210.

Anderson, J. L. & Smith, D. R. (1995). The effects of temperature and fO_2 on the Al-in-hornblende barometer. *American Mineralogist* **80**, 549–559.

Armstrong, J. T. (1988). Quantitative analysis of silicate and oxide minerals: comparison of Monte-Carlo, ZAF, and Phi-Rho-Z procedures. In: Newbury DE (ed.) *Proc. Microbeam Analysis Society*. San Francisco: San Francisco Press, p. 239.

Bachmann, O. & Huber, C. (2016). Silicic magma reservoirs in the Earth's crust. *American Mineralogist* **101**, 2377–2404.

Bacon, C. R. (1989). Crystallization of accessory phases in magmas by local saturation adjacent to phenocrysts. *Geochimica et Cosmochimica Acta* **53**, 1055–1066.

Beauducel, F. & Cornet, F. (1999). Collection and three-dimensional modelling of GPS and tilt data at Merapi volcano. *Journal of Geophysical Research: Solid Earth* **104**, 725–736.

Blake, S. (1984). Volatile oversaturation during the evolution of silicic magma chambers as an eruption trigger. *Journal of Geophysical Research* **89**, 8237–8244.

Blundy, J. & Cashman, K. (2008). Petrologic reconstruction of magmatic system variables and processes. *Reviews in Mineralogy and Geochemistry* **69**, 179–239.

Blundy, J. & Holland, T. J. (1990). Calcic amphibole equilibria and a new amphibole-plagioclase geothermometer. *Contributions to Mineralogy and Petrology* **104**, 208–224.

Blythe, L. S., Deegan, F. M., Freda, C., Jolis, E. M., Masotta, M., Misiti, V., Taddeucci, J. & Troll, V. R. (2015). CO_2 bubble generation and migration during magma–carbonate interaction. *Contributions to Mineralogy and Petrology* **169**, 42.

Borisova, A. Y., Martel, C., Gouy, S., Pratomo, I., Sumarti, S., Toutain, J. P., Bindeman, I. N., de Parseval, P., Metaxian, J. P. & Surono (2013). Highly explosive 2010 Merapi eruption: evidence for shallow-level crustal assimilation and hybrid fluid. *Journal of Volcanology and Geothermal Research* **261**, 193–208.

Boudreau, A. E. (1995). Fluid evolution in layered intrusions: evidence from the chemistry of the halogen-bearing minerals. In: *Magmas, Fluids and Ore Deposits*, pp. 25–46.

Boyce, J. W. & Hervig, R. L. (2008). Magmatic degassing histories from apatite volatile stratigraphy. *Geology* **36**, 63–66.

Boyce, J. W. & Hervig, R. L. (2009). Apatite as a monitor of late-stage magmatic processes at Volcán Irazú, Costa Rica. *Contributions to Mineralogy and Petrology* **157**, 135–145.

Budi-Santoso, A., Lesage, P., Dwiyono, S., Sumarti, S., Subandriyo, J., Surono, Jousset, P. & Metaxian, J.-P. (2013). Analysis of the seismic activity associated with the 2010 eruption of Merapi volcano, Java. *Journal of Volcanology and Geothermal Research* **261**, 153–170.

Burgisser, A. & Scaillet, B. (2007). Redox evolution of a degassing magma rising to the surface. *Nature* **445**, 194–197.

Byrdina, S., Friedel, S., Vandemeulebrouck, J., Budi-Santoso, A., Suryanto, W., Rizal, M. H. & Winata, E. (2017). Geophysical image of the hydrothermal system of Merapi volcano. *Journal of Volcanology and Geothermal Research* **329**, 30–40.

Carr, B. B., Clarke, A. B. & de' Michieli Vitturi, M. (2018). Earthquake induced variations in extrusion rate: a numerical modeling approach to the 2006 eruption of Merapi Volcano (Indonesia). *Earth and Planetary Science Letters* **482**, 377–387.

Carr, B. B., Clarke, A. B. & de' Michieli Vitturi, M. (2020). Volcanic conduit controls on effusive-explosive transitions and the 2010 eruption of Merapi Volcano (Indonesia). *Journal of Volcanology and Geothermal Research* **392**, 106767.

Cashman, K. V. & Sparks, R. S. J. (2013). How volcanoes work: a 25 year perspective. *Geological Society of America Bulletin* **125**, 664–690.

Cashman, K. V., Sparks, R. S. J. & Blundy, J. D. (2017). Vertically extensive and unstable magmatic systems: a unified view of igneous processes. *Science* **355**, eaag3055.

Cassidy, M., Manga, M., Cashman, K. & Bachmann, O. (2018). Controls on explosive-effusive volcanic eruption styles. *Nature Communications* **9**, 2839.

Chadwick, J. P., Troll, V. R., Ginibre, C., Morgan, D., Gertisser, R., Waight, T. E. & Davidson, J. P. (2007). Carbonate assimilation at Merapi Volcano, Java, Indonesia: insights from crystal isotope stratigraphy. *Journal of Petrology* **48**, 1793–1812.

Chadwick, J. P., Troll, V. R., Waight, T. E., van der Zwan, F. M. & Schwarzkopf, L. M. (2013). Petrology and geochemistry of igneous inclusions in recent Merapi deposits: a window into the sub-volcanic plumbing system. *Contributions to Mineralogy and Petrology* **165**, 259–282.

Chaussard, E. & Amelung, F. (2012). Precursory inflation of shallow magma reservoirs at west Sunda volcanoes detected by InSAR. *Geophysical Research Letters* **39**, n/a–n/a.

Cheng, L. & Costa, F. (2019). Statistical analysis of crystal populations and links to volcano deformation for more robust estimates of magma replenishment volumes. *Geology* **47**, 1171–1175.

Chevychelov, V. Y., Bocharnikov, R. E. & Holtz, F. (2008). Experimental study of chlorine and fluorine partitioning between fluid and subalkaline basaltic melt. *Doklady Earth Sciences* **422**, 1089–1092.

Clark, K., Zhang, Y. & Naab, F. U. (2016). Quantification of CO_2 concentration in apatite. *American Mineralogist* **101**, 2443–2451.

Costa, F., Andreastuti, S., Bouvet de Maisonneuve, C. & Pallister, J. S. (2013). Petrological insights into the storage conditions, and magmatic processes that yielded the centennial 2010 Merapi explosive eruption. *Journal of Volcanology and Geothermal Research* **261**, 209–235.

Costa, F., Scaillet, B. & Pichavant, M. (2004). Petrological and experimental constraints on the pre-eruption compositions of Holocene dacite from Volcan San Pedro (36° S, Chilean Andes) and importance of sulphur in silicic subduction-related magmas. *Journal of Petrology* **45**, 855–881.

Cottrell, E., Spiegelman, M. & Langmuir, C. H. (2002). Consequences of diffusive reequilibration for the interpretation of melt inclusions. *Geochemistry, Geophysics, Geosystems* **3**, 1–26.

Dalou, C., Koga, K., Le Voyer, M. & Shimizu, N. (2014). Contrasting partition behavior of F and Cl during hydrous mantle melting: implications for Cl/F signature in arc magmas. *Progress in Earth and Planetary Science* **1**, 26.

Dalou, C., Koga, K., Shimizu, N., Boulon, J. & Devidal, J. L. (2012). Experimental determination of F and Cl partitioning between lherzolite and basaltic melt. *Contributions to Mineralogy and Petrology* **163**, 591–609.

Danyushevsky, L. V., Della-Pasqua, F. N. & Sokolov, S. (2000). Re-equilibration of melt inclusions trapped by magnesian olivine phenocrysts from subduction-related magmas: petrological implications. *Contributions to Mineralogy and Petrology* **138**, 68–83.

Deegan, F. M., Troll, V. R., Freda, C., Misiti, V., Chadwick, J. P., McLeod, C. L. & Davidson, J. P. (2010). Magma–carbonate interaction processes and associated CO_2 release at Merapi Volcano, Indonesia: insights from experimental petrology. *Journal of Petrology* **51**, 1027–1051.

Deegan, F. M., Whitehouse, M. J., Troll, V. R., Budd, D. A., Harris, C., Geiger, H. & Halenius, U. (2016). Pyroxene standards for SIMS oxygen isotope analysis and their application to Merapi volcano, Sunda arc, Indonesia. *Chemical Geology* **447**, 1–10.

Degruyter, W., Huber, C., Bachmann, O., Cooper, K. M. & Kent, A. J. R. (2017). Influence of exsolved volatiles on reheating silicic magmas by recharge and consequences for eruptive style at Volcán Quizapu (Chile). *Geochemistry, Geophysics, Geosystems* **18**, 4123–4135.

Donovan, J. J. & Tingle, T. N. (1996). An improved mean atomic number background correction for quantitative microanalysis. *Journal of the Microscopy Society of America* **2**, 1–7.

Edmonds, M., Cashman, K. V., Holness, M. & Jackson, M. (2019). Architecture and dynamics of magma reservoir. *Philosophical*

Transactions of the Royal Society A: Mathematical, Physical and Engineering Sciences **377**, 20180298.

Erdmann, S., Martel, C., Pichavant, M. & Kushnir, A. (2014). Amphibole as an archivist of magmatic crystallization conditions: problems, potential, and implications for inferring magma storage prior to the paroxysmal 2010 eruption of Mount Merapi. *Contributions to Mineralogy and Petrology* **167**, 1016.

Erdmann, S., MartelC., Pichavant M., Bourdier, J. L., Champallier, R., Komorowski J. C. & Cholik, N. (2016) Constraints from phase equilibrium experiments on pre-eruptive storage conditions in mixed magma systems: a case study on crystal-rich basaltic andesites from Mount Merapi, Indonesia. *Journal of Petrology* **57**, 535–560.

Gaetani, G. A. & Watson, E. B. (2000). Open system behavior of olivine-hosted melt inclusions. *Earth and Planetary Science Letters* **183**, 27–41.

Geiger, H., Troll, V. R., Jolis, E. M., Deegan, F. M., Harris, C., Hilton, D. R. & Freda, C. (2018). Multi-level magma plumbing at Agung and Batur volcanoes increases risk of hazardous eruptions. *Scientific Reports* **8**, 10547.

Gertisser, R. (2001). Gunung Merapi (Java, Indonesien): Eruptionsgeschichte und magmatische Evolution eines Hochrisiko-Vulkans. Ph.D. thesis, University of Freiburg, Germany.

Gertisser, R. & Keller, J. (2003). Temporal variations in magma composition at Merapi Volcano (Central Java, Indonesia): magmatic cycles during the past 2000 years of explosive activity. *Journal of Volcanology and Geothermal Research* **123**, 1–23.

Giordano, D., Russell, J. K. & Dingwell, D. B. (2008). Viscosity of magmatic liquids: A model. *Earth and Planetary Science Letters* **271**, 123–134.

Goldoff, B., Webster, J. D. & Harlov, D. E. (2012). Characterization of fluor-chlorapatites by electron probe microanalysis with a focus on time-dependent intensity variation of halogens. *American Mineralogist* **97**, 1103–1115.

Grove, T. L., Elkins-Tanton, L. T., Parman, S. W., Chatterjee, N., Mյntener, O. & Gaetani, G. A. (2003). Fractional crystallization and mantle-melting controls on calc-alkaline differentiation trends. *Contributions to Mineralogy and Petrology* **145**, 515–533.

Hammarstrom, J. M. & Zen, E.-A. (1986). Aluminum in hornblende: an empirical igneous geobarometer. *American Mineralogist* **71**, 1297–1313.

Handley, H. K., Reagan, M., Gertisser, R., Preece, K., Berlo, K., McGee, L. E., Barclay, J. & Herd, R. (2018). Timescales of magma ascent and degassing and the role of crustal assimilation at Merapi volcano (2006–2010), Indonesia. *Geochimica et Cosmochimica Acta* **222**, 34–52.

Harrison, T. M. & Watson, E. B. (1984). The behavior of apatite during crustal anatexis: Equilibrium and kinetic considerations. *Geochimica et Cosmochimica Acta* **48**, 1467–1477.

Hauri, E., Gaetani, G. & Green, T. (2006). Partitioning of water during melting of the Earth's upper mantle at H_2O-undersaturated conditions. *Earth and Planetary Science Letters* **248**, 715–734.

Hercule, S. & Ingrin, J. (1999). Hydrogen in diopside; diffusion, kinetics of extraction–incorporation, and solubility. *American Mineralogist* **84**, 1577–1587.

Holland, T. J. & Blundy, J. (1994). Non-ideal interactions in calcic amphiboles and their bearing on amphibole-plagioclase thermometry. *Contributions to Mineralogy and Petrology* **116**, 433–447.

Hollister, L. S., Grissom, G. C., Peters, E. K., Stowell, H. H. & Sisson, V. B. (1987). Confirmation of the empirical correlation of Al in hornblende with pressure of solidification of calc-alkaline plutons. *American Mineralogist* **72**, 231–239.

Huber, C., Townsend, M., Degruyter, W. & Bachmann, O. (2019). Optimal depth of subvolcanic magma chamber growth controlled by volatiles and crust rheology. *Nature Geoscience* **12**, 762–768.

Humaida, H., Sumarti, S., Subandriyo, N., A., Sukarnen, I. G. M., Suharno, R., K., & Badrijas, I. & S. (2007). Aktivitas Merapi 2006 dan Pemantauan Emisi SO_2 dengan COSPEC, in Erupsi Merapi 2006. Laporan dan Kajian Vulkanisme Erupsi 2006. Departement Energi dan Sumber Daya Mineral, Badan Geologi, Pusat Vulkanologi dan Mitigasi Bencana Geologi.

Humphreys, M. C. S., Edmonds, M., Christopher, T. & Hards, V. (2009). Chlorine variations in the magma of Soufrière Hills Volcano, Montserrat: insights from Cl in hornblende and melt inclusions. *Geochimica et Cosmochimica Acta* **73**, 5693–5708.

Humphreys, M. C. S., Menand, T., Blundy, J. D. & Klimm, K. (2008). Magma ascent rates in explosive eruptions: constraints from H_2O diffusion in melt inclusions. *Earth and Planetary Science Letters* **270**, 25–40.

Johnson, M. C. & Rutherford, M. J. (1989). Experimental calibration of the aluminum-in-hornblende geobarometer with application to Long Valley caldera (California) volcanic rocks. *Geology* **17**, 837–841.

Jones, R. H., McCubbin, F. M., Dreeland, L., Guan, Y. B., Burger, P. V. & Shearer, C. K. (2014). Phosphate minerals in LL chondrites: a record of the action of fluids during metamorphism on ordinary chondrite parent bodies. *Geochimica Cosmochimica Acta* **132**, 120–140.

Kent, A. J. R. (2008). Melt inclusions in basaltic and related volcanic rocks. *Reviews in Mineralogy and Geochemistry* **69**, 273–331.

Ketcham, R. A. (2015). Technical Note: Calculation of stoichiometry from EMP data for apatite and other phases with mixing on monovalent anion sites. *American Mineralogist* **100**, 1620–1623.

Kim, Y. J., Konecke, B., Fiege, A., Simon, A. & Becker, U. (2017). An ab-initio study of the energetics and geometry of sulfide, sulfite, and sulfate incorporation into apatite: The thermodynamic basis for using this system as an oxybarometer. *American Mineralogist* **102**, 1646–1656.

Komorowski, J. C., Jenkins, S., Baxter, P. J., Picquout, A., Lavigne, F., Charbonnier, S., Gertisser, R., Preece, K., Cholik, N., Budi-Santoso, A. & Surono (2013). Paroxysmal dome explosion during the Merapi 2010 eruption: processes and facies relationships of associated high-energy pyroclastic density currents. *Journal of Volcanology and Geothermal Research* **261**, 260–294.

Konecke, B. A., Fiege, A., Simon, A. C., Linsler, S. & Holtz, F. (2019). An experimental calibration of a sulfur-in-apatite oxybarometer for mafic systems. *Geochimica Cosmochimica Acta* **265**, 242–258.

Konecke, B. A., Fiege, A., Simon, A. C., Parat, F. & Stechern, A. (2017). Co-variability of S^{6+}, S^{4+}, and S^{2-} in apatite as a function of oxidation state: Implications for a new oxybarometer. *American Mineralogist* **102**, 548–557.

Koulakov, I., Jakovlev, A. & Luehr, B. G. (2009). Anisotropic structure beneath central Java from local earthquake tomography. *Geochemistry, Geophysics, Geosystems* **10**, n/a–n/a.

Lange, R. A., Frey, H. M. & Hector, J. (2009). A thermodynamic model for the plagioclase-liquid hygrometer/thermometer. *American Mineralogist* **94**, 494–506.

Li, H. & Hermann, J. (2017). Chlorine and fluorine partitioning between apatite and sediment melt at 2.5 GPa, 800°C: a new experimentally derived thermodynamic model. *American Mineralogist* **102**, 580–594.

Li, W. (2019). Eruptive styles of subduction-zone volcanoes: investigation of magmatic volatile budgets and ascent rates using apatite. Ph.D. thesis, Nanyang Technological University, Singapore.

Li, W., Chakraborty, S., Nagashima, K. & Costa, F. (2020). Multicomponent diffusion of F, Cl and OH in apatite with application to magma ascent rates. *Earth and Planetary Science Letters* **550**, 116545.

Li, W. & Costa, F. (2020). A thermodynamic model for F-Cl-OH partitioning between silicate melts and apatite including non-ideal mixing with application to constraining melt volatile budgets. *Geochimica et Cosmochimica Acta* **269**, 203–222.

Lloyd, A. S., Plank, T., Ruprecht, P., Hauri, E. H. & Rose, W. (2013). Volatile loss from melt inclusions in pyroclasts of differing sizes. *Contributions to Mineralogy and Petrology* **165**, 129–153.

Lowenstern, J. B. (1995). Applications of silicate–melt inclusions to the study of magmatic volatiles. In: Thompson, J.F.H. (ed.) *Magmas, Fluids, and Ore Deposits.* Mineral. Assoc. Canada Short Course, vol. **23**, pp. 71–99.

Lowenstern, J. B., Sisson, T. W. & Hurwitz, S. (2017). Probing magma reservoirs to improve volcano forecasts. *EOS-Earth Space Science News* **98**.

Ludwig, K. R. (2003). *User's Manual for Isoplot 3.00: A Geochronological Toolkit for Microsoft Excel (No. 4)*. Berkeley Geochronology Centre, Special Publication.

Luehr, B. G., Koulakov, I., Rabbel, W., Zschau, J., Ratdomopurbo, A., Brotopuspito, K. S., Fauzi, P. & Sahara, D. P. (2013). Fluid ascent and magma storage beneath Gunung Merapi revealed by multi-scale seismic imaging. *Journal of Volcanology and Geothermal Research* **261**, 7–19.

Maclennan, J. (2019). Mafic tiers and transient mushes: evidence from Iceland. *Philosophical Transactions of the Royal Society A: Mathematical, Physical and Engineering Sciences* **377**, 20180021.

McCubbin, F. M., Hauri, E. H., Elardo, S. M., Vander Kaaden, K. E., Wang, J. & Shearer, C. K. (2012). Hydrous melting of the Martian mantle produced both depleted and enriched shergottites. *Geology* **40**, 683–686.

McCubbin, F. M. & Ustunisik, G. (2018). Experimental investigation of F and Cl partitioning between apatite and Fe-rich basaltic melt at 0 GPa and 950–1050°C: Evidence for steric controls on apatite-melt exchange equilibria in OH-poor apatite. *American Mineralogist* **103**, 1455–1467.

McCubbin, F. M., Vander Kaaden, K. E., Tartèse, R., Boyce, J. W., Mikhail, S., Whitson, E. S., Bell, A. S., Anand, M., Franchi, I. A., Wang, J. & Hauri, E. H. (2015). Experimental investigation of F, Cl, and OH partitioning between apatite and Fe-rich basaltic melt at 1.0-1.2 GPa and 950-1000°C. *American Mineralogist* **100**, 1790–1802.

Magee, C., Stevenson, C. T. E., Ebmeier, S. K., Keir, D., Hammond, J. O. S., Gottsmann, J. H., Whaler, K., Schofield, N., Jackson, C. A.-L., Petronis, M. S., O'Driscoll, B., Morgan, J., Cruden, A., Vollgger, S. A., Dering, G., Micklethwaite, S. & Jackson, M. D. (2018). Magma plumbing systems: a geo-physical perspective. *Journal of Petrology* **59**, 1217–1251.

Moretti, R., Métrich, N., Arienzo, I., Di Renzo, V., Aiuppa, A.& Allard, P. (2018) Degassing vs. eruptive styles at Mt. Etna volcano (Sicily, Italy). Part I: volatile stocking, gas fluxing, and the shift from low-energy to highly explosive basaltic eruptions. *Chemical Geology* **482**, 1–17.

Moretti, R., Papale, P. & Ottonello, G. (2003). A model for the saturation of C-O-H-S fluids in silicate melts. *Geological Society, London. Special Publications* **213**, 81–101.

Myers, M. L., Wallace, P. J., Wilson, C. J. N., Morter, B. K. & Swallow, E. J. (2016). Prolonged ascent and episodic venting of discrete magma batches at the onset of the Huckleberry Ridge supereruption. *Earth and Planetary Science Letters* **451**, 285–297.

Müller, A. & Haak, V. (2004). 3-D modeling of the deep electrical conductivity of Merapi volcano (Central Java): integrating magnetotellurics, induction vectors and the effects of steep topography. *Journal of Volcanology and Geothermal Research* **138**, 205–222.

Nadeau, O., Williams-Jones, A. E. & Stix, J. (2013). Magmatic-hydrothermal evolution and devolatilization beneath Merapi volcano. *Journal of Volcanology and Geothermal Research* **261**, 50–68.

Nakada, S. & Motomura, Y. (1999). Petrology of the 1991-1995 eruption at Unzen: Effusion pulsation and groundmass crystallization. *Journal of Volcanology and Geothermal Research* **89**, 173–196.

Newhall, C. G., Bronto, S., Alloway, B., Banks, N. G., Bahar, I., del Marmol, M. A., Hadisantono, R. D., Holcomb, R. T., McGeehin, J., Miksic, J. N., Rubin, M., Sayudi, S. D., Sukhyar, R., Andreastuti, S., Tilling, R. I., Torley, R., Trimble, D. & Wirakusumah, A. D. (2000). 10,000 Years of explosive eruptions of Merapi Volcano, Central Java: archaeological and modern implications. *Journal of Volcanology and Geothermal Research* **100**, 9–50.

O'Leary, J. A., Gaetani, G. A. & Hauri, E. H. (2010). The effect of tetrahedral Al^{3+} on the partitioning of water between clinopyroxene and silicate melt. *Earth and Planetary Science Letters* **297**, 111–120.

Pallister, J. S., Schneider, D. J., Griswold, J. P., Keeler, R. H., Burton, W. C., Noyles, C., Newhall, C. G. & Ratdomopurbo, A. (2013). Merapi 2010 eruption-Chronology and extrusion rates monitored with satellite radar and used in eruption forecasting. *Journal of Volcanology and Geothermal Research* **261**, 144–152.

Pan, Y. & Fleet, M. E. (2002). Compositions of the apatite-group minerals: substitution mechanisms and controlling factors. *Reviews in Mineralogy and Geochemistry* **48**, 13–49.

Papale, P., Moretti, R. & Barbato, D. (2006). The compositional dependence of the saturation surface of $H_2O + CO_2$ fluids in silicate melts. *Chemical Geology* **229**, 78–95.

Parat, F. & Holtz, F. (2004). Sulfur partitioning between apatite and melt and effect of sulfur on apatite solubility at oxidizing conditions. *Contributions to Mineralogy and Petrology* **147**, 201–212.

Parat, F. & Holtz, F. (2005). Sulphur partition coefficient between apatite and rhyolite: the role of bulk S content. *Contributions to Mineralogy and Petrology* **150**, 643–651.

Parat, F., Holtz, F. & Streck, M. J. (2011). Sulfur-bearing magmatic accessory minerals. *Reviews in Mineralogy and Geochemistry* **73**, 285–314.

Peng, G., Luhr, J. F. & McGee, J. J. (1997). Factors controlling sulfur concentrations in volcanic apatite. *American Mineralogist* **82**, 1210–1224.

Peters, S. T. M., Troll, V. R., Weis, F. A., Dallai, L., Chadwick, J. P. & Schulz, B. (2017). Amphibole megacrysts as a probe into the deep plumbing system of Merapi volcano, Central Java, Indonesia. *Contributions to Mineralogy and Petrology* **172**, 1–20.

Philpotts, A. & Ague, J. (2009). *Principles of Igneous and Metamorphic Petrology*, 2nd edn. Cambridge: Cambridge University Press.

Piccoli, P. M. & Candela, P. A. (1994). Apatite in felsic rocks: a model for the estimation of initial halogen concentrations in the bishop tuff (long valley) and tuolumne intrusive suite (Sierra Nevada Batholith) magmas. *American Journal of Science* **294**, 92–135.

Piccoli, P. M. & Candela, P. A. (2002). Apatite in igneous systems. *Reviews in Mineralogy and Geochemistry* **48**, 255–292.

Pichavant, M., Costa, F., Burgisser, A., Scaillet, B., Martel, C. & Poussineau, S. (2007). Equilibration scales in silicic to intermediate magmas - implications for experimental studies. *Journal of Petrology* **48**, 1955–1972.

Pichavant, M., Martel, C., Bourdier, J. L. & Scaillet, B. (2002). Physical conditions, structure, and dynamics of a zoned magma chamber: Mount Peleé (Martinique, Lesser Antilles Arc). *Journal of Geophysical Research* **107**, 2093.

Plank, T, Kelley, K. A, Zimmer M. M., Hauri, E. H. & Wallace, P. J. (2013). Why do mafic arc magmas contain ca. 4 wt % water on average? *Earth and Planetary Science Letters* **364**, 168–179.

Portnyagin, M., Almeev, R., Matveev, S. & Holtz, F. (2008). Experimental evidence for rapid water exchange between melt inclusions in olivine and host magma. *Earth and Planetary Science Letters* **272**, 541–552.

Preece, K. J. (2014). Transitions between effusive and explosive activity at Merapi volcano, Indonesia: a volcanological and petrological study of the 2006 and 2010 eruptions. Ph.D. Thesis, University of East Anglia.

Preece, K., Barclay, J., Gertisser, R. & Herd, R. A. (2013). Textural and micro-petrological variations in the eruptive products of the 2006 dome-forming eruption of Merapi volcano, Indonesia: implications for sub-surface processes. *Journal of Volcanology and Geothermal Research* **261**, 98–120.

Preece, K., Gertisser, R., Barclay, J., Berlo, K., Herd, R. A. & Edinburgh Ion Microprobe Facility (2014). Pre- and syn-eruptive degassing and crystallisation processes of the 2010 and 2006 eruptions of Merapi volcano, Indonesia. *Contributions to Mineralogy and Petrology* **168**, 1–25.

Preece, K., Gertisser, R., Barclay, J., Charbonnier, S. J., Komorowski, J.-C. & Herd, R. A. (2016). Transitions between explosive and effusive phases during the cataclysmic 2010 eruption of Merapi volcano, Java, Indonesia. *Bulletin of Volcanology* **78**, 54.

Putirka, K. D. (2008). Thermometers and barometers for volcanic systems. *Reviews in Mineralogy and Geochemistry* **69**, 61–120.

Putirka, K. D. (2016). Amphibole thermometers and barometers for igneous systems and some implications for eruption mechanisms of felsic magmas at arc volcanoes. *American Mineralogist* **101**, 841–858.

Putirka, K. D., Mikaelian, H., Ryerson, F. & Shaw, H. (2003). New clinopyroxene-liquid thermobarometer for mafic, evolved, and volatile-bearing lava compositions, with applications to lavas from Tibet and the Snake River Plain, Idaho. *American Mineralogist* **88**, 1542–1554.

Qin, Z., Lu, F. & Anderson, A. T. (1992). Diffusive reequilibration of melt and fluid inclusions. *American Mineralogist* **77**, 565–576.

Ratdomopurbo, A., Beauducel, F., Subandriyo, J., Agung Nandaka, I. G. M., Newhall, C. G., Suharna, Sayudi, D. S. & Suparwaka, H. S. (2013). Overview of the 2006 eruption of Mt. *Merapi. J. Journal of Volcanology and Geothermal Research* **261**, 87–97.

Ratdomopurbo, A. & Poupinet, G. (2000). An overview of the seismicity of Merapi volcano (Java, Indonesia), 1983-1994. *Journal of Volcanology and Geothermal Research* **100**, 193–214.

Ridolfi, F. & Renzulli, A. (2012). Calcic amphiboles in calc-alkaline and alkaline magmas: Thermobarometric and chemometric empirical equations valid up to 1130 °C and 2.2 GPa. *Contributions to Mineralogy and Petrology* **163**, 877–895.

Ridolfi, F., Renzulli, A. & Puerini, M. (2010). Stability and chemical equilibrium of amphibole in calc-alkaline magmas: An overview, new thermobarometric formulations and application to subduction-related volcanoes. *Contributions to Mineralogy and Petrology* **160**, 45–66.

Riker, J., Humphreys, M. C. S., Brooker, R. A., De Hoog, J. C. M. & Eim, F (2018). First measurements of OH-C exchange and temperature-dependent partitioning of OH and halogens in the system apatite-silicate melt. *American Mineralogist* **103**, 260–270.

Roggensack, K., Hervig, R. L., McKnight, S. B. & Williams, S. N. (1997). Explosive basaltic volcanism from Cerro Negro volcano: Influence of volatiles on eruptive style. *Science* **277**, 1639–1642.

Rudnick, R. L. & Fountain, D. M. (1995). Nature and composition of the continental crust: a lower crustal perspective. *Reviews of Geophysics* **33**, 267–309.

Rutherford, M. J. & Devine, J. D. (2003). Magmatic conditions and magma ascent as indicated by hornblende phase equilibria and reactions in the 1995–2002 Soufriére Hills magma. *Journal of Petrology* **44**, 1433–1454.

Saepuloh, A., Koike, K., Omura, M., Iguchi, M. & Setiawan, A. (2010). SAR- and gravity change-based characterization of the distribution pattern of pyroclastic flow deposits at Mt. Merapi during the past 10 years. *Bulletin of Volcanology* **72**, 221–232.

Saepuloh, A., Urai, M., Aisyah, N., Sunarta, Widiwijayanti, C., Subandriyo, J. & Jousset, P. (2013). Interpretation of ground surface changes prior to the 2010 large eruption of Merapi volcano using ALOS/PALSAR, ASTER TIR and gas emission data. *Journal of Volcanology and Geothermal Research* **261**, 130–143.

Sato, H., Holtz, F., Behrens, H., Botcharnikov, R. & Nakada, S. (2004). Experimental petrology of the 1991-1995 Unzen dacite, Japan. Part II: Cl/OH partitioning between hornblende and melt and its implications for the origin of oscillatory zoning of hornblende phenocrysts. *Journal of Petrology* **46**, 339–354.

Scaillet, B. & Evans, B. W. (1999). The 15 June 1991 eruption of Mount Pinatubo. I. Phase equilibria and pre-eruption P-T-fO_2-fH_2O conditions of the dacite magma. *Journal of Petrology* **40**, 381–411.

Scaillet, B. & Pichavant, M. (2005). A model of sulphur solubility for hydrous mafic melts: Application to the determination of magmatic fluid compositions of Italian volcanoes. *Annals of Geophysics* **48**, 671–698.

Schettler, G., Gottschalk, M. & Harlov, D. E. (2011). A new semi-micro wet chemical method for apatite analysis and its application to the crystal chemistry of fluorapatite-chlorapatite solid solutions. *American Mineralogist* **96**, 138–152.

Schmidt, M. W. (1992). Amphibole composition in tonalite as a function of pressure: an experimental calibration of the Al-in-hornblende barometer. *Contributions to Mineralogy and Petrology* **110**, 304–310.

Scott, J. A. J., Humphreys, M. C. S., Mather, T. A., Pyle, D. M. & Stock, M. J. (2015). Insights into the behaviour of S, F, and Cl at Santiaguito Volcano, Guatemala, from apatite and glass. *Lithos* **232**, 375–394.

Segall, P. (2010). *Earthquake and Volcano Deformation*. Princeton, NJ: Princeton University Press.

Segall, P. (2019). Magma chambers: what we can, and cannot, learn from volcano geodesy. *Philosophical Transactions of the Royal Society A: Mathematical, Physical and Engineering Sciences* **377**, 20180158.

Sisson, T. W. & Grove, T. L. (1993). Experimental investigations of the role of H_2O in calc-alkaline differentiation and subduction zone magmatism. *Contributions to Mineralogy and Petrology* **113**, 143–166.

Sparks, R. S. J. (2003). Forecasting volcanic eruptions. *Earth and Planetary Science Letters* **210**, 1–15.

Stock, M. J., Humphreys, M. C. S., Smith, V. C., Isaia, R. & Pyle, D. M. (2016). Late-stage volatile saturation as a potential trigger for explosive volcanic eruptions. *Nature Geoscience* **9**, 249–254.

Stock, M. J., Humphreys, M. C. S., Smith, V. C., Isaia, R., Brooker, R. A. & Pyle, D. M. (2018). Tracking volatile behaviour in sub-volcanic plumbing systems using apatite and glass: insights into pre-eruptive processes at Campi Flegrei. *Journal of Petrology* **59**, 2463–2492.

Stock, M. J., Humphreys, M. C. S., Smith, V. C., Johnson, R. D. & Pyle, D. M. (2015). New constraints on electron-beam induced halogen migration in apatite. *American Mineralogist* **100**, 281–293.

Stormer, J., Pierson, M. L. & Tacker, R. C. (1993). Variation of F and Cl X-ray intensity due to anisotropic diffusion in apatite. *American Mineralogist* **78**, 641–648.

Sparks, R. S. J. & Cashman, K. V. (2017). Dynamic magma systems: implications for forecasting volcanic activity. *Elements* **13**, 35–40.

Steele-MacInnis, M. (2019). Seeking the most hydrous, primitive arc melts: the glass is half full. *American Mineralogist* **104**, 1217–1218.

Surono, Jousset, P., Pallister, J., Boichu, M., Buongiorno, M. F., Budisantoso, A., Costa, F., Andreastuti, S., Prata, F., Schneider, D., Clarisse, L., Humaida, H., Sumarti, S., Bignami, C., Griswold, J., Carn, S., Oppenheimer, C. & Lavigne, F. (2012). The 2010 explosive eruption of Java's Merapi volcano—A '100-year' event. *Journal of Volcanology and Geothermal Research* **241–242**, 121–135.

Tiede, C., Camacho, A. G., Gerstenecker, C., Fernández, T. J. & Suyanto, I. (2005). Modeling the density at Merapi volcano area, Indonesia, via the inverse gravimetric problem. *Geochemistry Geophysics Geosystems* **6**, Q09011.

Troll, V. R., Chadwick, J. P., Jolis, E. M., Deegan, F. M., Hilton, D. R., Schwarzkopf, L. M., Blythe, L. S. & Zimmer, M. (2013). Crustal volatile release at Merapi volcano; the 2006 earthquake and eruption events. *Geology Today* **29**, 96–101.

Troll, V. R., Hilton, D. R., Jolis, E. M., Chadwick, J. P., Blythe, L. S., Deegan, F. M., Schwarzkopf, L. M. & Zimmer, M. (2012). Crustal CO_2 liberation during the 2006 eruption and earthquake events at Merapi volcano. *Geophysical Research Letters* **39**, L11302.

Van Hoose, A. E., Streck, M. J., Pallister, J. S. & Wälle, M. (2013). Sulfur evolution of the 1991 Pinatubo magmas based on apatite. *Journal of Volcanology and Geothermal Research* **257**, 72–89.

Voight, B., Young, K. D., Hidayat, D., Purbawinata, M. A., Ratdomopurbo, A., Sayudi, D. S., Lahusen, R., Marso, J., Murray, T. L., Dejean, M., Iguchi, M. & Ishihara, K. (2000). Deformation and seismic precursors to dome-collapse and fountain-collapse nuées ardentes at Merapi Volcano, Java, Indonesia, 1994–1998. *Journal of Volcanology and Geothermal Research* **100**, 261–287.

Wade, J. A., Plank, T., Zimmer, M. M., Hauri, E., Roggensack, K. & Kelley, K. (2008). Prediction of magmatic water contents via measurement of H_2O in clinopyroxene phenocrysts. *Geology* **36**, 799–802.

Wagner, D., Koulakov, I., Rabbel, W., Luehr, B.-G., Wittwer, A., Kopp, H., Bohm, M., Asch, G., the MERAMEX Scientists (2007). Joint inversion of active and passive seismic data in Central Java. *Geophysical Journal International* **170**, 923–932.

Wallace, P. J. (2005). Volatiles in subduction zone magmas: concentrations and fluxes based on melt inclusion and volcanic gas data. *Journal of Volcanology and Geothermal Research* **140**, 217–240.

Wallace, P. J., Plank, T., Edmonds, M. & Hauri, E. H. (2015). Volatiles in magmas. In: Sigurdsson, H., Houghton, B., McNutt, S., Rymer, H., Stix, J. (eds) *The Encyclopedia of Volcanoes*, **2**nd edn. Academic Press, Elsevier, pp. 163–183.

Waters, L. E. & Lange, R. A.(2015). An updated calibration of the plagioclase–liquid hygrometer–thermometer applicable to basalts through rhyolites. *American Mineralogist* **100**, 2172–2184.

Watson, E. B. & Green, T. H. (1981). Apatite/liquid partition coefficients for the rare earth elements and strontium. *Earth and Planetary Science Letters* **56**, 405–421.

Webster, J. D. & Piccoli, P. M. (2015). Magmatic apatite: a powerful, yet deceptive, mineral. *Elements* **11**, 177–182.

Webster, J. D., Sintoni, M. F. & De Vivo, B. (2009). The partitioning behavior of Cl, S, and H2O in aqueous vapor ± saline-liquid saturated phonolitic and trachytic melts at 200 MPa. *Chemical Geology* **263**, 19–36.

Wegler, U. & Lühr, B.-G. (2001). Scattering behaviour at Merapi volcano (Java) revealed from an active seismic experiment. *Geophysical Journal International* **145**, 579–592.

Webster, J. D., Vetere, F., Botcharnikov, R. E., Goldoff, B., McBirney, A., & Doherty, A. L. (2015) Experimental and modeled chlorine solubilities in aluminosilicate melts at 1 to 7000 bars and 700 to 1250°C: Applications to magmas of Augustine Volcano, Alaska. *American Mineralogist* **100**, 522–535.

Whitley, S., Gertisser, R., Halama, R., Preece, K., Troll, V. R. & Deegan, F. M. (2019). Crustal CO_2 contribution to subduction zone degassing recorded through calc-silicate xenoliths in arc lavas. *Scientific Reports* **9**, 8803.

Widiyantoro, S., Ramdhan, M., Métaxian, J.-P., Cummins, P. R., Martel, C., Erdmann, S., Nugraha, A. D., Budi-Santoso, A., Laurin, A. & Fahmi, A. A. (2018). Seismic imaging and petrology explain highly explosive eruptions of Merapi Volcano, Indonesia. *Scientific Reports* **8**, 13656.